UC San Diego
UC San Diego Electronic Theses and Dissertations

Title

Fabrication and applications of nanocomposite structures using anodized aluminum oxide membranes

Permalink

https://escholarship.org/uc/item/715380zp

Author

Gapin, Andrew Isaac

Publication Date

2007

Peer reviewed|Thesis/dissertation

eScholarship.org Powered by the California Digital Library
University of California

UNIVERSITY OF CALIFORNIA, SAN DIEGO

Fabrication and Applications of Nanocomposite Structures Using Anodized Aluminum Oxide Membranes

A dissertation submitted in partial satisfaction of the

requirements for the degree Doctor of Philosophy

in

Materials Science and Engineering

by

Andrew Isaac Gapin

Committee in Charge:

Professor Sungho Jin, Chair
Professor Prabhakar Bandaru
Professor Yu-Hwa Lo
Professor Vlado Lubarda
Professor Sunil Sinha

2007

Copyright

Andrew Isaac Gapin, 2007

All rights reserved

The dissertation of Andrew Isaac Gapin is approved, and it is acceptable in quality and form for publication on microfilm:

____

____

____

____

____

Chair

University of California, San Diego

2007

Dedicated to

everyone that made this possible

The breeze is blowin’ me a new perfume
It’s givin’ my heart a little elbow room
And the sea is singin’ lullabies
And everything’s slowin’ down flowin’ counterclockwise
Everything’s slowin’ down flowin’ counterclockwise

Roger Clyne

TABLE OF CONTENTS

Signature page....................iii
Dedication....................iv
Epigraph....................v
Table of Contents....................vi
List of Figures....................xiii
List of Tables....................xiv
Acknowledgements....................xv
Vita....................xvi
Abstract....................xviii

CHAPTER 1: INTRODUCTION 1

CHAPTER 2: BACKGROUND 4

2.1 History of aluminum and aluminum production 4
2.2 Properties of aluminum and aluminum oxide.................... 7
2.3 Synthesis of anodized aluminum oxide 10
2.3.1 Anodization of aluminum 10
2.3.2 Anodized aluminum oxide on bulk aluminum 14
2.3.2.1 History of AAO on bulk aluminum 14
2.3.2.2 Nucleation and growth of the porous layer 17
2.3.2.3 Self-ordering in the porous layer 23
2.3.3 Imprinting and guided anodization 34
2.3.4 Anodizided aluminum oxide on thin film aluminum 41
2.4 Electrodeposition of nanowires 41
2.4.1 Preparing the pores for electrodeposition 42
2.4.2 Elemental and alloy nanowires 46
2.4.3 Multi-layer nanowires 52
2.5 Applications of anodized aluminum oxide membranes 54
2.5.1 Structural and architectural applications 54
2.5.2 Sensors and other nanotechnology applications 55

2.5.3 Magnetic recording media 55
CHAPTER 3: EXPERIMENTAL PROCEDURES 66
3.1 Thin film deposition 66
3.2 Sample preparation 67
3.3 Anodization 69
3.4 Electrodeposition 71
3.5 Annealing 72
3.6 Sample characterization and analysis 74
CHAPTER 4: RESULTS AND DISCUSSION 77
4.1 Thin film deposition 77
4.1.1 Metal underlayers 77
4.1.2 Aluminum film deposition and surface roughness 79
4.2 Anodization of aluminum films 87
4.3 Nanowire deposition into the AAO pores 92
4.3.1 CoPt nanowires 92
4.3.1.1 Fabrication of CoPt nanowires 92
4.3.1.2 Microstructure and composition of CoPt nanowires 100
4.3.1.3 Magnetic data for CoPt nanowires 102
4.3.2 Ni/CoPt composite nanowires 107
4.3.2.1 Fabrication of Ni/CoPt nanowires 107
4.3.2.2 Microstructure and composition of Ni/CoPt nanowires 110
4.3.2.3 Magnetic data for Ni/CoPt nanowires 111
4.4 Nanoimprint lithography using an AAO based master 118
CHAPTER 5: SUMMARY, CONCLUSIONS, AND FUTURE WORK 123
REFERENCES 128

LIST OF FIGURES

Figure 2.1: Graph showing the increase in commercial aluminum production from 1900-2000. ... 7

Figure 2.2: Directional movement of ions in the anodization process of aluminum... 11

Figure 2.3: Schematic diagram showing the two main types of anodic coatings... 12

Figure 2.4: Cross sectional image of a nonporous barrier oxide formed in a tartrate solution on aluminum ... 13

Figure 2.5: Idealized structure of a porous anodic film... 13

Figure 2.6: Early proposed pore structure of AAO produced in a 120 V phosphoric acid solution, including relevant dimensions... 15

Figure 2.7: Electron microscope image of the cross-section of a porous alumina film anodized in 4 wt. % phosphoric acid at 120 V... 16

Figure 2.8: Schematic diagram showing the shape of the barrier layer and pore structure and the equations that model their shape... 17

Figure 2.9: (A) Anodization of aluminum at constant voltage, (B) anodization of aluminum at constant current density... 18

Figure 2.10: Influence of the surface morphology on field-enhanced dissolution, showing the dependence of field-enhancement on the angle Θ ... 19

Figure 2.11: Graphs showing the influence of the electrolyte solution and anodization voltage on the current density. (A) 0.2 M oxalic acid and (B) 0.5 M sulfuric acid at different voltages: 1 = 5 V, 2 = 10 V, 3 = 15 V, 4 = 20 V, 5 = 30 V, 6 = 40 V ... 20

Figure 2.12: The variation in the interpore distance (A) and cell size (B) are shown as a consequence of the electrolyte and anodization voltage. Shown in (A): phosphoric acid, ▲, sulfuric acid, ●, oxalic acid, □. In (B): oxalic acid, △, phosphoric acid, □, glycolic acid, ○, tartaric acid, ❍ ... 21

Figure 2.13: Optimal pore sizes for the typically used anodizing solutions of oxalic, sulfuric, and phosphoric acids in relation to the applied voltage ... 22

Figure 2.14: Influence of temperature on the pore density for galvanostatic anodization (A) and potentiostatic anodization (B), at anodization temperatures of 10°C, □, 20°C, ○, 30°C, ▽, 40°C, △ ... 23

Figure 2.15: Variation of the regularity of the porous structure as the anodized time and porous layer thickness increases; samples anodized in 0.5 M H_2SO_4 at 25 V for (A) 9 min [2.4 µm], (B) 36 min [10.6 µm], and (C) 750 min [202 µm]; (D) shows a lower magnification image of (C) 24

Figure 2.16: Scanning electron microscope images of AAO formed in 0.3 M H_2SO_4 at (A) 20 V for 1500 min, (B) 23 V for 1000 min, (C) 25 V for 706 min, and (D) 27 V for 450 min 25

Figure 2.17: A summary of the self-ordering conditions for different electrolyte solutions and the resulting cell sizes 26

Figure 2.18: Experimental setup depicting (A) a single pore nucleating and (B) two pores attempting to nucleate in a thin strip of aluminum insulated on either side. 27

Figure 2.19: Diagram showing the volume expansion of aluminum to aluminum oxide during anodization and the formation of a pore 28

Figure 2.20: Low magnification SEM image showing the presence of ordered domains in the AAO 30

Figure 2.21: Graph showing the increasing size of the ordered domain size with increasing anodization time for a sample anodized in 0.3 M oxalic acid at 40 V. 31

Figure 2.22: Procedure for the process of a two-step anodization of aluminum: (A) initial anodization for a long time, (B) removal of the first anodization layer, (C) growth of the second anodization layer 33

Figure 2.23: Imprinting of aluminum with a schematic diagram showing the imprinting process (A), and SEM images showing the difference between the imprinted and non-imprinted areas (B).. 35

Figure 2.24: SEM image showing the mismatch of imprinting conditions with the anodization conditions 36

Figure 2.25: Imprinting with a single missing site and the resulting pore array formed after anodization with the arrows indicating the missing sites (A), and after an etching treatment to widen the pores (B). Imprinting with two chained missing sites on the SiC mold (C) and in the anodized pattern, identified by the circles (D) 37

Figure 2.26: SEM image of the barrier layer of an anodized aluminum thin film on a silicon substrate 39

Figure 2.27: Schematic diagram of the electrodeposition process. The bath solution consists of aqueous metal salts as represented by the M^+ and A^-. The object to be plated is the cathode 42

Figure 2.28: SEM images showing the interface between the Si substrate, Ti buffer layer, and the Au nanowires, (A) after anodization showing the pores and (B) after electrodeposition and removal of the AAO layer to show the nanowires...... 45

Figure 2.29: SEM cross-sectional image of silver nanowires, appearing as the bright vertical stripes, grown inside the pores of an AAO film 46

Figure 2.30: M-H loops showing the variation in the coercivity as measured parallel to the nanowire axis (☐) and perpendicular to the nanowire axis (●) for nanowires with diameters of (A) 55 nm, (B) 40 nm, and (C) 30 nm..................... 48

Figure 2.31: The phase diagram of the CoPt system showing the composition range of the ordered face centered tetragonal $L1_0$ phase (A) and the crystal structure of the $L1_0$ phase (B) 49

Figure 2.32: M-H loops for CoPt nanowires measured with the applied magnetic field parallel to the wire axis (—) and perpendicular to the wire axis (- - -) for the 80 nm $Co_{50}Pt_{50}$ nanowires (A) and the 35 nm $Co_{47}Pt_{53}$ nanowires (B) 51

Figure 2.33: A schematic diagram showing the structure of the Ni/Cu multi-layer nanowires (A) and a TEM image of segments of the dispersed nanowires (B) 53

Figure 2.34: (A) The increase in areal storage density is shown along with the compound growth rate (CGR), the introduction of the first magnetoresistance (MR) recording head, the first giant magnetoresistance (GMR) head, and antiferromagnetically coupled (AFC) media. (B) The decrease in average price per gigabyte of storage is shown since 1990 for different types of storage, including projections through 2010 57

Figure 2.35: Schematic diagram showing the longitudinal magnetic recording system with separate read and write heads, the relevant parameters, and the grain structure with magnetic transitions. Typical values for the parameters are: track width W = 210 nm, thickness of film t = 14 nm, bit length B = 30 nm, distance of heads to surface d = 10 nm..................... 59

Figure 2.36: Schematic diagram showing the differences between longitudinal (left) and perpendicular (right) recording technologies..................... 61

Figure 2.37: Transmission electron microscope images of the top view of the magnetic CoCrPt-SiO_2 layer showing the grain segregation (A) and the cross section showing the columnar grain structure and sequence of underlayers (B) ... 62

Figure 2.38: Schematic diagram illustrating a patterned recording media and showing the influence that bit diameter and bit spacing have on the corresponding recording density ... 64

Figure 3.1: Photograph illustrating a prepared sample with an electrical connection and insulated with lacquer ... 68

Figure 3.2: Schematic diagram showing the anodization setup used in these experiments ... 69

Figure 3.3: A graph showing the heating and cooling cycle for the annealing process, indicated in a temperature versus time plot ... 74

Figure 4.1: Scanning electron microscope images of the as-deposited Al films deposited at 330°C 150 W (A), 200°C 150 W (B), 25°C 150 W (C), 25°C 125 W (D), 25°C 100 W (E), and 25°C 75 W (F) ... 82

Figure 4.2: AFM image of the surface of the optimum sputtering condition of 25°C and 100 W, showing the RMS surface roughness ... 84

Figure 4.3: SEM images showing the influence of alloying elements on the Al films for 200 nm thick films. (A) as-deposited Al film, (B) $Al_{97}Ti_3$ film, (C) $Al_{97}Zr_3$ film, (D) anodized Al film, (E) anodized $Al_{97}Ta_3$ film, (F) anodized $Al_{94}Ta_6$ film ... 85

Figure 4.4: SEM images showing the surface of the Al film after chemical mechanical polishing (A) and the top surface of the same film after anodization at 25 V in 0.3 M oxalic acid at 5ºC (B) ... 87

Figure 4.5: SEM images showing the top surface of an Al film anodized in 0.3 M oxalic acid at 5°C and an applied voltage of 25 V (A), and a higher magnification image of the top surface (B) ... 88

Figure 4.6: Plot showing the increase in current over the course of the anodization process carried out at 25 V in 0.3 M oxalic acid at 5°C ... 89

Figure 4.7: Schematic diagrams showing the procedure for a two-step anodization. (A) partial anodization of the Al layer, (B) removal of the anodized layer leaving the depressions from the pore bases as nucleation sites for the next anodization step, (C) second anodization to create through pores to the metal underlayer, and (D) electrodeposition to create nanowires ... 90

Figure 4.8: SEM images of a sample after a two-step anodization process. The top surface is shown, displaying improved pore regularity at low magnification (A), at successively higher magnification (B) and (C), a cross-sectional image showing the pore structure (D), and a higher magnification cross-sectional image (E) ... 91

Figure 4.9: A graph showing the variation in Co and Pt composition determined by EDS analysis in atomic percent as the electrodeposition current density is increased 94

Figure 4.10: SEM image showing the AAO template and embedded CoPt nanowires, the edge was exposed by fracturing the sample, showing the height of the nanowires and the template 96

Figure 4.11: SEM images showing CoPt nanowires of different lengths that have been fabricated, ~30 nm (A), ~100 nm (B), ~500 nm (C), and a low magnification image showing the coverage of CoPt nanowires on the substrate (D) 98

Figure 4.12: An SEM image of CoPt nanowires exposed by ion milling from a focused ion beam to remove the surrounding AAO template 99

Figure 4.13: An EDS scan showing the number of counts obtained for each element that was detected for a sample of CoPt nanowires subjected to a post-deposition annealing treatment at 700°C 101

Figure 4.14: M-H loops showing the magnetic properties of the annealed and as-deposited CoPt nanowires, measured in the in-plane direction parallel to the substrate (A), and in the perpendicular direction along the nanowire axis (B) ... 103

Figure 4.15: A schematic diagram showing the structure of the fabricated Ni/CoPt composite nanowires in the AAO template 108

Figure 4.16: SEM images showing the composite Ni/CoPt nanowires from a 45° angle after removal of the AAO template via chemical etching to expose the nanowires, at lower magnification (A) and higher magnification (B) 109

Figure 4.17: M-H hysteresis loops measured in the perpendicular direction along the nanowire axis for the annealed CoPt, Ni_{20nm} / $CoPt_{80nm}$, Ni_{50nm} / $CoPt_{50nm}$, Ni_{80nm} / $CoPt_{20nm}$, and Ni nanowires, all with equivalent lengths of 100 nm 111

Figure 4.18: M-H loops showing the magnetic properties of the annealed composite Ni/CoPt nanowires measured in the in-plane and perpendicular directions for the Ni_{20nm} / $CoPt_{80nm}$ (A), Ni_{50nm} / $CoPt_{50nm}$ (B), and Ni_{80nm} / $CoPt_{20nm}$ (C) samples 113

Figure 4.19: Schematic diagram showing the process steps in the replication of an imprinting master stamp: (A) an ideally ordered pore structure prepared from anodizing an Al film imprinted by the master stamp, (B) electrodeposition of nanowires into the pores and onto the surface of the AAO template, (C) chemical dissolution of the Si substrate and AAO template leaving only the nanowires, (D) imprinting of an Al film using the prepared nanowire array,

and (E) an imprinted film with ordered surface depressions, ready to repeat the process 119

Figure 4.20: SEM images of the freestanding Ni nanowire arrays produced using the procedure described in the text, (A) top view of the nanowire bases that were attached to the Si substrate, (B) cross-sectional lower magnification image of a sectioned Ni film and nanowire array with the film crumpled during sectioning, and (C) higher magnification cross-sectional image, again crumpled during sectioning 121

LIST OF TABLES

Table 2.1: A chart showing the composition variation of the compounds in several bauxite samples 5

Table 2.2: A summary of the physical properties of pure aluminum 8

Table 2.3: Physical properties of the polycrystalline α-Al_2O_3 phase 9

Table 2.4: Structural measurements of self-ordered porous alumina prepared in different electrolytes 29

Table 2.5: Relationship between the thickness of the aluminum layer and the regularity of the pore arrays 40

Table 4.1: The corresponding RMS surface roughness values as measured by an AFM for the different sputtering parameters when the substrate temperature and sputtering power were varied 80

Table 4.2: Data table summarizing the coercivities measured in the perpendicular and in-plane directions for different nanowire compositions 114

ACKNOWLEDGEMENTS

I would like to thank my advisor, Professor Sungho Jin, for his guidance and support during my time in graduate school and throughout the course of this project. I also want to thank Dr. Leon Chen for all of the help, assistance, and instruction he has given me during the duration of my tenure here at the University of California, San Diego.

I am grateful for the time that all of my committee members, Professors Prabhakar Bandaru, Yu-Hwa Lo, Vlado Lubarda, and Sunil Sinha, have set aside out of their busy schedules, as well as the useful input they have provided. In addition to the faculty assistance that I have received, invaluable contributions were also received from many of my fellow group members. I would specifically like to thank the following people for their assistance on various aspects of this work: Dr. Chris Hong, Edward Choi, Dr. Daniel Ye, Dr. Joseph AuBuchon, Dr. Chiara Daraio, Jeongwon Park, Eric Kim, Kevin Noh, Mariana Loya, Edin Chen, and Dr. Brian Oh.

I graciously acknowledge the financial support from the Center for Magnetic Recording Research (CMRR) at the University of California, San Diego. Financial support was also provided by the National Science Foundation (NSF-NIRT grant numbers DMR-0210559 and DMI-0303790) and from Veeco Instruments and the University of California Discovery Fund (grant number ele05-10241). Without such financial support this work would not have been possible. Finally, I would like to thank my family and friends for their support and encouragement throughout this long journey.

VITA

1980	Born New York, USA
2002	B.S., Materials Science and Engineering, Georgia Institute of Technology
2003	M.S., Materials Science and Engineering, University of California, San Diego
2007	Ph.D., Materials Science and Engineering, University of California, San Diego

JOURNAL PUBLICATIONS

1. Joseph F. AuBuchon, Li-Han Chen, Andrew I. Gapin, Dong-Wook Kim, Chiara Daraio, Sungho Jin, "Multiple Sharp Bendings of Carbon Nanotubes during Growth to Produce Zigzag Morphology", *Nano Letters*, **4**, 1781 (2004).

2. L. –H. Chen, J. F. AuBuchon, A. Gapin, C. Daraio, P. Bandaru, S. Jin, D. –W. Kim, I. K. Yoo, "Control of carbon nanotube morphology by change of applied bias field during growth", *Applied Physics Letters*, **85**, 5373 (2004).

3. Joseph F. AuBuchon, Li-Han Chen, Andrew I. Gapin, Sungho Jin, "Opening of Aligned Carbon Nanotube Ends via Room-Temperature Sputter Etching Process", *Journal of Applied Physics*, **97**, 124310 (2005).

4. Joseph F. AuBuchon, Chiara Daraio, Li-Han Chen, Andrew I. Gapin, Sungho Jin, "Iron Silicide Root Formation in Carbon Nanotubes Grown by Microwave PECVD", *Journal of Physical Chemistry B*, **109**, 24215 (2005).

5. L. –H. Chen, J. F. AuBuchon, I. –C. Chen, C. Daraio, X. –R. Ye, A. I. Gapin, S. Jin, C. M. Wang, "Growth of Aligned Carbon Nanotubes on Carbon Microfibers by DC Plasma-Enhanced Chemical Vapor Deposition", *Applied Physics Letters*, **88**, 033103 (2006).

6. A. I. Gapin, X. R. Ye, J. F. AuBuchon, L. H. Chen, Y. J. Tang, S. Jin, "CoPt patterned media in anodized aluminum oxide templates", *Journal of Applied Physics* **99**, 08G902 (2006).

7. Joseph F. AuBuchon, Li-Han Chen, Andrew I. Gapin, Sungho Jin, “Electric Field Guided Growth of Carbon Nanotubes during DC PECVD”, *Chemical Vapor Deposition* **12**, 1 (2006).

8. X. R. Ye, L. H Chen, C. Wang, J. F. Aubuchon, I. C. Chen, A. I. Gapin, J. B. Talbot, S. Jin, “Electrochemical Modification of Vertically Aligned Carbon Nanotube Arrays”, *Journal of Physical Chemistry B*, **110**, 12938 (2006).

9. C. Choi, D. H. Hong, A. I. Gapin, S. Jin, “Control of M-H Loop Shape in Perpendicular Recording Media by Ion Implantation”, *IEEE Transactions on Magnetics*, **43**, 2121 (2007).

10. A. I. Gapin, X. R. Ye, L. H. Chen, D. H. Hong, S. Jin, “CoPt Hard Magnet/Ni Soft Magnet Composite Nanowire Array for Patterned Recording Media”, *IEEE Transactions on Magnetics*, **43**, 2151 (2007).

ABSTRACT OF THE DISSERTATION

Fabrication and Applications of Nanocomposite Structures Using

Anodized Aluminum Oxide Membranes

by

Andrew Isaac Gapin

Doctor of Philosophy in Materials Science and Engineering

University of California, San Diego, 2007

Professor Sungho Jin, Chair

As the field of nanotechnology continues to advance and device feature sizes scale down to ever smaller dimensions, it is becoming increasingly important to develop quick and efficient methods for large-scale production at the nanoscale. Creating such a template would have widespread uses in areas such as magnetic data storage, chemical sensors, and mask technology. One promising approach to realizing this goal may lie in utilizing the self-ordering behavior found in porous anodized aluminum oxide (AAO). This material offers many advantages such as the ability to customize the pore diameter and spacing and easy device integration based on its compatibility with silicon

substrates. The pores of the AAO templates can be filled with many different materials via electrochemical deposition or other methods to produce numerous potential devices.

In this work, current research results detailing the fabrication of AAO templates and their use in creating ~100 nm tall CoPt, Ni, and composite Ni/CoPt nanowires is demonstrated. The synthesis of such nanostructures may ultimately be advantageous for new types of patterned magnetic recording media. The Ni nanowires exhibit relatively soft magnetic coercivity of 242 Oe, while the CoPt nanowires show a very high coercivity of at least 10.97 kOe, measured in the perpendicular direction along the nanowires axis. The composite soft magnet / hard magnet Ni/CoPt nanowires exhibit intermediate perpendicular coercivities depending on the relative amounts of Ni and CoPt. The Ni_{80nm} / $CoPt_{20nm}$ nanowires showed a coercivity of 1.96 kOe, the Ni_{50nm} / $CoPt_{50nm}$ nanowires had a coercivity of 3.59 kOe, and the Ni_{20nm} / $CoPt_{80nm}$ nanowires had a coercivity of 5.10 kOe. This marked decrease in the coercivity is significant because it could facilitate easier magnetic data writing. Analysis of the magnetic properties of the various nanowire structures and their dependence on the processing parameters is presented. A method for utilizing the AAO structure to replicate a master stamp for nanoimprinting technology is also discussed. In addition, plans for future work and a discussion of the application of these fabricated structures towards magnetic recording technology are presented.

CHAPTER 1: INTRODUCTION

As the magnetic storage devices currently in use in today's computers and other devices continue to increase in storage capacity and density, the current technology will soon prove to be a limiting factor. One possible alternative is the use of a patterned media type of storage where one bit of data is stored within a single nanowire or other vertically oriented magnetic structure. In order to reach high storage densities, the size of these features must be extremely small, ideally around 10 nm or less, with a similarly small spacing in order to produce a device having a clear advantage over the currently available alternatives. While industrial and consumer demands push for these further advances, the cost and feasibility of producing such nanometer-sized features on a large scale is a daunting challenge. Because of their advantageous properties, anodized aluminum oxide (AAO) membranes have received considerable attention from researchers focusing on these problems. With their self-organizational characteristics and the ability to tailor the size, spacing, and depth of the pores, these AAO membranes have many potential applications, even outside of the field of magnetic data storage.

Much of the preliminary research work on AAO membranes for magnetic storage applications has shown significant promise. Several other research groups have demonstrated magnetic properties of nanowires within an AAO matrix. However, the ability to fabricate small diameter and high magnetic coercivity CoPt nanowires has previously been uncovered in the literature. In addition, the production of nanocomposites within the AAO matrix has also received little attention. This capability could be significant for tailoring the properties of the nanowires for specific

applications. For the case of these magnetic nanowires the addition of a second layer can act to effectively reduce the magnetic coercivity in high coercivity alloys to a value that would make it easier to write and erase data.

In this research work it is shown how the anodization of aluminum thin films on silicon substrates and subsequent electrodeposition of magnetic nanowires into the pores can have potential applications in magnetic recording technology. The ability to deposit high anisotropy magnetic materials with a customizable structure into a large array of nanometer scale pores will prove to be an integral process in future magnetic data storage devices. Based on this same anodization and electrodeposition process, I also show how a nanoimprinting master stamp can be replicated using the anodization characteristics of AAO and an electrodeposition step.

To give a brief outline of this dissertation, Chapter 2 provides background information on the history of anodized aluminum oxide as well as more detailed information on the anodization process, some of the related work on electrodeposition of nanowires into the AAO templates, and some potential applications of AAO based devices. Chapter 3 focuses on the experimental details of the sample preparation processes used for these experiments such as the anodization, electrodeposition, annealing, and sample characterization techniques. Chapter 4 contains the results and discussion section, divided into four sub-sections. Section 4.1 details the thin film deposition techniques used in preparing the starting materials. Section 4.2 covers the anodization of the aluminum films. Section 4.3 discusses the microstructure, magnetic properties, and advantages of the CoPt and Ni/CoPt composite nanowires that have been fabricated as part of this research. Section 4.4 shows how a nanoimprinting master

stamp can be replicated based on the anodization and electrodeposition techniques used in this research. Chapter 5 concludes this dissertation with a summary of the main results of the work and covers some of the ongoing research and future research plans.

CHAPTER 2: BACKGROUND

2.1 History of aluminum and aluminum production:

Aluminum was discovered and named in 1807 by Sir Humphry Davy, while in a strange occurrence, what turned out to be aluminum oxide was first discovered more than 40 years earlier in 1761 by L. B. G. de Moreveau.[1] As a material, aluminum has many useful properties, among them are good electrical and thermal conductivity, it is lightweight yet some alloys are very strong, it has good corrosion resistance, it is easily cast and formed and it readily accepts many types of surface finishes. Another important point is that aluminum is the most abundant metallic element in the Earth's crust and in terms of all elements it ranks third behind only silicon and oxygen.[2] This ready availability makes aluminum an economical choice for many applications. However, in order to exploit this abundance many years of research were needed before a commercially viable extraction process was developed.

Problems arose because naturally occurring aluminum is found only in combination with other materials, most commonly as bauxite. Bauxite is an aluminum ore that accounts for 99% of metallic aluminum and has varying compositions but typically contains combinations of the following: gibbsite ($Al(OH)_3$), boehemite and diaspore ($AlOOH$), iron oxides goethite ($FeOOH$) and hematite (Fe_2O_3), clay minerals such as kaolinite ($Al_2Si_2O_5(OH)_4$), and anatase (TiO_2).[3] Depending on the type of ore deposit, these compounds may be present in varying amounts as indicated in table 2.1 below.[4]

Table 2.1: A chart showing the composition variation of the compounds in several bauxite samples.[4]

Compound	Composition (%)						
	1	2	3	4	5	6	7
H_2O	28.08	17.9	13.74	13.14	9.88	14.98	14.24
SiO_2	9.7	18.9	13.96	20.5	1.36	17.84	5.36
Al_2O_3	56.31	52.48	67.21	60.89	60.66	61.98	73.7
Fe_2O_3	3.1	4.39	0.75	0.55	23.55	0.47	2.28
TiO_2	2.09	2.68	3.22	3.14	3.85	2.85	3.57
CaO	0.22	3.17	0.22	0.43	0.22	0.22	0.4
MgO	0.52	0.4	0.36	0.31	0.5	0.79	0.16
KNaO	0.49	0.43	1.16	1.34	0.37	0.38	0.53

Total	100.51	100.35	100.62	100.3	100.39	100.51	100.24

The first commercially viable process capable of isolating the aluminum metal in bauxite was developed independently by American Charles Martin Hall and Frenchman Paul Héroult in 1886, and named the Hall-Héroult process.[5] Unfortunately, this process was unable to synthesize high purity aluminum on its own and required the help of another process to obtain the high purity alumina needed. This process was developed in 1888 by Austrian chemist Karl Bayer and is now known as the Bayer process, making it possible to isolate high purity alumina from bauxite.[6] Currently, this method still remains the first step in the production of aluminum.

In a very simplified manner the Bayer process consists of several chemical reactions. First, the crushed bauxite is mixed with a hot concentrated solution of sodium hydroxide (NaOH), this transforms the Al_2O_3 and SiO_2 into aqueous salts and isolates the insoluble Fe_2O_3, which is then filtered out.[7] The chemical reactions are shown below.

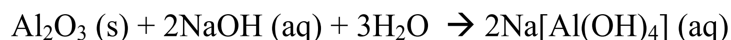

$$Al_2O_3\ (s) + 2NaOH\ (aq) + 3H_2O \rightarrow 2Na[Al(OH)_4]\ (aq)$$

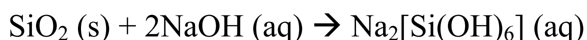

$$SiO_2 (s) + 2NaOH (aq) \rightarrow Na_2[Si(OH)_6] (aq)$$

To separate the Al_2O_3, this aqueous solution is treated with carbon dioxide (CO_2), which serves to precipitate Al_2O_3 by forming aqueous carbonic acid (H_2CO_3).[7]

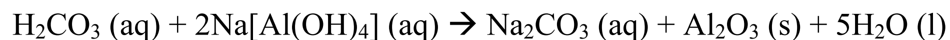

$$H_2CO_3 (aq) + 2Na[Al(OH)_4] (aq) \rightarrow Na_2CO_3 (aq) + Al_2O_3 (s) + 5H_2O (l)$$

After obtaining high purity alumina, the Hall-Héroult process is used to convert the alumina to aluminum. This is an electrolytic process which involves dissolving alumina in a carbon lined molten bath of cryolite (Na_3AlF_6). The carbon serves as the anode and an electrical bias of 3-5 V is applied, resulting in reduction of the alumina to form liquid aluminum, which is denser than the molten cryolite and sinks to the bottom, where it is collected.[8] The chemical reaction that occurs is shown below.

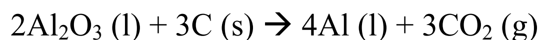

$$2Al_2O_3 (l) + 3C (s) \rightarrow 4Al (l) + 3CO_2 (g)$$

With a viable process for making aluminum, the manufacturing capacity and markets for aluminum increased rapidly as more and more uses were discovered. The increase in the production of aluminum is shown below in Figure 2.1.

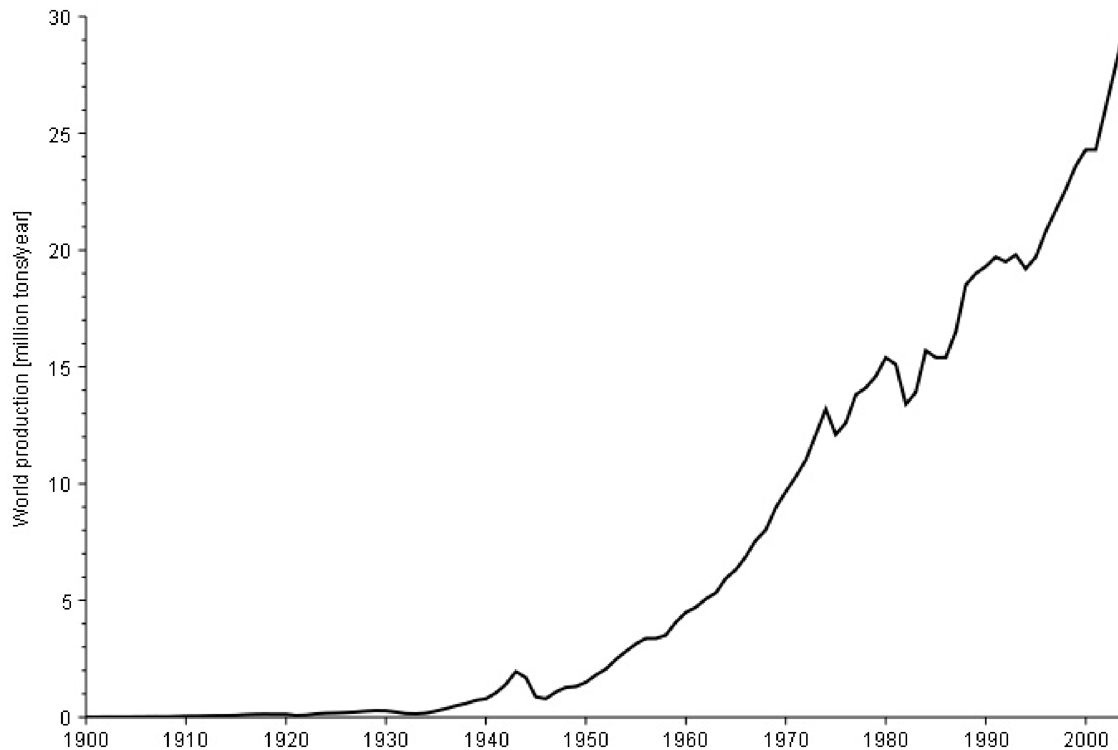

Figure 2.1: Graph showing the increase in commercial aluminum production from 1900-2000.[9]

As aluminum became used in increasingly wider circles, attention was gradually focused on anodic coatings on aluminum pieces and the many advantages that they offer.

2.2 Properties of aluminum and aluminum oxide

Aluminum has an atomic number of 13 and an atomic weight of 26.98.[10] In its highest purity, ultra pure aluminum (99.9998%) has a density of 2.69808 g / cm^3 at 25°C and exhibits a face centered cubic crystal structure with an edge length of 4.0496 Å.[11, 12] At room temperature Al has a tensile yield strength (0.2% offset) of 10 MPa and

a tensile strength of 45 MPa.[13] Table 2.2 shows a summary of the physical properties of aluminum.[13]

Table 2.2: A summary of the physical properties of pure aluminum.[13]

Property	Value
Lattice constant	4.0496 Å at 298 K
Density (solid)	2697 - 2699 kg / m^3
Density (liquid)	2357 kg / m^3 at 973 K
	2303 kg / m^3 at 1173 K
Coefficient of thermal expansion	23 x 10^{-6} K^{-1} at 298 K
Thermal conductivity	2.37 W / cm K at 298 K
Volume resistivity	2.655 x 10^{-8} Ω m
Magnetic susceptibility	16 x 10^{-3} g / m^3 atom at 298 K
Surface tension	868 dyne / cm at melting point
Viscosity	0.012 poise at melting point
Melting point	933.5 K
Boiling point	2767 K
Heat of fusion	397 J / g
Heat of vaporization	1.08 x 10^{-4} J / g
Heat capacity	0.90 J / g K

Of these properties, the thermal conductivity and resistivity are important because they give aluminum various applications in the electronics industry. Aluminum also exhibits high reflectivity in excess of 90% for smooth surfaces at light wavelengths from 0.9 – 12.0 µm.[13] However, as the roughness increases the reflectivity drops drastically, to 15 – 25% for sandblasted aluminum.[13] The naturally occurring isotope, Al^{27}, was used extensively in early nuclear reactors as protective sheaths because of the short half-life of its resulting irradiated product.[10] Another advantageous property of aluminum is its stability in many oxidizing environments. This results from the nascent aluminum oxide film that is continually present and heals rapidly when damaged.[13]

The aluminum oxide film that forms on the surface of aluminum is a ceramic material. In fact, there are several different forms of bulk aluminum oxide with various crystal structures, as was mentioned briefly in the previous section. There are tri-hydrated aluminas such as gibbsite, bayerite, and nordstrandite ($Al_2O_3 \cdot 3H_2O$), and monohydrated boehemite and diaspore ($Al_2O_3 \cdot H_2O$).[14] In non-hydrated form, pure alumina is known as corundum (α-Al_2O_3) if it is polycrystalline, or sapphire if it is single crystalline.[15] They exhibit a rhombohedral crystal structure with unit cell parameters a = 4.758 Å and c = 12.991 Å.[15] Table 2.3 lists some of the properties of polycrystalline α-Al_2O_3.[14, 15]

Table 2.3: Physical properties of the polycrystalline α-Al_2O_3 phase.[14, 15]

Property	Value
Density (solid)	3.97 g / cm^3
Coefficient of thermal expansion	5.4 x 10^{-6} K^{-1} at 298 K
Thermal conductivity	0.360 J / cm s K
Volume resistivity	1 x 10^{13} Ω cm at 298 K
Dielectric constant	12.3
Magnetic susceptibility	-0.23 x 10^{-6}
Melting point	2051°C
Boiling point	3530°C
Heat of fusion	26 kcal / mol at 298 K
Heat of vaporization	443 kcal / mol at 298 K
Heat capacity	15.5 J / mol K at 298 K

Naturally, the different phases of alumina have slightly different properties. The importance of these properties is seen in the wide range of applications that there are for aluminum oxide. Additionally, corundum has a hardness of nine on the Mohs hardness scale making it the second hardest mineral, behind only diamond. This hardness gives

it many useful applications in cutting tools. The advantageous insulating and dielectric properties result in uses as spark plug insulators and housings for electrical parts.[15] It is these insulating properties that make the thin protective alumina film so useful. Compared to the other forms of alumina mentioned above, the thin alumina film that forms naturally on aluminum has an amorphous structure. The beneficial effects of this thin oxide layer have led to numerous applications for aluminum pieces with protective anodic coatings in areas from structural and architectural applications. More information on applications of anodized aluminum is provided in section 2.5. To tailor the materials for specific applications, the character of the anodized aluminum oxide coating can be influenced by varying the conditions under which it forms. To examine these effects, the preparation and synthesis of an anodized aluminum oxide layer will now be examined.

2.3 Synthesis of anodized aluminum oxide

2.3.1 Anodization of aluminum:

Anodization is a simple means of producing an oxide coating or film on a metal; it can be performed on metals such as aluminum, titanium, or zirconium, to name a few. In the process of anodization the metal piece is made the anode by connecting it to the positive terminal of a direct current power supply and immersing it in an electrolyte solution. Another material, non-reactive to the electrolyte, such as carbon or platinum is connected to the negative terminal of the power supply and serves as the cathode. When the power supply is switched on and a voltage is applied across the anode and cathode the flow of ions commences, shown in simplified form in Figure 2.2 below.

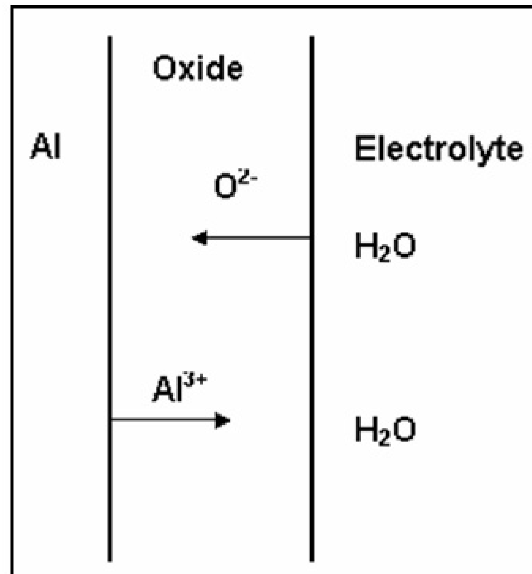

Figure 2.2: Directional movement of ions in the anodization process of aluminum.[16]

The real version is somewhat more complicated as there are separate reactions occurring at the cathode in addition to the reactions shown above occurring at the metal/oxide and oxide/electrolyte interfaces at the anode. These are the reactions that occur at each site:[16]

metal/oxide interface: $2Al + 3O^{2-} \rightarrow Al_2O_3 + 6e^-$

oxide/electrolyte interface: $2Al^{3+} + 3H_2O \rightarrow Al_2O_3 + 6H^+$

partial dissolution of the oxide: $Al_2O_3 \rightarrow 2Al^{3+} + 3O^{2-}$

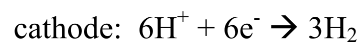
cathode: $6H^+ + 6e^- \rightarrow 3H_2$

These reactions combine to produce an overall reaction for the anodization process of:

$$2Al + 3H_2O \rightarrow Al_2O_3 + 3H_2$$

With anodization there is always a balance between the growth of the oxide and its dissolution, provided that the oxide forms faster than it dissolves there will be continued growth and thickening of the oxide layer.

One critical aspect of the anodizing process is the type of electrolyte that is used. The type of electrolyte in turn influences how the formed oxide behaves in the solution and alters the structure of anodic film that is formed. There are two different types of oxides that can form based on the type of electrolyte that is used, as illustrated in Figure 2.3 below.

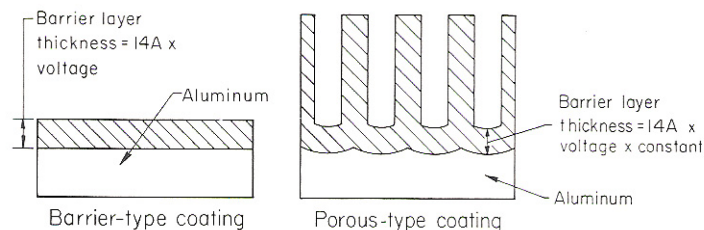

Figure 2.3: Schematic diagram showing the two main types of anodic coatings.[17]

Using a neutral electrolyte with a pH of 7-8, such as phosphates, citrates, tartrates, and borates, a nonporous amorphous barrier oxide is formed with a thickness proportional to the applied voltage at about 14 Å / V and limited to a few hundred nanometers.[18, 19] Part of the reason for the formation of this barrier oxide is that the oxide that is formed is stable in the electrolyte and does not dissolve. Figure 2.4 shows an image of this nonporous barrier oxide.

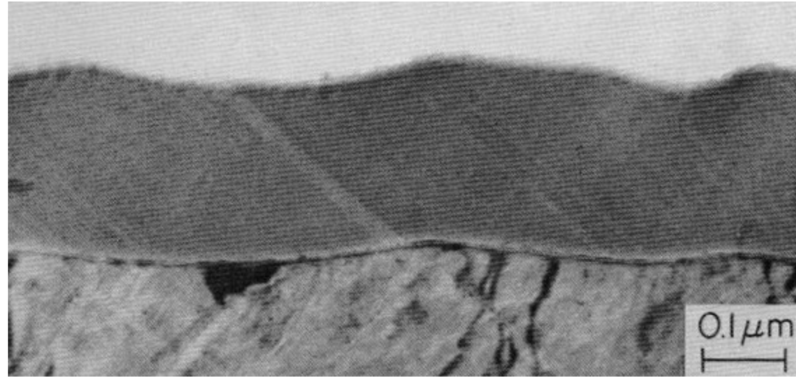

Figure 2.4: Cross sectional image of a nonporous barrier oxide formed in a tartrate solution on aluminum.[20]

When the electrolyte is acidic, such as in sulfuric, oxalic, or phosphoric acid solutions, porous oxides develop because the acidic electrolyte promotes oxide dissolution.[21] An illustration of the idealized porous structure is shown in Figure 2.5.

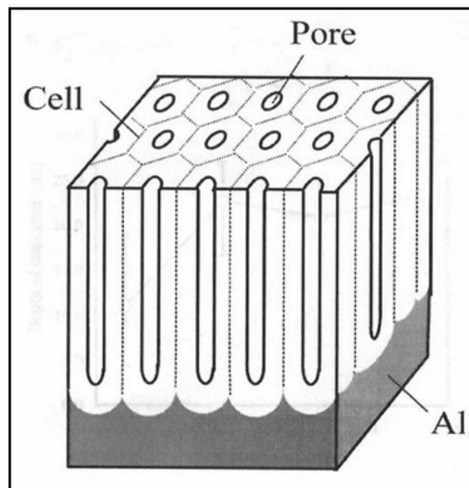

Figure 2.5: Idealized structure of a porous anodic film.[22]

For this research, the porous structure is the subject of interest. With a clear background on aluminum and the basics of anodization, the formation of porous aluminum oxide will now be discussed.

2.3.2 Anodized aluminum oxide on bulk aluminum

2.3.2.1 History of AAO on bulk aluminum

The first studies on the formation of porous anodized aluminum oxide were published in 1941 and 1944 by Edwards and Keller and proposed a preliminary theory for the formation of the pores.[23, 24] It was not until 1953 that clear structural details of the pores were disclosed and a more refined theory of pore growth was published.[25] The authors of that publication, F. Keller, M. S. Hunter, and D. L. Robinson, noted that initially high current flows and a thin barrier oxide is formed and thereafter the current decreases to a steady state value as anodization proceeds.[25] At the time, they proposed that growth of the pores occurred in an outward manner from the center of pores and therefore resulted in the star shaped pore due to the presence of the six neighboring cells, as shown in Figure 2.6.[25]

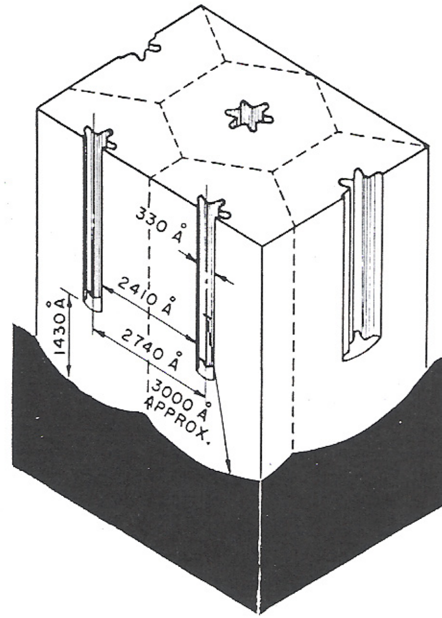

Figure 2.6: Early proposed pore structure of AAO produced in a 120 V phosphoric acid solution, including relevant dimensions.[25]

However, lacking clear images of the porous oxide it was difficult to accurately assess the structure of the pores. It would be several years before imaging techniques allowed for an accurate analysis of the pore structure.

Soon afterwards, a comprehensive study was released which outlined the six major factors that influence the growth of the pores: electrolyte type, electrolyte concentration, electrolyte temperature, voltage, current density, and time.[26] The key result from this study was that it was noted that the oxide layer forms only as fast as dissolution occurs at the pore base.[26, 27] The first direct observation of a cross-section of a porous anodic film, shown in Figure 2.7, was made in 1968 and confirms the scalloped shape of the pore bottom as inferred in previous studies.[28]

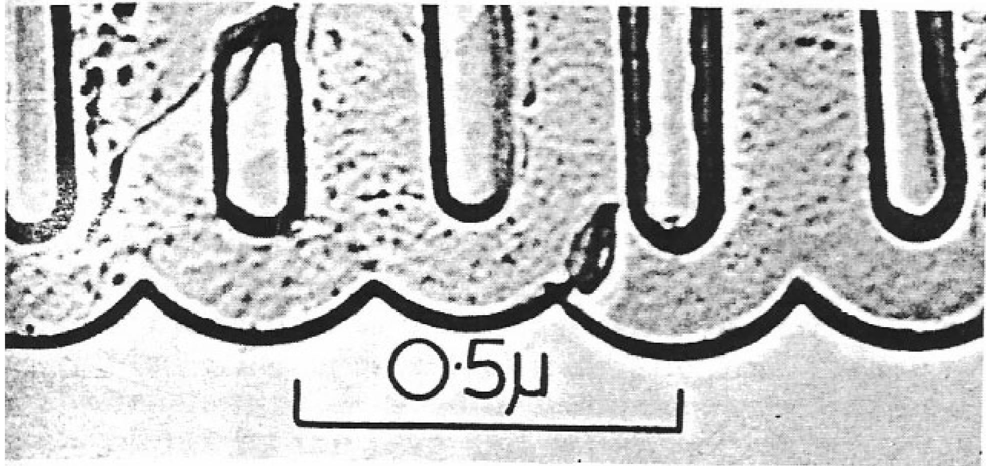

Figure 2.7: Electron microscope image of the cross-section of a porous alumina film anodized in 4 wt. % phosphoric acid at 120 V.[28]

Underneath each pore there is a thin layer of barrier oxide whose thickness depends on the anodizing voltage; this layer serves as the interface between the porous structure and the bulk aluminum.[29] In 1970 it was discovered that the average field across this barrier layer determines the film growth rate and the local field at the barrier layer/electrolyte interface determines the dissolution rate.[30] Thus, considering these competing forces and the growth characteristics of the pores, mathematical equations were developed to predict the geometric shape of the pores as shown below in Figure 2.8.

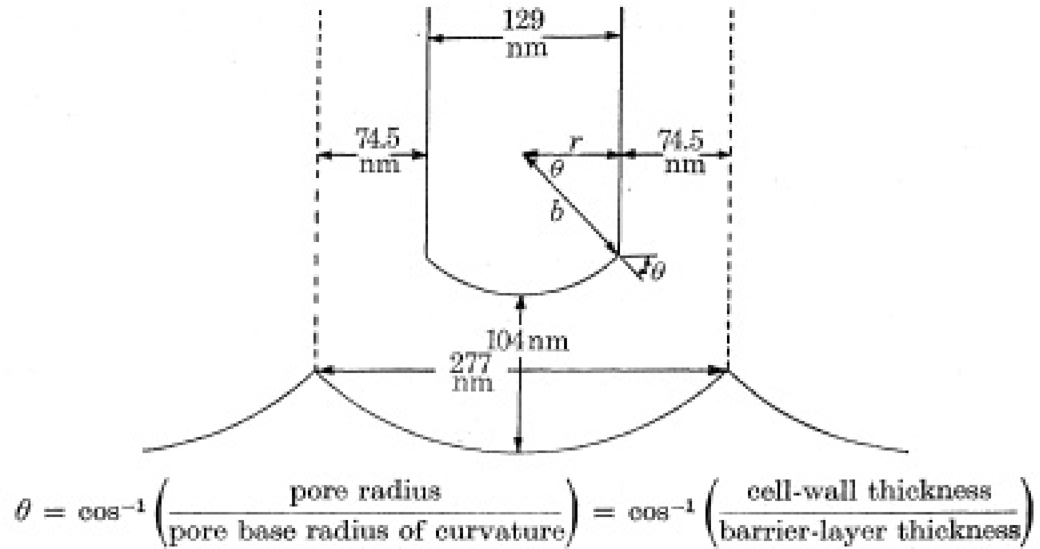

Figure 2.8: Schematic diagram showing the shape of the barrier layer and pore structure and the equations that model their shapes.[30]

2.3.2.2 Nucleation and growth of the porous layer

The growth of the porous layer can be analyzed by looking at how changes in the six major factors that influence pore growth, mentioned above, affect the character of the porous film, beginning with an analysis of the influence of the anodizing voltage. Naturally, the anodizing voltage is interrelated with the current density that the sample experiences for samples of the same size. Figure 2.9 shows the graphs for constant voltage and constant current anodization.

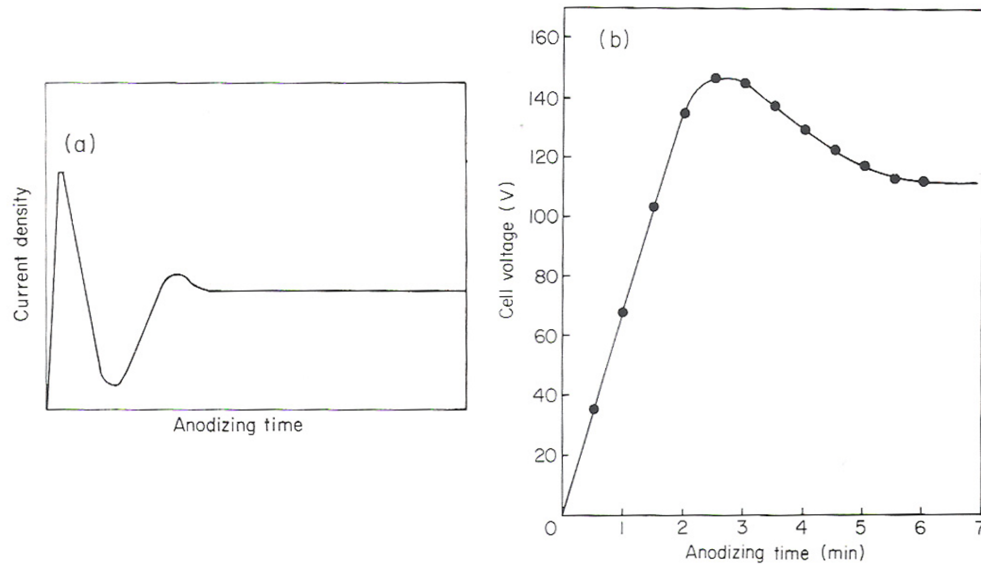

Figure 2.9: (A) Anodization of aluminum at constant voltage, (B) anodization of aluminum at constant current density.[31]

The initial spike and subsequent decrease of the current density in potentiostatic anodization is due to the initial formation of a barrier oxide film.[31] As this barrier oxide film reaches a certain thickness, pores nucleate across the surface in depressions where the oxide film is thinner, which allows field-enhanced dissolution to take place, accelerating the rate of oxide dissolution at the pore base.[32] These depressions typically result from the original roughness and initial contours of the Al surface. Field-enhanced dissolution occurs in areas where the angle of the oxide/metal interface is larger than 180° as shown by point A in Figure 2.10, where the dashed lines indicates the boundary of the initial oxide film formed at two different anodizing voltages.[33]

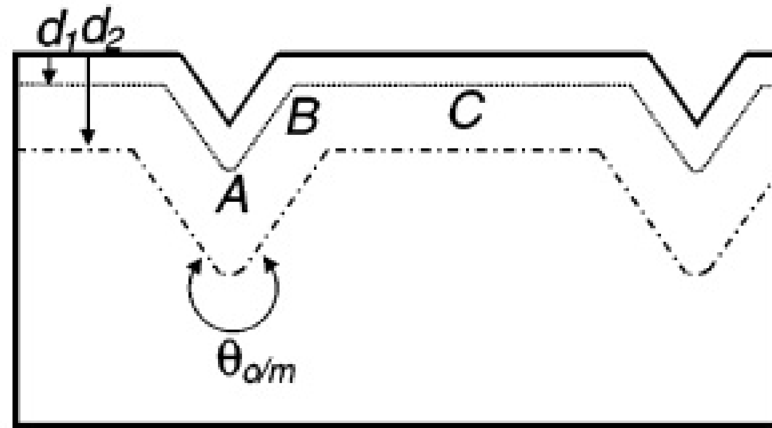

Figure 2.10: Influence of the surface morphology on field-enhanced dissolution, showing the dependence of field-enhancement on the angle Θ.[33]

When Θ is less than or equal to 180°, such as at points B and C in Figure 2.10, no field-enhancement occurs and the pores are therefore unable to nucleate.[33] The field-enhanced dissolution works in several ways. First, the higher local field encourages the migration of O^{2-} and OH^- ions through the barrier layer at the pore base leading to increased formation of oxide at the oxide/metal interface and increased dissolution at the oxide/electrolyte interface.[30, 33, 34] Second, the growth of the pores results in an increased flow of current to the area which locally increases temperature and further hastens ionic migration thereby increasing the rates of dissolution and oxide formation.[30, 35] After initial nucleation the pores will continue to grow at a steady-state indefinitely until the available aluminum is consumed.

The electrolyte solution used for anodization also has a big influence on the porous structure. Naturally, a more acidic electrolyte will result in faster dissolution and the presence of more ionic conductors will also increase the anodization rate. The

effect that the electrolyte solution has on the current density during anodization is shown in Figure 2.11.

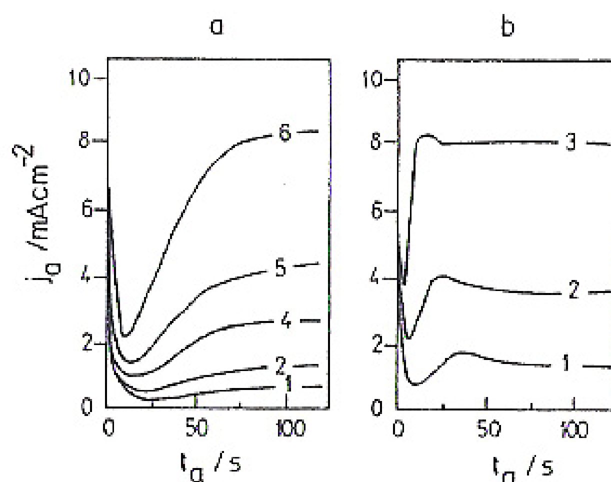

Figure 2.11: Graphs showing the influence of the electrolyte solution and anodization voltage on the current density. (A) 0.2 M oxalic acid and (B) 0.5 M sulfuric acid at different voltages: 1 = 5 V, 2 = 10 V, 3 = 15 V, 4 = 20 V, 5 = 30 V, 6 = 40 V.[36]

It can be seen in comparing the oxalic and sulfuric acid graphs that the stronger sulfuric acid shows a much higher ionic activity, resulting in a larger current density than oxalic acid solutions at the same applied voltage. The strength and activity of the acid also seems to influence the size of the pores.

The size of the pores in any porous film is linearly dependent on the anodization voltage, so that larger voltages lead to larger pores. In addition, anodization results in a pore spacing or center-to-center distance equivalent to about twice the diameter of the pores. This is called the interpore distance and is therefore also related to the size of the pores. It is also typical in the literature to see references to the cell size which is merely the area surrounding the pore that is half the interpore distance towards the neighboring

pores on each side, as illustrated in Figure 2.5, which is also equivalent to twice the pore diameter. Figure 2.12 shows the effect of the type of electrolyte and the anodizing voltage on the interpore distance and cell size.

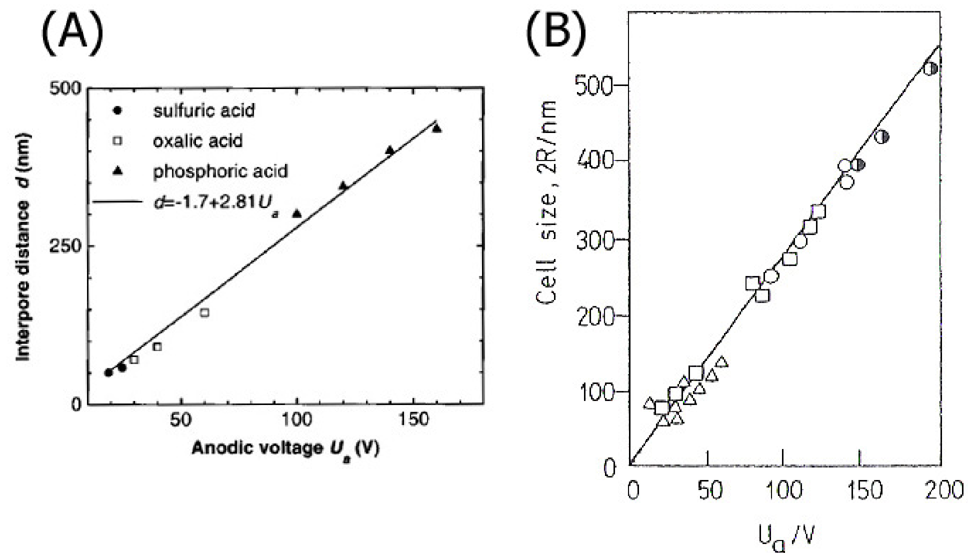

Figure 2.12: The variation in the interpore distance (A) and cell size (B) are shown as a consequence of the electrolyte and anodization voltage. Shown in (A): phosphoric acid, ▲, sulfuric acid, ●, oxalic acid, □. In (B): oxalic acid, △, phosphoric acid, □, glycolic acid, ○, tartaric acid, ❍.[37, 38]

Based on the experimental data available, equations have been developed to model the dependence of the cell size on the anodization voltage, the lines for these equations are plotted in each of the graphs of Figure 2.12. According to the value of the voltage there are two different equations for the dependence of the interpore distance or cell size, d, on the applied voltage, U_a:[38]

For $U_a < 20V$: $d = 14.5 + 2.0\ U_a$

For $U_a > 20V$: $d = -1.7 + 2.81\ U_a$

As useful as this data is, it overlooks the fact that some electrolyte solutions are better suited for certain pore sizes than others based upon their chemistry and how they affect the aluminum under an applied potential. For producing pore sizes of a desired value, the primary anodizing electrolytes, oxalic acid, sulfuric acid, and phosphoric acid are generally used in the regimes shown in Figure 2.13.

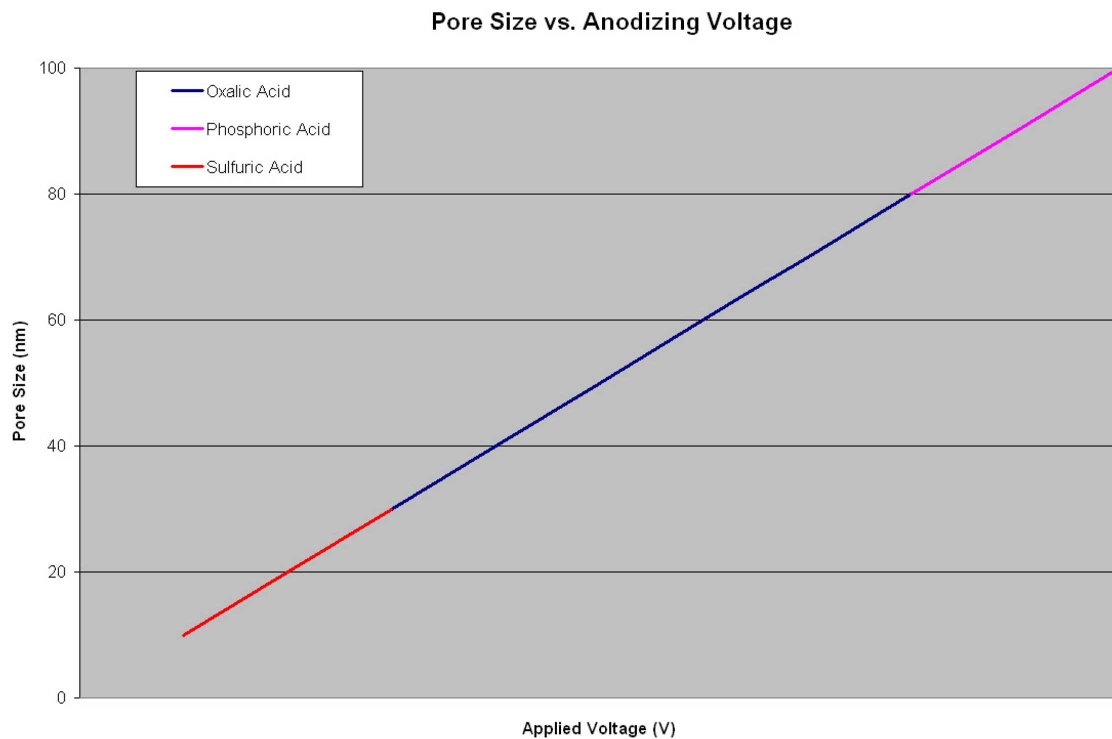

Figure 2.13: Optimal pore sizes for the typically used anodizing solutions of oxalic, sulfuric, and phosphoric acids in relation to the applied voltage.[37, 39, 40, 41]

The final variable of the six major parameters, the temperature of the electrolyte solution has a different effect depending on the type of anodization that is used. For potentiostatic anodization, which is the type of anodization used for this and other

similar research, temperature does not appear to influence the pore diameter or interpore spacing.[42] However, for galvanostatic anodization, anodization at constant current density, an increase in temperature results in an increase in pore size and interpore spacing.[42] These effects are shown graphically in Figure 2.14.

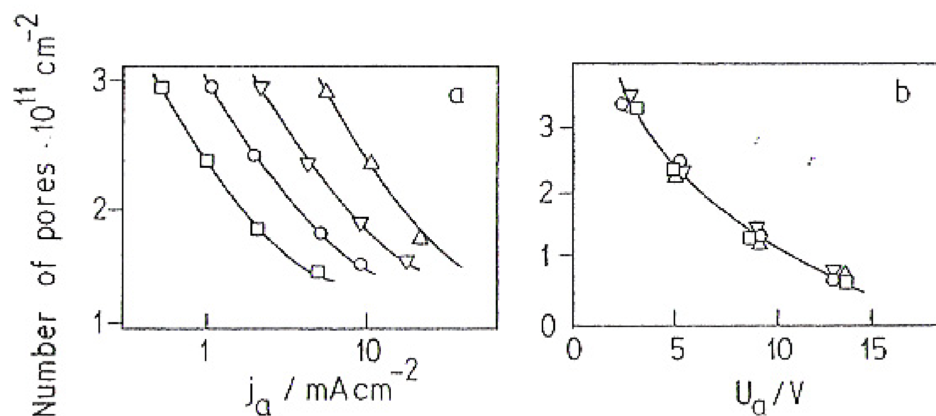

Figure 2.14: Influence of temperature on the pore density for galvanostatic anodization (A) and potentiostatic anodization (B), at anodization temperatures of 10°C, □, 20°C, ○, 30°C, ▽, 40°C, △.[42]

Despite the fact that temperature does not influence the size of the pores in potentiostatic anodization, there is evidence that a lower temperature does promote a more regular pore structure. The process of pore ordering will be discussed next, in section 2.3.2.3.

2.3.2.3 Self-ordering in the porous layer

As mentioned previously in section 2.3.2.2, the pores nucleate in depressions on the surface of the aluminum after the formation of a thin barrier oxide layer. This step is then followed by pore growth into the aluminum by field-enhanced dissolution of the

oxide layer. By analyzing the surface at the underside of the pore bottom it is observed that the pores are much more ordered at the bottom than they are on the top surface. This has been observed in many studies and summarized by Thompson and Wood.[18] It can therefore be inferred that the ordering develops during growth of the porous layer. Figure 2.15 shows the effect of this self-organization process versus the thickness of the anodized layer, where the anodization time increases from (A) - (C).

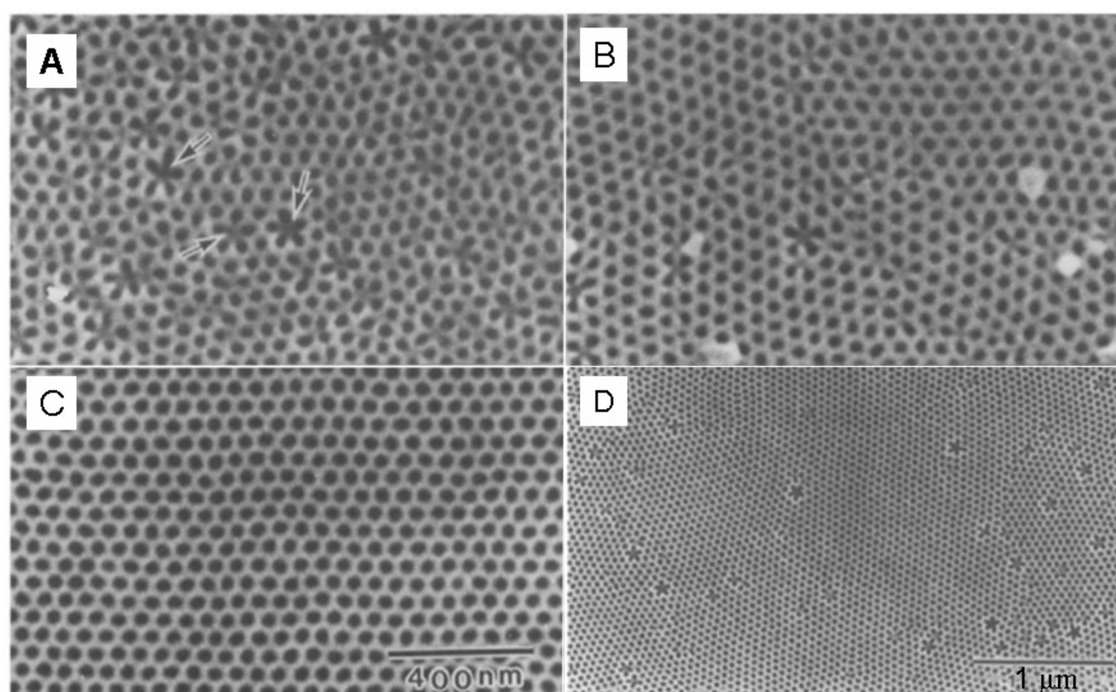

Figure 2.15: Variation of the regularity of the porous structure as the anodized time and porous layer thickness increases; samples anodized in 0.5 M H_2SO_4 at 25 V for (A) 9 min [2.4 µm], (B) 36 min [10.6 µm], and (C) 750 min [202 µm]; (D) shows a lower magnification image of (C).[43]

The ordering and regularity of the pores are not only influenced by the anodization time. For each of the primary electrolyte solutions that are used in anodization there exists a certain anodization voltage that promotes in a regularly ordered pore structure

over micrometer sized areas. This ideal voltage coupled with a longer anodizing time will favor the formation of ordered pores. The discovery of this self-ordering voltage was first reported by Masuda and Fukuda in 1995.[44] They obtained an ordered pore structure by anodizing aluminum in 0.3 M oxalic acid at 40 V. Figure 2.16 shows how using the correct anodization voltage is more important than anodization time when the regularity of the pore array is concerned.[43] Using 0.3 M H_2SO_4 the regularity is much better with an anodization voltage of 27 V for a short time of 450 min than it is with a long time anodization of 20 V for 1500 min.[43]

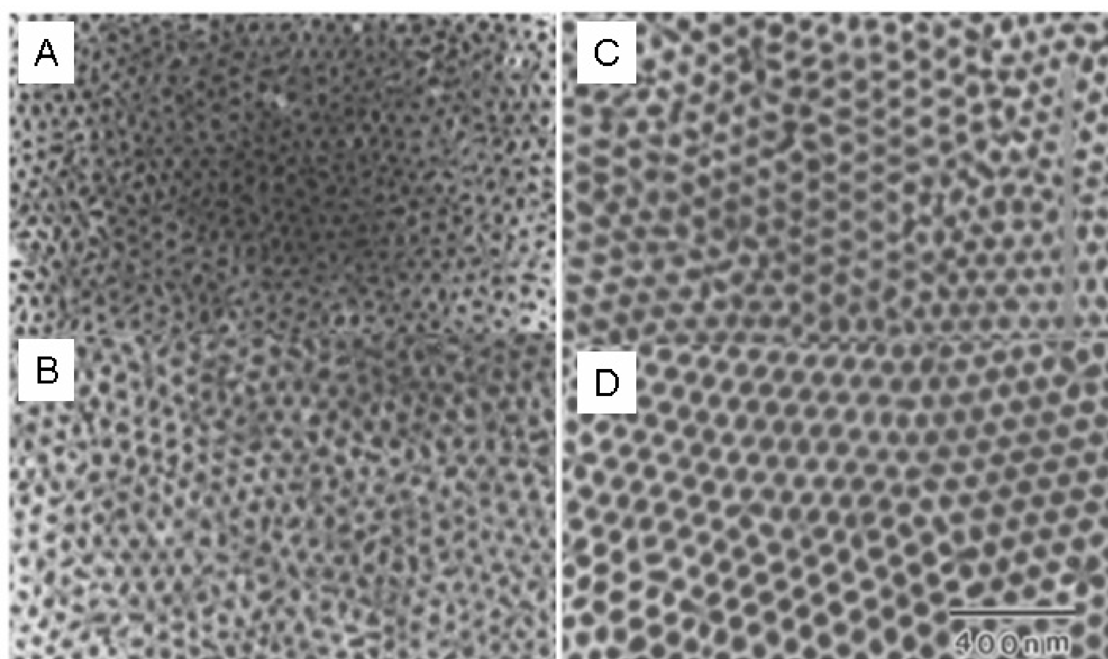

Figure 2.16: Scanning electron microscope images of AAO formed in 0.3 M H_2SO_4 at (A) 20 V for 1500 min, (B) 23 V for 1000 min, (C) 25 V for 706 min, and (D) 27 V for 450 min.[43]

Depending on the type of electrolyte solution the ideal ordering voltage varies over a considerable range from 25 V to 240 V and results a variety of pore sizes.[45] A summary

of the self-ordering conditions that have been determined so far are presented in Figure 2.17.

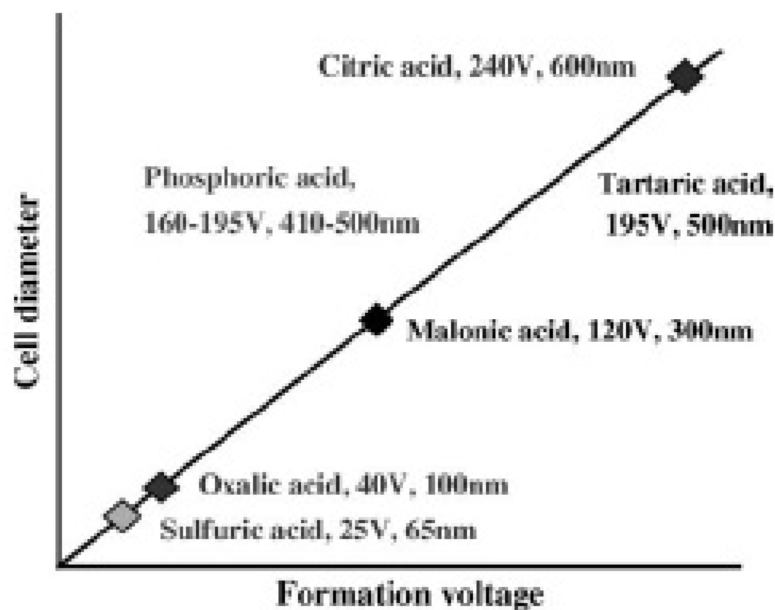

Figure 2.17: A summary of the self-ordering conditions for different electrolyte solutions and the resulting cell sizes.[45]

The exact mechanism for this self-ordering behavior is not exactly known. It seems that there must be some balance of forces, either mechanical, electrical or a combination of both, between neighboring pores that eventually evens out, resulting in an ordered pore structure. One theory of the mechanism of self-adjustment by neighboring pores is based upon the electric field present at the bottom of the pores. To test their theory the authors used a very thin stripe of aluminum, insulated on either side, with a thickness designed to only accommodate a single file row of pores, as shown in Figure 2.18.[46]

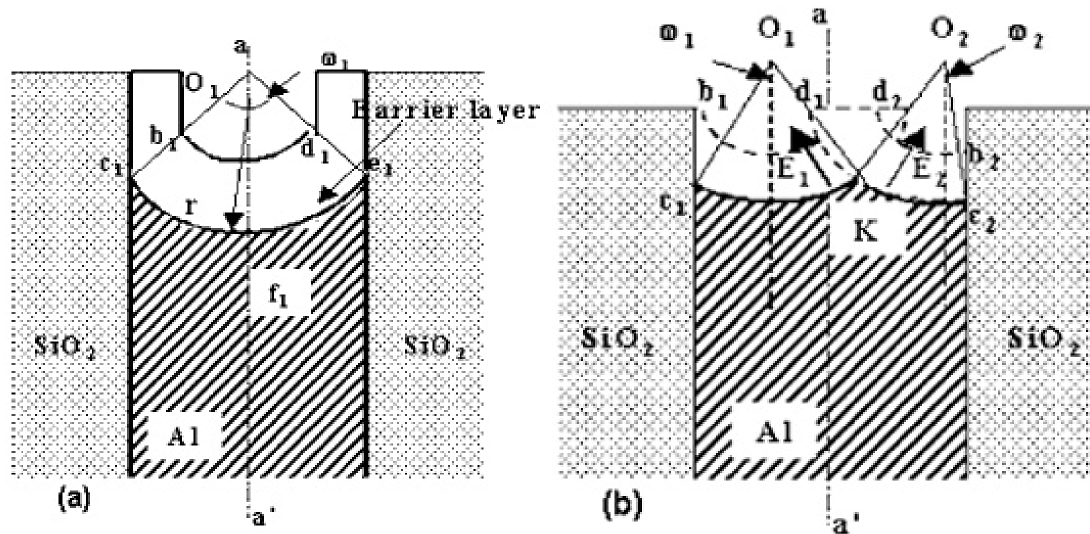

Figure 2.18: Experimental setup depicting (A) a single pore nucleating and (B) two pores attempting to nucleate in a thin strip of aluminum insulated on either side.[46]

The result of these two pores in close proximity to each other is that each pore has its own electric field acting towards the center or lowest point in their respective pore bases. Because the pores are close together, their electric fields will overlap to some degree with a maximum concentration and an enhanced field occurring around point K in Figure 2.18 (B).[46] This will have the result of increasing the dissolution rate at this point and will gradually push each respective pore center towards this centerline position.[46] Finally, the two pores will merge to become one pore, in a manner similar to that shown in Figure 2.18 (A). If the case of a large area of exposed aluminum is considered, it can be envisioned how this effect would work on a two-dimensional surface to develop order over a long anodizing time.

Another theory that may work in a similar fashion has been proposed by the authors of the study mentioned in Figure 2.17 above, Ono, Saito, and Asoh. They

propose that these self-ordering conditions occur only at a critical high current density range which forces the cells to cluster together in a tightly packed arrangement.[45] It may be that this critical high current density promotes the electric fields acting on each surface depressions to ideally space themselves in such a way as to minimize repulsive forces. This point could be similar to the ordering mechanism originally proposed by Jessensky, Müller, and Gösele in 1998. They stated that the mechanical stress resulting from the volume expansion that occurs during conversion of Al to the lower density Al_2O_3 at the metal/oxide interface is the basis of the repulsive forces between the pores.[47] The effect of this volume expansion on the pore during anodization is illustrated in Figure 2.19.

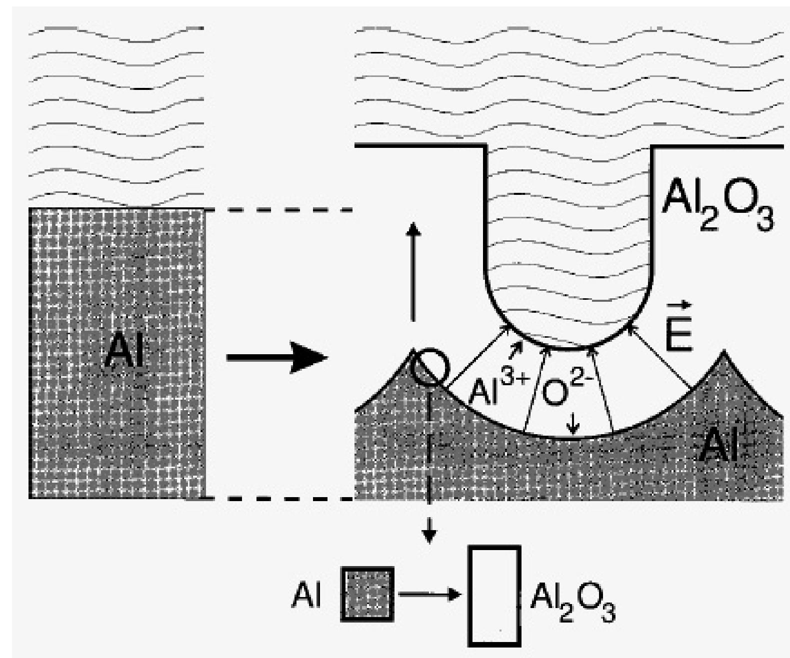

Figure 2.19: Diagram showing the volume expansion of aluminum to aluminum oxide during anodization and the formation of a pore.[47]

A more in-depth version of this proposed mechanism was published in 2002 which showed how the self-ordering regimes in different electrolytes all correlate to a porous film with approximately 10% porosity.[48] Table 2.2 shows the relationship between the pore diameter, interpore distance, and porosity for oxalic, sulfuric, and phosphoric acid electrolytes.

Table 2.4: Structural measurements of self-ordered porous alumina for different electrolytes.[48]

electrolyte	interpore distance D_{int}	inner wall thickness D_{inner}	pore diameter D_p (= $2r$)	porosity P
H_2SO_4 25 V, 0.3 M	66.3 nm	7.2 nm	24 nm	12%
$(COOH)_2$ 40 V, 0.3 M	105 nm	9.1 nm	31 nm	8%
H_3PO_4 195 V, 0.1 M	501 nm	54 nm	158.4 nm	9%

This correlation with 10% porosity is thought to mirror the volume expansion that occurs in the conversion from aluminum to alumina because a 10% porosity corresponds to a volume expansion of about 1.2.[48] Concurring evidence is also presented in other studies.[49, 50]

In order to reach this certain level of porosity, the pores that nucleate in a less ordered fashion on the surface must, at some point, merge with other pores to create the more ordered structure that develops during the course of longer anodization times.

From experimental evidence there seems to be a limit to the size of the areas that have perfect pore ordering. These areas of well-ordered pores look like grains and can

be referred to as ordered domains. An example of these ordered domains is shown in Figure 2.20.

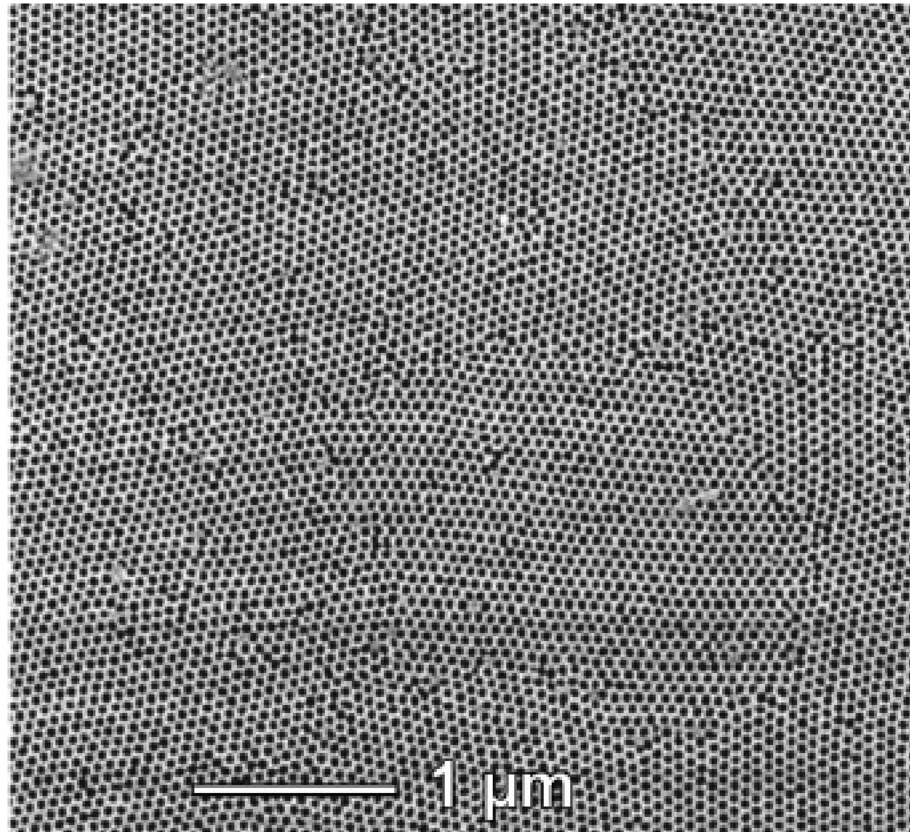

Figure 2.20: Low magnification SEM image showing the presence of ordered domains in the AAO.[37]

The grain size of the aluminum has some influence over this and annealing the substrates prior to anodization can increase the grain size, improving regularity to some degree.[51] However, the perfectly ordered pore areas still form in certain domains that do not necessarily match up with the grain size of the material. In further proof that the grain size is not a limiting factor in the size of the ordered domains, single crystal aluminum was anodized and the largest ordered domains formed were around 10 x 10

μm.[52] It has also been shown that increasing anodization time results in an increase in the size of these ordered domains; but this also has its limitations.[53] A graph showing the relationship between anodization time and size of the ordered domains is presented in Figure 2.21.

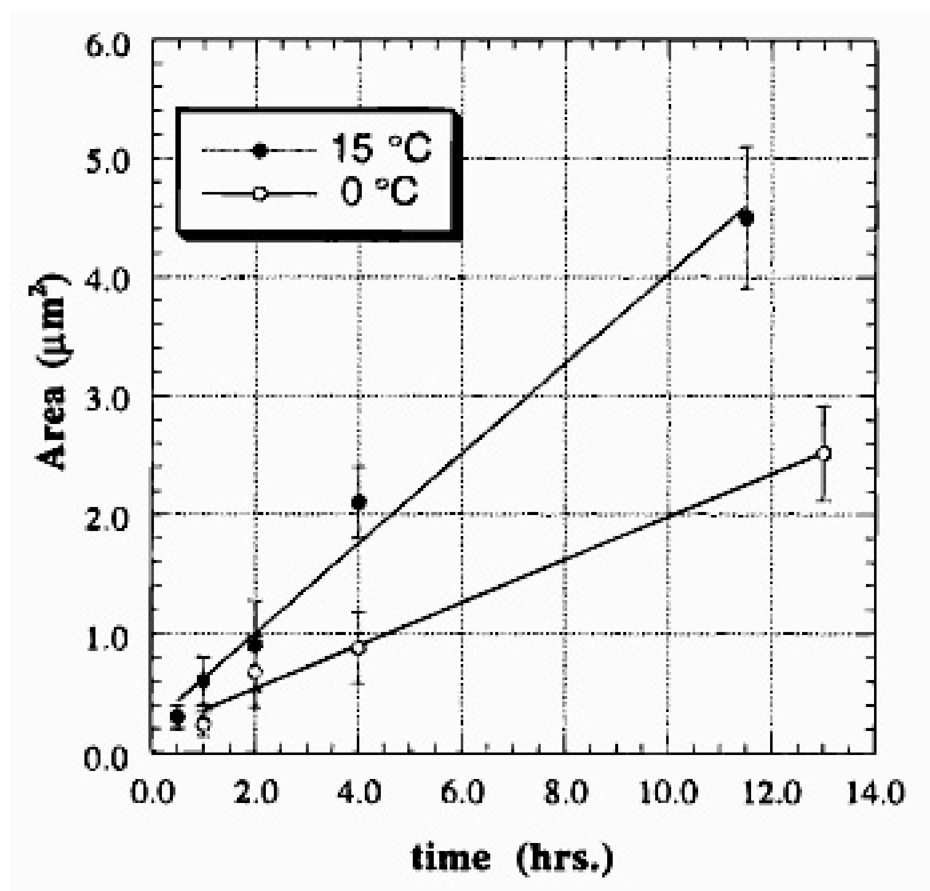

Figure 2.21: Graph showing the increasing size of the ordered domain size with increasing anodization time for a sample anodized in 0.3 M oxalic acid at 40 V.[53]

Another factor that would seemingly influence the size and nature of the ordered pore domains would be the quality of the starting aluminum surface. As pore formation starts in depressions or concavities on the surface it would naturally seem to follow that

the roughness of the original surface of the aluminum would influence ordering of the pores. However, this is true only to an extent. In many early studies of porous aluminum films, pre-anodization surface treatments such as mechanical polishing, and in some cases electropolishing, were performed to generate a smoother aluminum surface in hope of creating a more regular porous structure.[54, 55, 56] This has been shown to be a prerequisite to forming ordered pore structures but beyond a certain threshold roughness it does not seem to influence the ordering much further.[57] Typically a mechanical polishing step will be followed by an electropolishing step using perchloric acid or phosphoric and sulfuric acid based solutions, the result of these steps would be an RMS surface roughness on the order of 3 nm over a 3 μm^2 area.[37, 56, 57] Certain electropolishing conditions are purposely used because they generate a specific surface topology, such as lines or ridges, which can in turn influence the shape of the ordered pore configurations.[58]

Despite all of these factors that influence the ordering, surface roughness, anodization time, grain size, and self-ordering voltage, it is still not possible to obtain perfectly ordered domains in any area larger than on a micrometer scale. Even with the proper self-ordering voltage it is still necessary to anodize for significant amounts of time to create an ordered porous layer, and there is still the problem of a poorly ordered top layer and the large thickness of the porous layer resulting from the long anodizing times. All the images of AAO shown in the previous figures, Figures 2.15 and 2.16, are scanning electron microscope images taken of the bottom of the pores; obtained by dissolving the remaining aluminum and then etching through the barrier layer to expose the underside of the pores. The applications of such a thick porous layer are limited and

it was necessary to create thinner porous layers that still maintained a good deal of periodicity within the pore array. This was accomplished in 1996 by Masuda and Satoh. In that publication, they reported using a two-step anodization process with the capability of fabricating much thinner layers of ordered porous films.[59] A schematic diagram illustrating this simple process is shown in Figure 2.22.

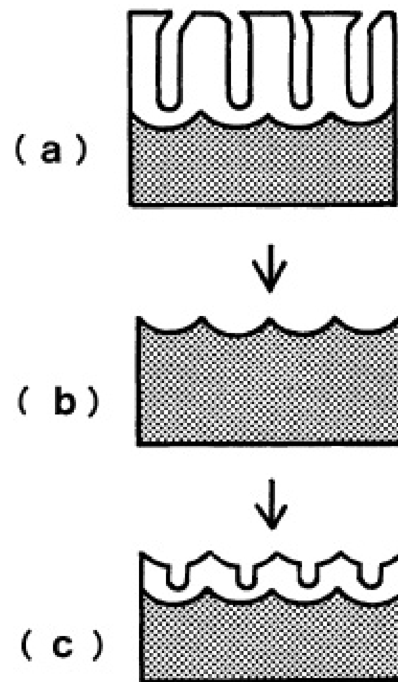

Figure 2.22: Procedure for the process of a two-step anodization of aluminum: (A) initial anodization for a long time, (B) removal of the first anodization layer, (C) growth of the second anodization layer.[59]

This method relies on using the concave shapes formed from the first anodization step as a template for pore nucleation in the second anodization step. The self-organization that takes place over the extended first anodization step is transferred to the aluminum substrate and those ordered concavities dictate the regions where pores form, thereby

maintaining the order that had previously developed. The first anodization layer is removed using a solution of H_3PO_4 and H_2CrO_4 at 60°C. After removing the first anodization layer and anodizing again the new top layer has a much more ordered pore structure, although consistent long-range order is still lacking. The success of this type of surface patterning led to a potential solution to the lack of large area ordered pore arrays; the idea of pre-patterning the aluminum surface over a large area before anodization in order to guide the growth of the pores. This topic will be discussed in the next section.

2.3.3 Imprinting and guided anodization

When considering the information on pore nucleation and growth that was covered in the previous two sub-sections (2.3.2.2 and 2.3.2.3), it should be possible to force the pores to nucleate in pre-determined areas by patterning the surface of the aluminum. If an array of depressions, such as those shown in Figure 2.10, can be created on the surface then those depressions should serve as sites for pore nucleation. The difficulty arises in how to create those small-scale features in such a regular pattern and also to fabricate something that is mechanically robust enough to deform the aluminum surface. Progress towards solving these problems was presented by Masuda et al. in 1997. They reported the successful fabrication of an imprinting master stamp from single-crystal SiC using electron beam lithography with a textured area up to 3 mm x 3 mm.[60] The master stamp was then pressed into the Al surface to transfer the concavities on the SiC stamp to the Al surface and form depressions. Anodization was

subsequently carried out resulting in a perfectly ordered pore array over the imprinted area. Figure 2.23 shows a schematic diagram of the imprinting process in (A) and the difference in pore regularity between the imprinted and non-imprinted areas in (B).

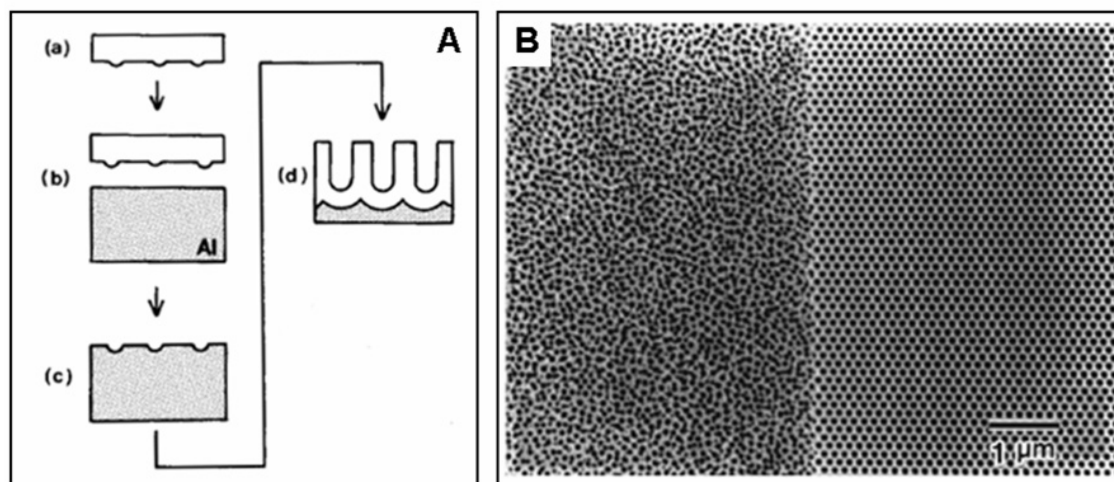

Figure 2.23: Imprinting of aluminum with a schematic diagram showing the imprinting process (A), and SEM images showing the difference between the imprinted and non-imprinted areas (B).[60]

There have been other reports of imprinting of aluminum similar to the process used by Masuda et al. with many of these using metal molds created via electron beam lithography.[61] One of the advantages of the electron beam lithography process is that it is possible to produce any type of pattern that is desired. Using this imprinting technique researchers have been able to produce various pore shapes from triangles and squares to intricate Moiré patterns of circular pores.[62, 63] A critical point of this nanoimprinting is the selection of the proper anodizing conditions. If the anodizing conditions do not generate a pore size and interpore distance that are similar to the size

and spacing of the imprinting master stamp then mismatching surface features such as those shown in Figure 2.24 may be generated.

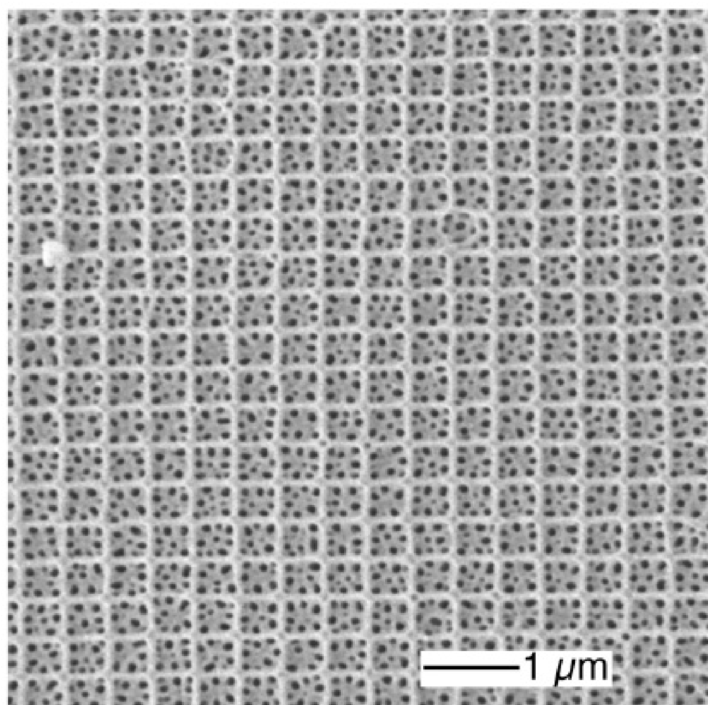

Figure 2.24: SEM image showing the mismatch of imprinting conditions with the anodization conditions.[64]

Here, the imprinted area was much larger than the pore size obtained during anodization resulting in many pores nucleating inside each imprinting site.

Other than electron beam lithography, there are several other methods that have been used to pre-pattern the aluminum surface. Metal molds can be produced from single layer arrays of nanoparticles on the surface of Si or imprinting can be done directly with the nanoparticles.[65, 66] Using the latter technique, pore sizes around 10 nm with a 13 nm spacing have been achieved, albeit ordered only over a very small area.[66] It is also possible to use the nanoimprinting capabilities of an atomic force microscope

(AFM) to pattern the aluminum surface as was demonstrated by Shingubara et al. They were able to achieve separated pore structures with an interpore distance of 65 nm, with smaller distances resulting in conjoined pores and larger distances leading to pores nucleating in between the imprinting sites. These results further underscore the importance of matching the imprinting conditions to the anodization conditions.[67]

Other than providing ideal ordering over a large area, imprinting also provides a means to test the self-ordering properties of AAO. By producing imprinting master stamps with missing imprinting sites it can be tested to see whether the surrounding depressions on the aluminum surface will influence the formation of a pore in the proper location. This was first tested in 2001 when SiC imprinting masters were prepared with single missing sites and with two missing sites next to each other.[68] The results are shown below in Figure 2.25.

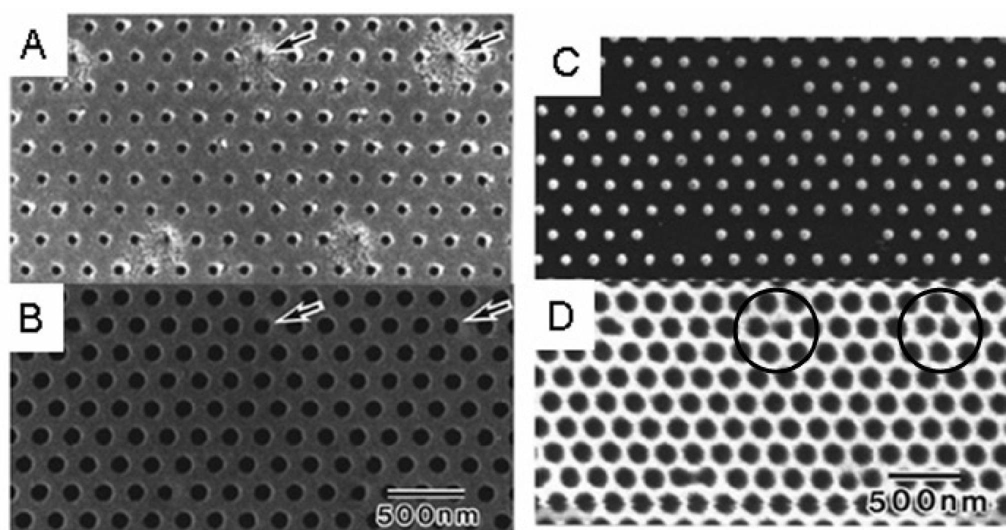

Figure 2.25: Imprinting with a single missing site and the resulting pore array formed after anodization with the arrows indicating the missing sites (A), and after an etching treatment to widen the pores (B). Imprinting with two chained missing sites on the SiC mold (C) and in the anodized pattern, identified by the circles (D).[68]

For the single missing site, nearly perfect order is obtained, the pores may be slightly smaller after anodizing but they are perfectly positioned. When two missing areas are connected the position of the pore varies and perfect order is not preserved.

This demonstration of the self-ordering behavior is important because of the disadvantages of electron beam lithography, the primary method used to create the imprinting master stamps that allow millimeter sized ordered pore arrays. Electron beam lithography is a serial process where each element of the pattern is defined one at a time. This makes it a very slow process and limits its yield. In addition, the time required to define a large area of nanoscale features could be prohibitively long. Proof of the self-ordering behavior makes it possible to define only some of the features on the imprinting master stamp, as the missing features will assemble themselves during anodization. There have been a few reports on the success of this technique in patterning the surface.[69, 70] Consistent with the results presented in Figure 2.25, the ordering is better when there are only single missing imprinting sites than when multiple neighboring sites are missing.

2.3.4 Anodized aluminum oxide on thin film aluminum

In order to realize many potential applications, especially in the emerging nanotechnology and electronics industries it is necessary to form the ordered porous structure on a compatible substrate, such as silicon. This was first demonstrated in 2000, when a 2 μm thin film of aluminum was deposited via thermal evaporation on a silicon substrate.[71] Compared to the anodization of bulk aluminum, there are some

differences in the thin film anodization because of the limited supply of aluminum. The presence of the silicon and the type of doping, whether n- or p-type, must be taken into account, as it is reactive with some electrolyte solutions. Either a non-reactive acid solution must be used or the exposed silicon must be insulated from the electrolyte. The biggest difference is seen in the barrier layer where, instead of forming a typical scalloped bottom, the barrier layer arches up from the silicon/oxide interface and leaves a void underneath each pore, as shown in Figure 2.26.[71]

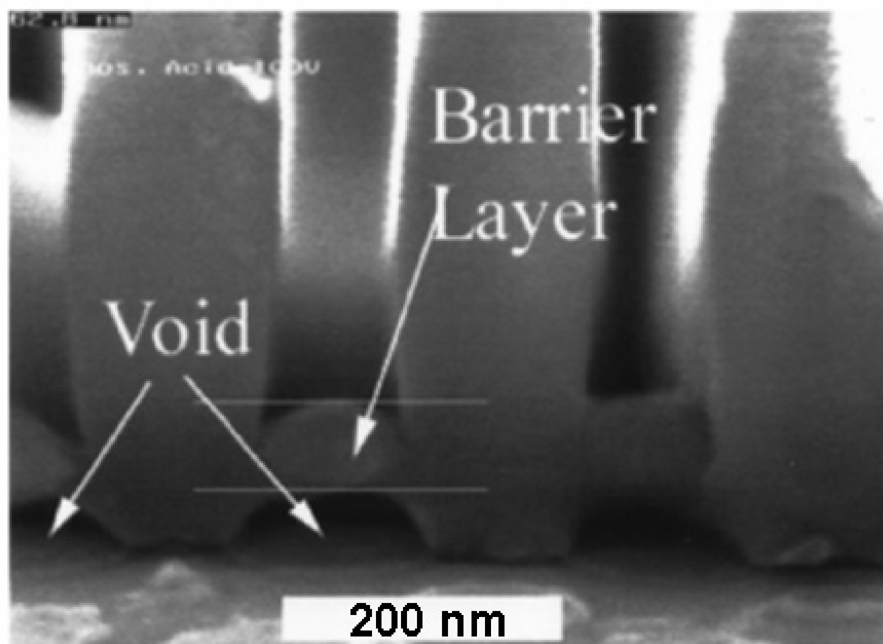

Figure 2.26: SEM image of the barrier layer of an anodized aluminum thin film on a silicon substrate.[71]

The geometry of this barrier layer lends itself to easy removal with a simple etching step in a 5 wt. % phosphoric acid solution.[71] It was later shown that further anodization of p-type or n^+-type Si will result in breaks forming in the barrier layer and SiO_2 dots

forming underneath the pores as the underlying Si is anodized.[72] If anodization continues past this point the SiO_2 will continue to expand and eventually the AAO layer will be separated from the Si substrate.[72] However, n-type Si does not seem to anodize easily and even with long time anodization the AAO layer remains connected to the Si substrate.[72]

The ability to produce AAO on Si substrates was a great leap forward. It did, however, present a problem in obtaining well-ordered pore arrays. Researchers had previously depended on long time anodization resulting in thick aluminum layers for developing very regular pore structures, excluding any type of imprinting technique. Producing thick aluminum films is not such an easy task, especially when a smooth film surface is desired. The two-step anodization helps to improve the ordering but it too requires a relatively thick initial aluminum thickness. A summary of the thickness of aluminum films on Si and the corresponding pore regularity is shown in Table 2.5.

Table 2.5: Relationship between the thickness of the aluminum layer and the regularity of the pore arrays.[51]

Thickness of the evaporated Al layer (μm)	0.3	0.5	1	2	5	6–12	20
Pore regularity of the resulting nanostructures	Poor	Poor	Fair	Fair	Fair	Fair	Good

As the table shows, with an Al thickness of less than 1 μm the ordering of the pores is not very regular and good ordering is only obtained around a starting thickness of 20 μm.

2.4 Electrodeposition of nanowires

Electrodeposition, or electroplating, as it is also known, is a technique used to deposit, or plate, a metal onto an object. The experimental setup works similarly to anodization and involves a power source, an anode and a cathode, and an electrolyte solution known as a bath. In a sense, electrodeposition is the opposite of anodization, instead of removing material from the object as in the case of porous alumina, metal is formed as a coating on the object. It is a very versatile process and virtually any type of metal can be deposited, the only requirement is that some form of the metal's salts must be soluble so that they can exist in aqueous form to comprise the bath solution.[73] The other difference from anodization is that the object to be plated is the cathode and is connected to the negative terminal of the power supply. The metal ions in the bath solution carry a positive charge and are therefore attracted to the negatively charged cathode when a voltage is applied across the anode and cathode. Upon reaching the negatively charged cathode surface there are available electrons to reduce the metal ions, transforming them into a metallic coating. The generalized electrochemical reduction reaction occurring at the cathode for a given metal is:[74]

$$M^{+n} + ne^{-} \rightarrow M$$

A schematic diagram of the electrodeposition set-up is shown in Figure 2.27.

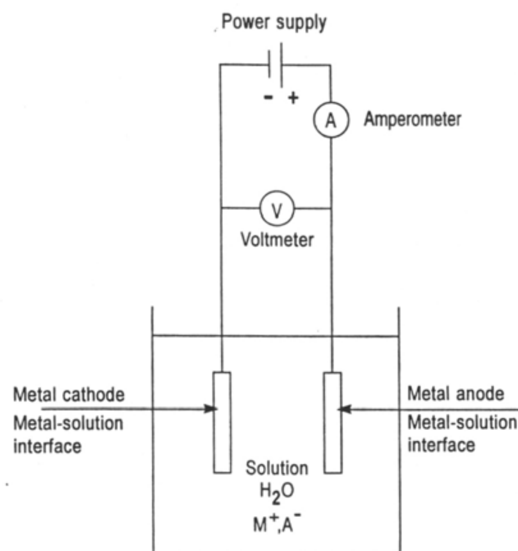

Figure 2.27: Schematic diagram of the electrodeposition process. The bath solution consists of aqueous metal salts as represented by the M^+ and A^-. The object to be plated is the cathode.[74]

Electrodeposition has been in use since around 1800 and has continually evolved and now has countless industrial applications from metal finishing and decoration to metal interconnection lines in integrated circuits. But focusing on its usefulness in producing nanowires inside the AAO pores, there are several issues that need to be dealt with in the as-anodized Al samples before that becomes possible.

2.4.1 Preparing the pores for electrodeposition

The first step in producing nanowires is to prepare an electrical connection to the ordered pore array. After anodization, there is a thin insulating barrier layer that is present beneath the pores so that no electrical connection exists between the Al substrate and the pore base. For uniform electrodeposition it is desired that the pores reach through to the substrate and a clear electrical pathway exists between the

substrate, the pores, and the electrodeposition bath. Small variations in the barrier layer thickness will result in current fluctuations during electrodeposition and will likely result in inhomogeneous filling of the pores.[75] Making this electrical connection to the substrate can be accomplished in several ways. A process of thinning the barrier layer was developed in 2000 by Gösele et al. in which the anodization voltage is reduced in a step-wise manner, after an etching treatment that both widens the pores and thins the barrier layer.[76] Two anodization steps at constant current densities of 290 and 135 mA / cm^2 were conducted which limited the formation rate of the oxide and decreased the barrier layer thickness to less than 10 nm.[76] This also results in branching of the pores as the smaller anodization voltages promote the nucleation of multiple pores in each of the larger already established pores.[37] The same authors later improved this procedure by using two different anodization solutions, a phosphoric acid solution with voltages from 195 V down to 80 V, decreased by 2 V increments every three minutes, followed by oxalic acid from 80 V down to 1 V reducing the voltage exponentially every 30 seconds.[77] This method does result in the creation of large pores of 180 nm on top with branches at the pore bottom of 40 nm in diameter and is difficult to apply to smaller pores without broadening them.[77]

Alternatively, if a very thick porous layer is desired, a stand-alone AAO film may be sufficient. In this situation, a thick porous film is created during a long time anodization and the remaining Al substrate is dissolved, leaving a free standing porous layer. Next, the backside of the porous layer is etched in an acid solution to remove the barrier layer and create through-hole pores. To create an electrical contact for electrodeposition an inert metal film, such as Pt, is sputtered onto the backside of the

AAO template.[78] This allows for easy electrodeposition into the pores and no barrier layer problems, but it is limited to very thick porous films which may not be very mechanically robust, in addition, the lack of a substrate also limits potential applications.

For AAO on Si substrates, the barrier layer thinning techniques are not relevant. If the barrier layer is thinned to the point where contact with the Si substrate occurs, the electrolyte and anodization voltage will result in the formation of an insulating layer of silicon dioxide (SiO_2).[51] Even though the doped Si is conductive, the SiO_2 that forms prevents a good electrical connection. The solution to this is to deposit a thin metal film between the Si substrate and the aluminum layer to serve as a conducting electrode. This was demonstrated in 2003 by Rabin et al.[79] They reported using a platinum film on top of a titanium adhesion layer on a Si substrate. With the Pt/Ti films the anodization characteristics were different than a Si substrate without a metal underlayer. As the Al layer was consumed and the Pt layer became exposed to the electrolyte the current began to increase rapidly and evolution of gas bubbles occurred from the electrolysis of the acid on the Pt.[79] Anodization had to be stopped at this point in order to prevent the AAO layer from detaching from the substrate.[79] After anodization, an electrical connection was present and bismuth nanowires were deposited, although the presence of a partial barrier layer limited the deposition uniformity.[79] To prevent the evolution of gas bubbles after the Al layer is consumed, a Ti underlayer can be used instead of the Pt layer. By continuing anodization after the Al is consumed the barrier layer can be thinned and the Ti layer becomes partially anodized without such a vigorous release of gas bubbles that might detach the AAO layer. The thin barrier layer

can then be removed by anodizing the sample in a dilute potassium chloride (KCl) solution at a low anodizing voltage of around 2 V.[79] It was later discovered in 2005 by Tian et al. that it is possible to dissolve the barrier layer in-situ in the anodizing solution by reversing the anodization bias, connecting the Al film to the negative terminal of the power supply, and applying low voltages of 3.5 – 5 V.[80] This creates voids in the Ti layer and yet still maintains conductivity, allowing the deposition of the nanowires. Figure 2.28 shows an SEM image of the deposited nanowires and their interface with the substrate.[80]

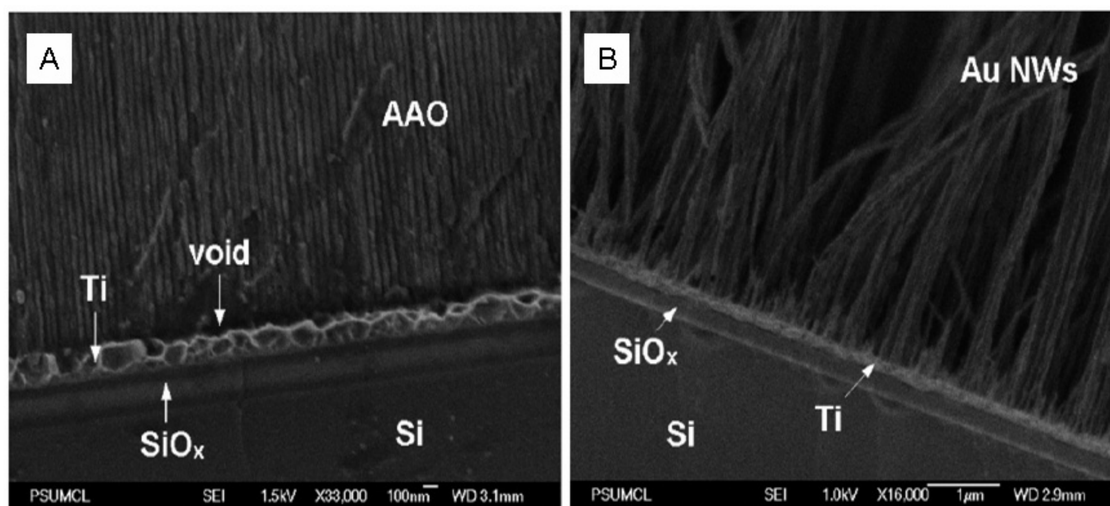

Figure 2.28: SEM images showing the interface between the Si substrate, Ti buffer layer, and the Au nanowires, (A) after anodization showing the pores and (B) after electrodeposition and removal of the AAO layer to show the nanowires.[80]

There have been other reports in the literature concurring with the effectiveness of this technique.[81] It is also possible under some conditions to deposit nanowires without removing the barrier layer. This has been reported using an alternating current electrodeposition method at 50 - 200 Hz and varying voltages, for Ni, Co, and Fe

nanowires.[82, 83, 84, 85, 86] The vast majority of published research in the field uses a dc electrodeposition process, presumably because it provides advantages in control and uniformity of the deposit.

2.4.2 Elemental and alloy nanowires:

The nanowires that are deposited into the pores take the shape of the pores and the result is a straight and vertically aligned nanowire that grows perpendicular to the substrate. Figure 2.29 shows an SEM cross-sectional image of silver nanowires inside the pores of an AAO film.

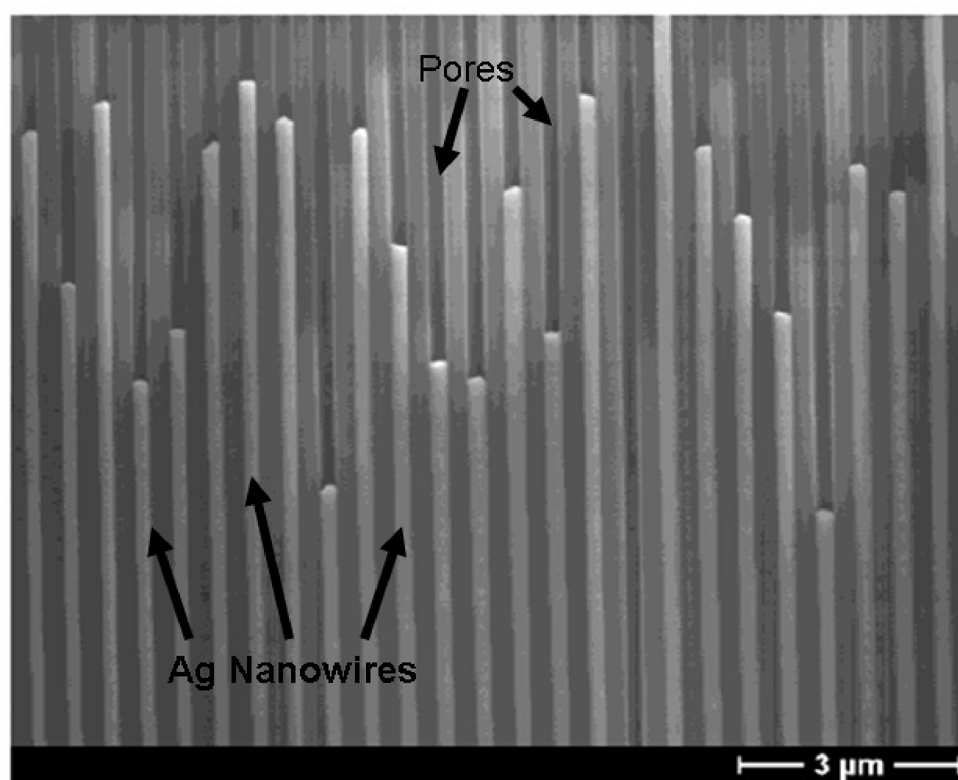

Figure 2.29: SEM cross-sectional image of silver nanowires, appearing as the bright vertical stripes, grown inside the pores of an AAO film.[77]

It can be observed from the figure that the height of the nanowires is not very uniform. Better height uniformity than that shown in Figure 2.29 has been reported in other publications but there is still some variation in the height of the nanowires, perhaps due to differences in the conductivity at the pore bottom from remnants of the barrier layer.[87]

Due to the versatility of electrodeposition it is possible to also deposit alloy nanowires in addition to elemental nanowires. This is done by preparing an appropriate bath solution containing aqueous metal ions of both elements that will be deposited. The composition of the deposit is influenced by the relative concentration of each element, the current density and voltage, bath pH, and bath temperature.[73]

There have been reports of many different types of nanowires that have been fabricated in AAO templates for different applications. Many of those reports concern magnetic nanowires because of the potential of anodized aluminum oxide templates for applications in patterned magnetic recording media. Other than magnetic nanowires there have been reports of other types of nanowires as well. Photoluminescence properties in In_2O_3 and CdS nanowires have been studied by several researchers.[88, 89, 90, 91] There have also been reports of Pd nanowires for potential hydrogen sensors and Bi_2Te_3 nanowires for thermoelectric applications.[87, 92]

While a detailed account on the use of AAO templates for magnetic recording applications will be given in section 2.5.3, a brief background on some of the magnetic nanowires that have been studied to date will be given here. The magnetic nanowires that are deposited in the pores usually exhibit shape anisotropy, and in some cases crystalline anisotropy, which allow for very advantageous properties such as a larger

coercivity along the nanowire axis. There have been several reports on the magnetic properties of Ni nanowires and it has been shown that as the nanowire diameter decreases in the range from 55 – 30 nm the coercivity increases from 600 Oe to 1200 Oe along the nanowire axis and the M-H loop squareness improves from 30% to 98%.[93, 94] The M-H loop graphs are shown below in Figure 2.30, illustrating the influence that the aspect ratio of the nanowire has on its coercivity.

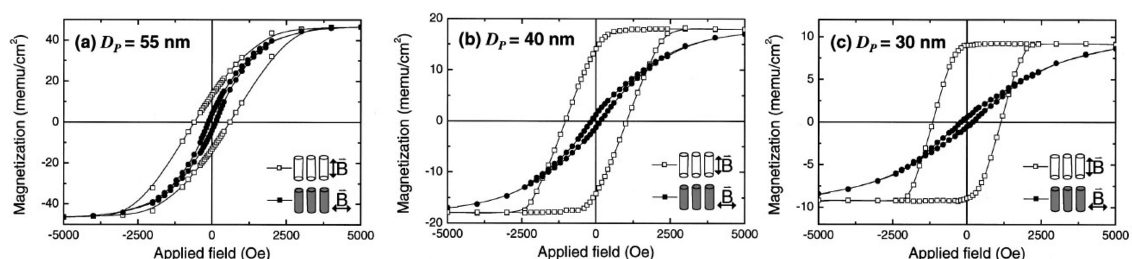

Figure 2.30: M-H loops showing the variation in the coercivity as measured parallel to the nanowire axis (□) and perpendicular to the nanowire axis (●) for nanowires with diameters of (A) 55 nm, (B) 40 nm, and (C) 30 nm.[94]

Magnetic data has also been collected for Fe and Co nanowires showing coercivities along the nanowire axis of 2.2 kOe and 2.3 kOe, respectively.[83, 86] There have also been many studies of different binary magnetic alloys nanowires, including FeCo, $Co_{67}Ni_{33}$, $Co_{48}Pb_{52}$, $Fe_{60}Pb_{40}$, and $FePt_3$, with diameters of 20 nm – 200 nm and coercivities ranging up to 2.9 kOe in the perpendicular direction along the nanowire axis.[95, 96, 97, 98, 99]

In terms of previous work in the field concerning CoPt nanowires, one of the topics of this research, there have been an increasing number of reports in the last few years on their fabrication and magnetic properties. In their ordered face-centered

tetragonal $L1_0$ phase CoPt alloys show strong magnetocrystalline anisotropy; reports have shown that CoPt alloy thin films are capable of generating a coercive force of around 10 kOe after a heat treatment to convert the as-deposited material to the ordered $L1_0$ phase.[100] Due to this desirable property and their ability to be electrodeposited, CoPt, and also FePt, a very similar binary system, have received considerable attention as possible materials for patterned magnetic recording media, which will be covered in further detail in section 2.5.3. Figure 2.31 shows the phase diagram of the CoPt system and the crystal structure of the ordered face centered tetragonal (fct) $L1_0$ phase.

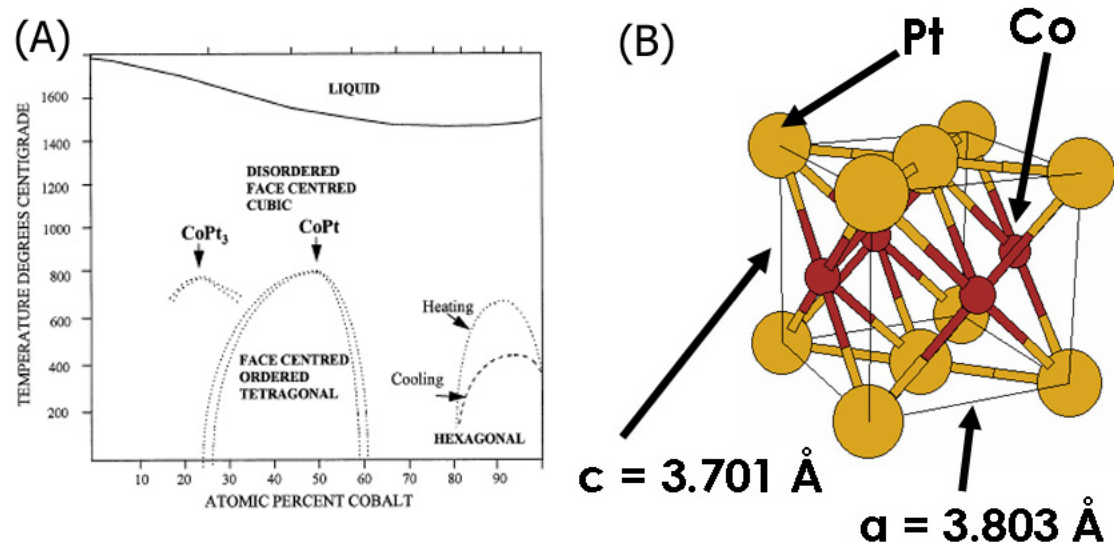

Figure 2.31: The phase diagram of the CoPt system showing the composition range of the ordered face centered tetragonal $L1_0$ phase (A) and the crystal structure of the $L1_0$ phase (B).[101, 102]

It can be seen from the phase diagram that the ordered $L1_0$ phase exists only over a Co composition of approximately 25 – 57 atomic percent.[101, 102] On either side of this range there exists a face centered cubic (fcc) $CoPt_3$ phase and a hexagonal close packed

(hcp) Co_3Pt phase.[103] The $L1_0$ structure shown in Figure 2.31 (B) exhibits a shortened c-axis due to the presence of the smaller Co atoms. The first report of CoPt nanowires in an AAO template was published in 2003 by Yasui et al. They reported the fabrication of ~80 nm diameter nanowires over a range of compositions, $Co_{17}Pt_{83}$, $Co_{44}Pt_{56}$, $Co_{54}Pt_{46}$, $Co_{80}Pt_{20}$, and $Co_{85}Pt_{15}$, with the $Co_{54}Pt_{46}$ exhibiting the ordered $L1_0$ phase and having a coercivity of 7.4 kOe in the perpendicular direction (along the nanowire axis).[104] Following that report, was a study on the magnetic properties of $Co_{65}Pt_{35}$ with a disordered face centered cubic (fcc) structure with nanowire diameters ranging from 48 – 470 nm.[105] The magnetic data from that study shows the influence of the composition and crystal structure on the coercivity as the highest coercivity reported for that composition was 2.3 kOe.[105] In order to realize the ordered $L1_0$ phase it is necessary to subject the as-deposited CoPt phase to an annealing treatment at temperatures around 700°C because the as-deposited CoPt is generally in the disordered fcc phase.[104, 105] Although, it is possible to create an as-deposited amorphous phase; amorphous $Co_{49}Pt_{51}$ nanowires with a 35 nm diameter were reported, yet only reached a coercivity of 2.7 kOe.[106] Another study of platinum rich CoPt nanowires exhibiting low coercivity further emphasizes the need to attain the right composition and phase in order to reach good magnetic properties.[107]

The first study to report very high coercivity CoPt nanowires was published in 2005 by Mallet et al. They reported the fabrication of 80 nm $Co_{50}Pt_{50}$ and 35 nm $Co_{47}Pt_{53}$ nanowires in AAO templates on Si substrates.[108] Both nanowire structures exhibited the ordered $L1_0$ phase after an annealing treatment at 700°C.[108] The 80 nm nanowires had a coercivity of 10.87 kOe while the 35 nm nanowires had a coercivity of

7.5 kOe.[108] Figure 2.32 shows the M-H loops for the two different sizes and compositions of the nanowires that they were able to obtain.

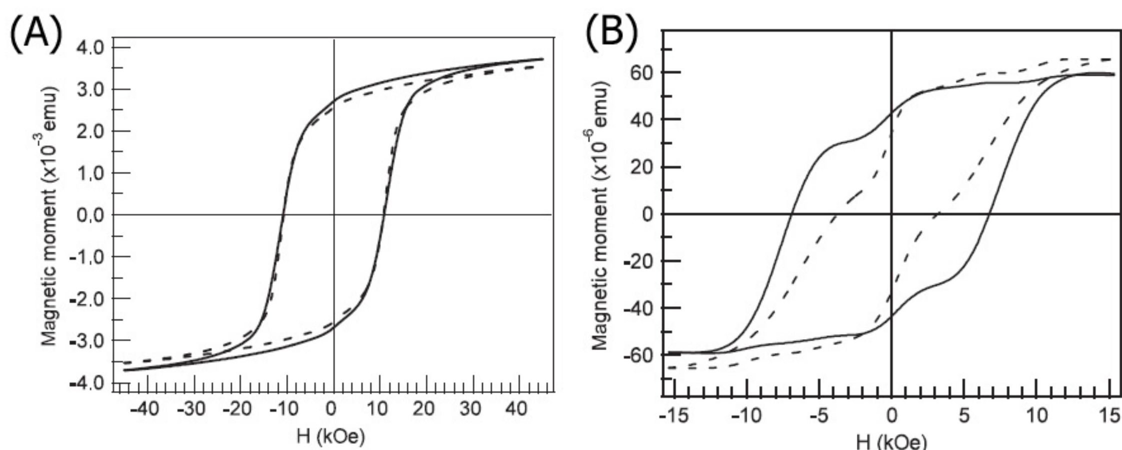

Figure 2.32: M-H loops for CoPt nanowires measured with the applied magnetic field parallel to the wire axis (—) and perpendicular to the wire axis (- - -) for the 80 nm $Co_{50}Pt_{50}$ nanowires (A) and the 35 nm $Co_{47}Pt_{53}$ nanowires (B).[108]

The M-H loop in Figure 2.32 (B) is considerably different from that in Figure 2.32 (A). The shape of the loop in Figure 2.32 (B) indicates the presence of two phases, likely the co-existence of the fcc and fct phases as has been reported in FePt nanoparticles.[109] The authors reported difficulty in controlling the composition of the 35 nm nanowires due to hydrogen evolution during the electrodeposition process and perhaps this may be a reason for the presence of two phases. Since this report there have been a few other reports of CoPt and also FePt nanowires that exhibit coercivities in excess of 10 kOe. In those reports, the nanowire diameters are 60 – 100 nm with a coercivity of up to 11 kOe after a 700°C annealing treatment.[110, 111] The CoPt system seems to be preferred to

the FePt system because Fe is much more chemically active than Co and it seems harder to obtain FePt nanowires with a high coercivity than CoPt.[111]

With all the work that has been done on CoPt nanowires in AAO templates there are some significant shortcomings. First, all of the nanowires studied in the reports mentioned above are significantly longer, with a minimum length of 500 nm, than would be desired for any patterned media applications. Second, the smallest reported nanowire diameter has been around 35 nm, which is too large to form any type of high-density magnetic storage system. Some of the goals of this research have been to address these areas of interest and progress towards this will be presented in Chapter Four.

2.4.3 Multi-layer nanowires

Using electrodeposition it is also possible to create multi-layer nanowires consisting of alternating layers of different elements or alloys. A single bath solution containing multiple species of metal ions can be used because each ionic species has its own unique standard reduction potential.[112] This allows for separate deposition of the different elements or alloys. However, there will still be some co-deposition of elements. This can be minimized by balancing the voltage and varying the concentrations of the elements in the bath.[112] For example, in one report detailing the fabrication of Ni/Cu multi-layer nanowires, at an applied voltage of 0.3 V for 30 seconds Cu was deposited and at an applied voltage of 1.4 V for 10 seconds Ni was deposited.[113] A schematic diagram showing the structure that was formed and a TEM

image of a segment of the nanowires confirming their appearance are shown in Figure 2.33 (A) and (B).

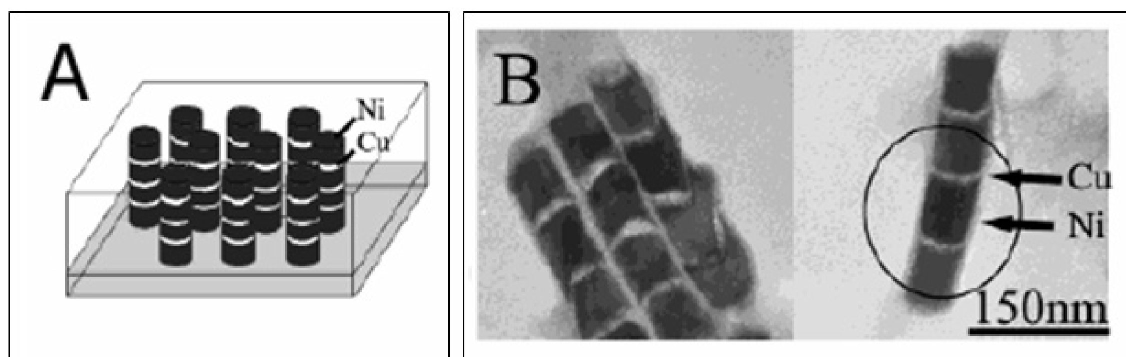

Figure 2.33: A schematic diagram showing the structure of the Ni/Cu multi-layer nanowires (A) and a TEM image of segments of the dispersed nanowires (B).[113]

As the figure shows there are clearly alternating bands of Ni and Cu layers, the authors report an enhanced coercivity of 490 Oe compared to that of 290 Oe for Ni nanowires measured at the same temperature.[113, 114] Compared to the amount of published material on elemental and alloy nanowires there have been comparatively few reports on multi-layered nanowires produced in AAO templates. The following multi-layered nanowires have been reported in the literature: NiFe/Cu, CoNi/Cu, Co/Cu, and CoPt/Pt.[115, 116, 117, 118] The magnetic properties of each of these nanowire systems were studied with all exhibiting coercivities of less than 2.5 kOe. While there have been these few limited reports on multi-layer nanowires, there have not been any reports of two layer nanowires or their magnetic properties. Additionally, the reports mentioned above have all detailed the fabrication of long nanowires; there have been no reports of shorter nanowires. The fabrication and magnetic properties of a short two layer Ni/CoPt

nanowire system has been accomplished as part of this research work and will be discussed in section 4.3.2.

2.5 Applications of anodized aluminum oxide membranes

Because of its advantageous properties, anodized aluminum oxide has widespread and diverse applications. Its versatility is demonstrated by applications ranging from traditional industries such as architecture and transportation to the emerging nanotechnology markets and possible use in future magnetic recording technology.

2.5.1 Structural and architectural applications

Due to their unique nature, anodized aluminum coatings are widely used in structural and architectural applications. The oxide coating that forms on the surface offers good wear resistance and protection from corrosion. In addition, there are a variety of different surface finishes and textures that can be created using different anodization conditions. It is also possible to attain many different colors either by anodizing aluminum alloys such as Al-Si or Al-Cr, or through post-anodization treatments like soaking in organic dyes or electrodepositing inorganic materials at the pore bases.[18] With all these available finishing options, anodized aluminum coatings are used extensively in architectural applications as decorative and protective coatings on exterior building components such as doors, window frames, hand rails, and ceiling panels.[119] They are also prevalent in the transportation industry as decorative trim in

automobiles, planes, and trains.[119] Many consumer electronic devices also use anodized aluminum coatings to provide smooth and shiny durable surfaces.

2.5.2 Sensors and other nanotechnology applications

The small sizes of the pores in the anodized aluminum films also lend themselves to many applications in the advancing field of nanotechnology. The porous films naturally can be used as membranes, with one application as electrolyte carriers and separators in lithium ion rechargeable batteries.[120] The electrical properties of porous alumina are very sensitive to moisture which gives the material much promise for use as a humidity sensor. Micro-humidity sensors responding within the range of 50 – 100 ppm have been tested and are functional and reproducible.[121] There are also potential applications as a dielectric material, with a dielectric constant of 2.4 being attained, a breakdown voltage of 400 V, and a very low leakage current below 10^{-9} A / cm^2 at 15 V.[122] Studies on overheating in interconnects has shown this structure to have advantages over aluminum interconnects passivated by silica insulators.[123]

2.5.3 Magnetic recording media

In a fashion similar to Moore's Law, which has been followed by the semiconductor industry, the storage capacity of hard disk drives has continued to increase over the past several decades. Continued technological advances have helped to perpetuate this trend. At the same time, the price per gigabyte of storage space has drastically decreased. This combination of increased storage capacity and a decrease in the price leads to a very demanding environment in the magnetic storage industry.

There is strong motivation to perpetuate this trend of increasing storage capacity while keeping prices low. Additionally, the industry is facing competition in some areas by other storage technologies such as the rapidly growing flash memory storage, in widespread use in digital cameras, MP3 players, and USB drives. Unfortunately, magnetic storage methods utilizing the current technology based on thin films of magnetic material are reaching the fundamental physical limits on their capacity and have little room for further expansion. It is therefore necessary to develop new storage methods to perpetuate the growth in areal storage density, while also keeping the price per gigabyte of storage at an economical level. Figure 2.34 (A) shows the increase in storage capacity over the last several decades and some of the technological advancements that made this possible.[124] Figure 2.34 (B) shows the drop in price per gigabyte of storage space in recent years.[124]

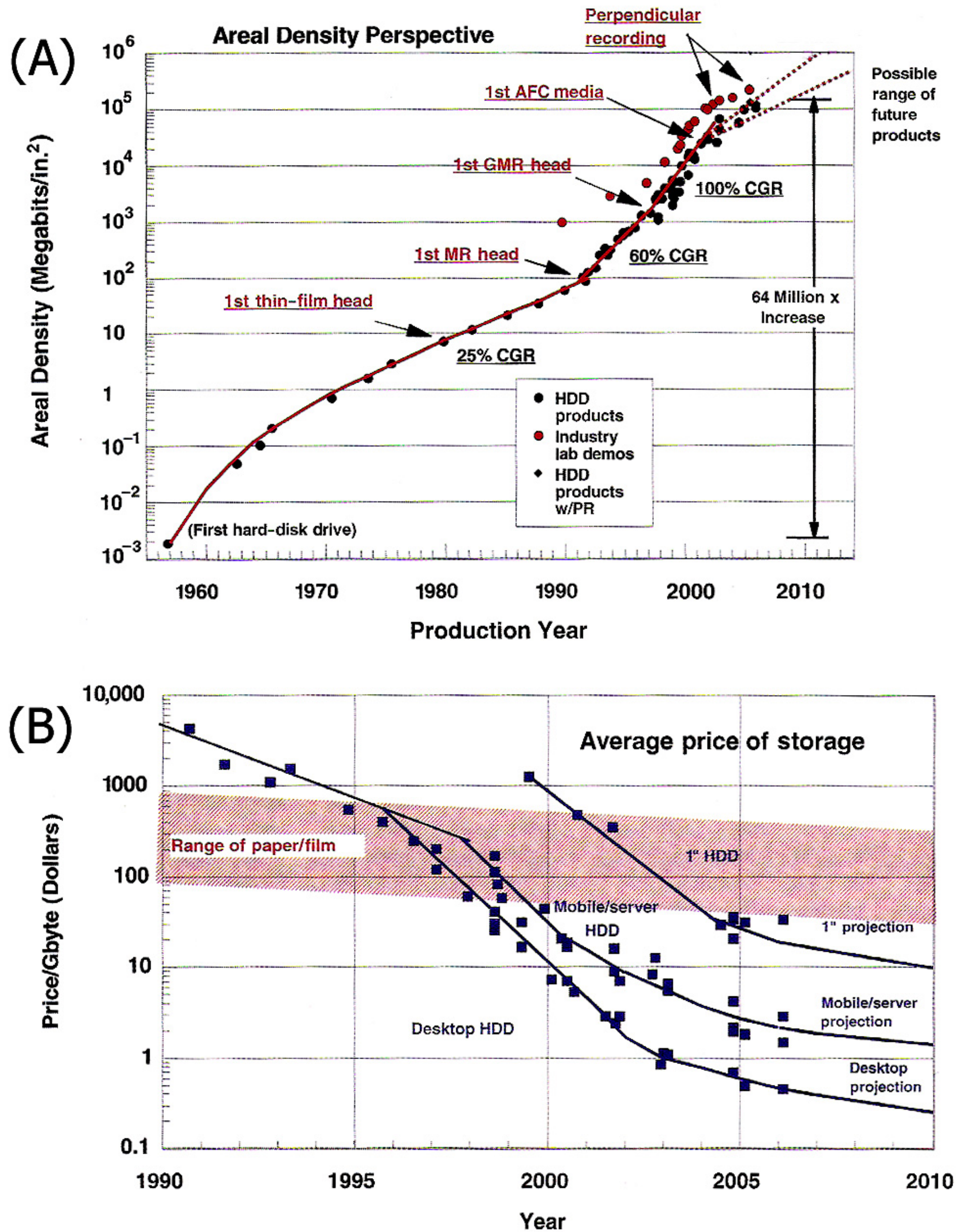

Figure 2.34: (A) The increase in areal storage density is shown along with the compound growth rate (CGR), the introduction of the first magnetoresistance (MR) recording head, the first giant magnetoresistance (GMR) head, and antiferromagnetically coupled (AFC) media. (B) The decrease in average price per gigabyte of storage is shown since 1990 for different types of storage, including projections through 2010.[124]

As the figure shows, there were large increases in the growth rate of storage capacity with the innovation of MR and GMR recording heads which were much more sensitive and provided increased signal-to-noise ratios when reading and writing data.[125] With each of these came changes in the thin films used to store the data. The MR heads utilized Co alloy films such as CoCrTa and CoCrPt while the GMR heads relied on CoCrPtTa and CoCrPtB quaternary alloys.[125] Along with more complicated magnetic layers there are also several underlayers that are present in order to control the grain size and epitaxy as well as increase the signal-to-noise ratio (SNR).[125] Despite these advances there are still looming fundamental physical limits which will prevent further advances to the magnetic thin films and increases in the storage density.

Currently, magnetic recording is a longitudinal system using a group of small grains of the magnetic alloy thin film to store the data at densities up to about 250 Gbits / in^2, where one bit is comprised of approximately 65 grains.[126] A schematic diagram of a longitudinal recording system is shown below in Figure 2.35.[127]

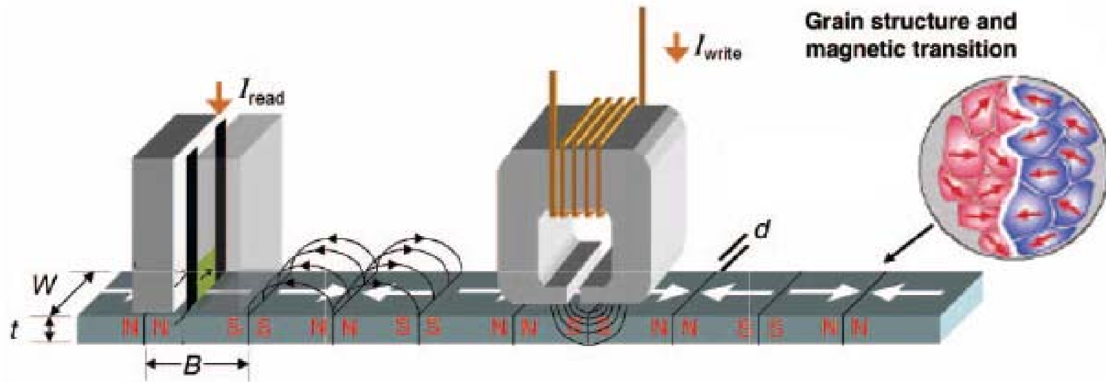

Figure 2.35: Schematic diagram showing the longitudinal magnetic recording system with separate read and write heads, the relevant parameters, and the grain structure with magnetic transitions. Typical values for the parameters are: track width W = 210 nm, thickness of film t = 14 nm, bit length B = 30 nm, distance of heads to surface d = 10 nm.[127]

The inset enlarged figure shows the varying magnetic spin alignments of the grains within each bit and the sharp transition that occurs at the boundary. The overall magnetic spin of the bit is therefore determined by the aggregate of the different spins of each grain that comprises the bit. In recent years, the improvements in recording density have been achieved by reductions in the grain size, bit length, and track width. However, there is a limit to these reductions.

As the grain size decreases there are issues with the thermal stability of the magnetic spin orientation of the grain. When the volume of magnetic material in the grains reaches a certain minimum value the amount of thermal energy present may be large enough to cause unexpected reversal in the magnetic spin orientation.[128] The magnetic energy of a grain can be represented by the product of its magnetic anisotropy (K_u) with the volume of the grain (V), while the thermal energy is equivalent to Boltzmann's constant (k_B) multiplied by the temperature (T). For sufficient thermal

stability over a reasonable timescale of at least 10 years, the following condition should be met:

$$K_U \cdot V > 55 \cdot k_B \cdot T \ ,$$

with the range of reported values being from 55 – 80.[125, 127, 129] From this equation it seems possible to counter decreases in V from shrinking grain size by simply increasing the magnetic anisotropy. The magnetic anisotropy represents the amount of energy required to rotate the magnetization perpendicular to the easy axis, or the energetically more favorable direction for magnetization.[129] There can be multiple contributions to the overall anisotropy, notably the magnetocrystalline anisotropy based on the crystal structure, shape anisotropy due to the dimensions, and magnetoelastic anisotropy arising from interactions between strain and magnetization, such as at interfaces.[129] Increasing the anisotropy does result in more thermally stable grains, however, practically this is limited by the available write head fields capable of switching such high coercivity materials. A material's coercivity can be approximately represented by the following equation:[127]

$$H_C \cong \frac{K_U}{M_S} \quad .$$

There may also be negative effects on the SNR from decreasing grain size and volume. This combination of thermal instability, write field limitations, and SNR needs are known as the superparamagnetic limit.[128, 130]

One potential solution of keeping the grain volume high is to move to a perpendicular recording technology rather than a longitudinal one. For perpendicular recording media the north – south magnetic spin orientation is vertical rather than

horizontal, with a larger thickness of the magnetic layer there is larger grain volume for a given track width. Figure 2.36 shows the difference between longitudinal and perpendicular recording technology.[131]

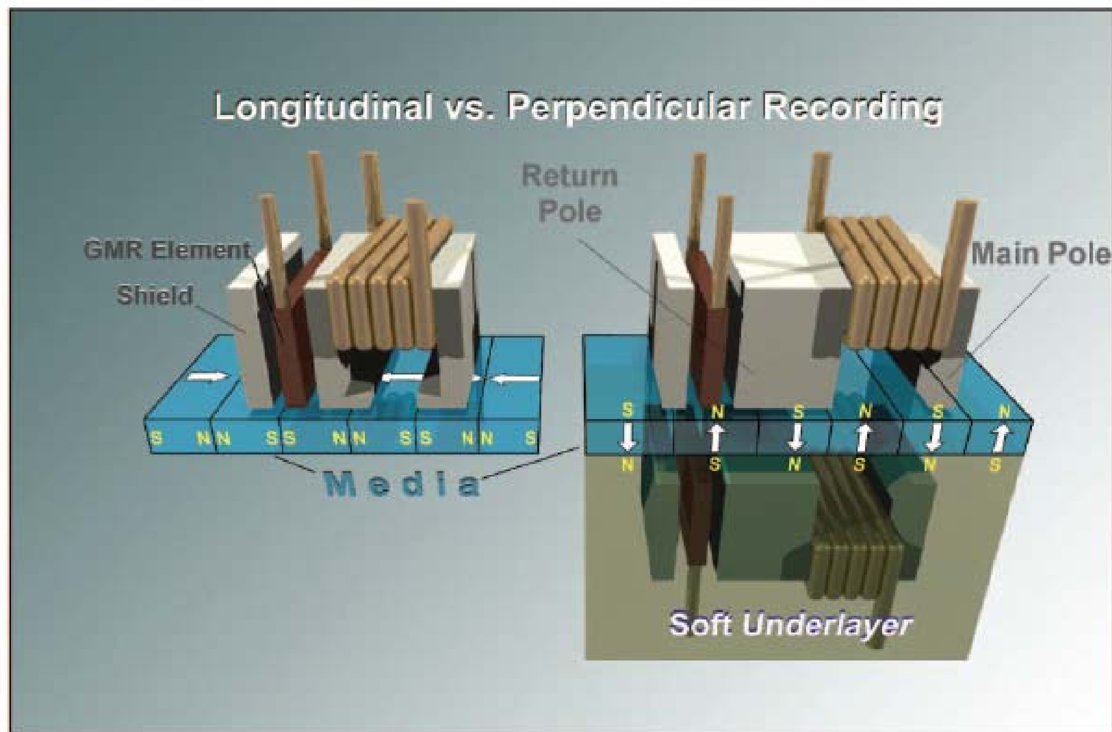

Figure 2.36: Schematic diagram showing the differences between longitudinal (left) and perpendicular (right) recording technologies.[131]

As the grain are packed close together in perpendicular magnetic recording (PMR) it is necessary to segregate the grains from one another to reduce noise.[132] This, along with the perpendicular spin orientation, requires good epitaxial control in the magnetic layer which can only be obtained through the use of an appropriate seed layer.[131] Figures 2.37 (A) and (B) show a typical PMR film structure from the top and cross sectional views.

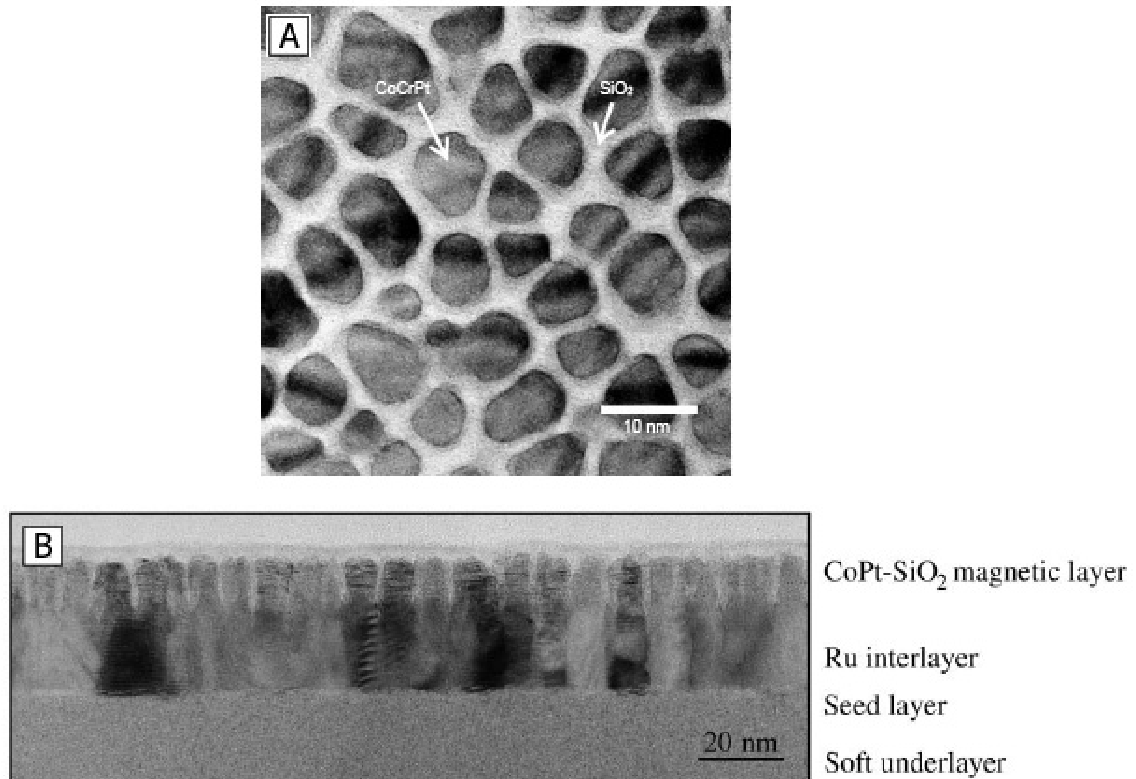

Figure 2.37: Transmission electron microscope images of the top view of the magnetic CoCrPt-SiO_2 layer showing the grain segregation (A) and the cross section showing the columnar grain structure and sequence of underlayers (B).[131, 132]

A thicker magnetic layer of 15 – 20 nm leads to a larger grain volume, enhancing the thermal stability in the small grains. The seed layer and the Ru layer act to maintain a narrow grain size distribution and control the c-axis orientation of the magnetic layer.[131] Which also limits the size of the transition region between neighboring bits.[131] It has been estimated that even with further advancements the limitations inherent in perpendicular recording will limit its recording density to between 500 Gbits / in^2 – 1 Tbit / in^2.[124, 133, 134, 135, 136] With these limitations in mind, it is necessary to think towards the future of magnetic recording despite the fact that PMR hard disk drives

have only recently been released in stores within the last two years. Patterned magnetic recording media has recently received a considerable amount of attention as a potential successor to PMR in the magnetic recording industry.

Patterned magnetic recording media has several advantages over longitudinal and perpendicular recording methods. In patterned media, each magnetic element stores one bit of data and the elements are separated and isolated from one another. This keeps each element thermally stable even at sizes below 10 nm because the entire volume of the element contributes to the signal and the transitions between bits are defined by the patterning.[137] In the case of longitudinal and perpendicular recording media, each a bit is made up of multiple grains and there is averaging taking place to obtain a higher SNR with the bit transitions determined by the magnetic field from the recording head.[137] The primary advantage in patterned media is that the bits can be placed very close together making it capable of achieving very large recording densities. Figure 2.38 shows the corresponding areal density as it is influenced by the bit diameter and the period or bit spacing.

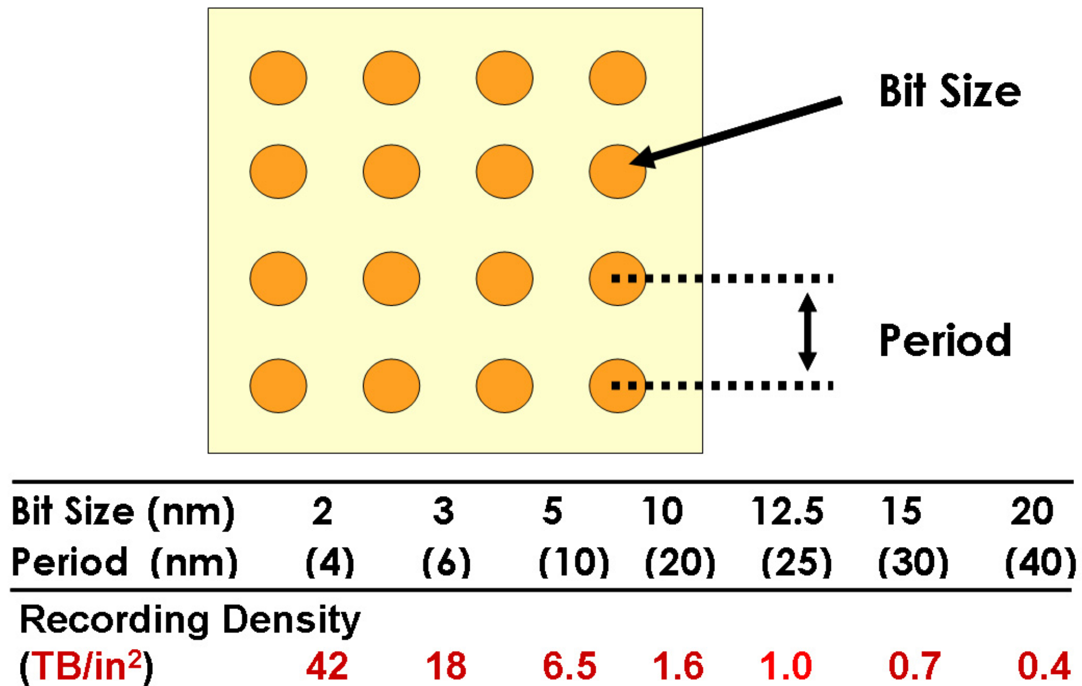

Bit Size (nm) Period (nm)	2 (4)	3 (6)	5 (10)	10 (20)	12.5 (25)	15 (30)	20 (40)
Recording Density (TB/in^2)	42	18	6.5	1.6	1.0	0.7	0.4

Figure 2.38: Schematic diagram illustrating a patterned recording media and showing the influence that bit diameter and bit spacing have on the corresponding recording density.

The figure shows that a bit diameter of 12.5 nm and a period of 25 nm would correspond to an areal density of 1 Tbit / in^2. As the bit diameter and period shrink, the magnetic fields of neighboring bits may influence each other and a shorter bit element will be necessary as it will exert a lesser field on the neighboring elements.[137] When bit sizes decrease beyond this point it will ultimately be necessary to place a soft magnetic underlayer (SUL) beneath the patterned media bit elements. The SUL acts to channel the magnetic flux from the write head. In a sense, it places the patterned media between two magnetic fields, that of the write head and that channeled through the SUL, effectively increasing the write head field and allowing the use of higher anisotropy materials to compensate for decreases in bit size and volume.[137] It is clear that there is

much promise in patterned recording media. There are also many challenges involved in successfully fabricating a functional patterned recording media.

One the primary challenges is to come up with an ordered array of elements with such small diameter, on the scale of 10 – 20 nm, with small periods of 20 – 40 nm. The preceding sections of this chapter detail the properties and self-organizing capabilities of anodized aluminum oxide demonstrating its potential to serve as a suitable template for patterned recording media. The other challenge is the placement and quality of a suitable magnetic layer that meets the requirements in terms of magnetic properties and physical dimensions. It was also previously shown that electrodeposition of materials such as CoPt into the anodized aluminum oxide templates is potentially an attractive solution to this problem. While there are still many issues to be dealt with before a functional patterned media can be realized, hopefully further work and some of the accomplishments of this research, discussed in Chapter 4, will help to bring about the realization of this goal.

CHAPTER 3: EXPERIMENTAL PROCEDURES

3.1 Thin film deposition:

The substrate materials for anodization were prepared by depositing metal thin films onto the surface of 100 mm n-type (100) Si substrates. DC sputtering in a Denton Discovery 18 was used to deposit all the thin films used in these experiments. On the cleaned Si substrates, a 20 Å thick Ti film is first deposited to serve as an adhesion layer between the Si substrate and the following metal layer. On top of the Ti layer, a 30 Å layer of Au is deposited. The Au layer is necessary as it serves as a non-reactive underlying electrical connection between the Si substrate and the Al layer. The noble Au layer is inert and unaffected by the caustic anodization and electrodeposition environments. Following deposition of the Au layer, 10 Å of Ni are sputtered to serve as a buffer layer between the Al film and the Au layer. The necessity of this buffer layer will be explained in further detail in section 4.1.1. Finally, the Al layer is sputtered on top of this Ni layer. Typically, a thickness of around 250 nm was deposited, although numerous experiments have been conducted at varying thicknesses. An optimization of the deposition parameters such as temperature and power was conducted to produce the smoothest film possible for the subsequent anodization step. A complete analysis of this optimization is covered in section 4.1.2. A very important aspect of the Al sputtering was the need for long pump down times to achieve very low base pressures, in the range of ~3×10^{-7} torr, in order to prevent oxidation or incorporation of impurities during the extended sputtering times needed to

deposit the 250 nm thicknesses. Following deposition of the Al film, the substrates were ready to be prepared for anodization.

3.2 Sample preparation

After deposition of all the metal layers, the metalized Si substrates were diced into specimen sizes suitable for anodization, usually slightly larger than 1 cm^2. In order to form an electrical connection from the Al surface to the anodization and electrodeposition power supplies, ¼" wide copper tape with conductive adhesive from McMaster-Carr was utilized. The copper tape was doubled back on itself to form an electrical lead between the Al surface and the backside of the Si substrate that could be connected to the power supplies. After forming the electrical connection, the sample edges and the electrical lead need to be insulated from the anodization and electrodeposition solutions. An exposed portion of the electrical lead in the anodizing or electroplating solution would essentially result in a short circuit between the anode and cathode. The sample edges need to be insulated to promote uniform anodization and electrodeposition as exposing the underlying metal layers at the edges would result in a non-uniform current and preferential anodization and electrodeposition. To insulate the samples, a lacquer specially designed for electrochemical applications called MiccroShield, produced by Tobler Division, was utilized. The lacquer was applied to the front side, edges, backside, and copper electrical lead, with care being taken on the front side to leave an exposed Al area of approximately 1 cm^2. As per the application instructions for the MiccroShield, after an initial coat of the lacquer was applied the sample was allowed to dry for about 30 minutes before a second coat of lacquer was

applied. The second coat is needed to completely cover any tiny pinholes that may form in the first coat due to incorporation of air bubbles or from out-gassing. After the second coat was applied the samples were allowed to dry overnight to promote adhesion of the lacquer to the substrate and Al film. For clarity, the finished product is shown below in a photograph in Figure 3.1.

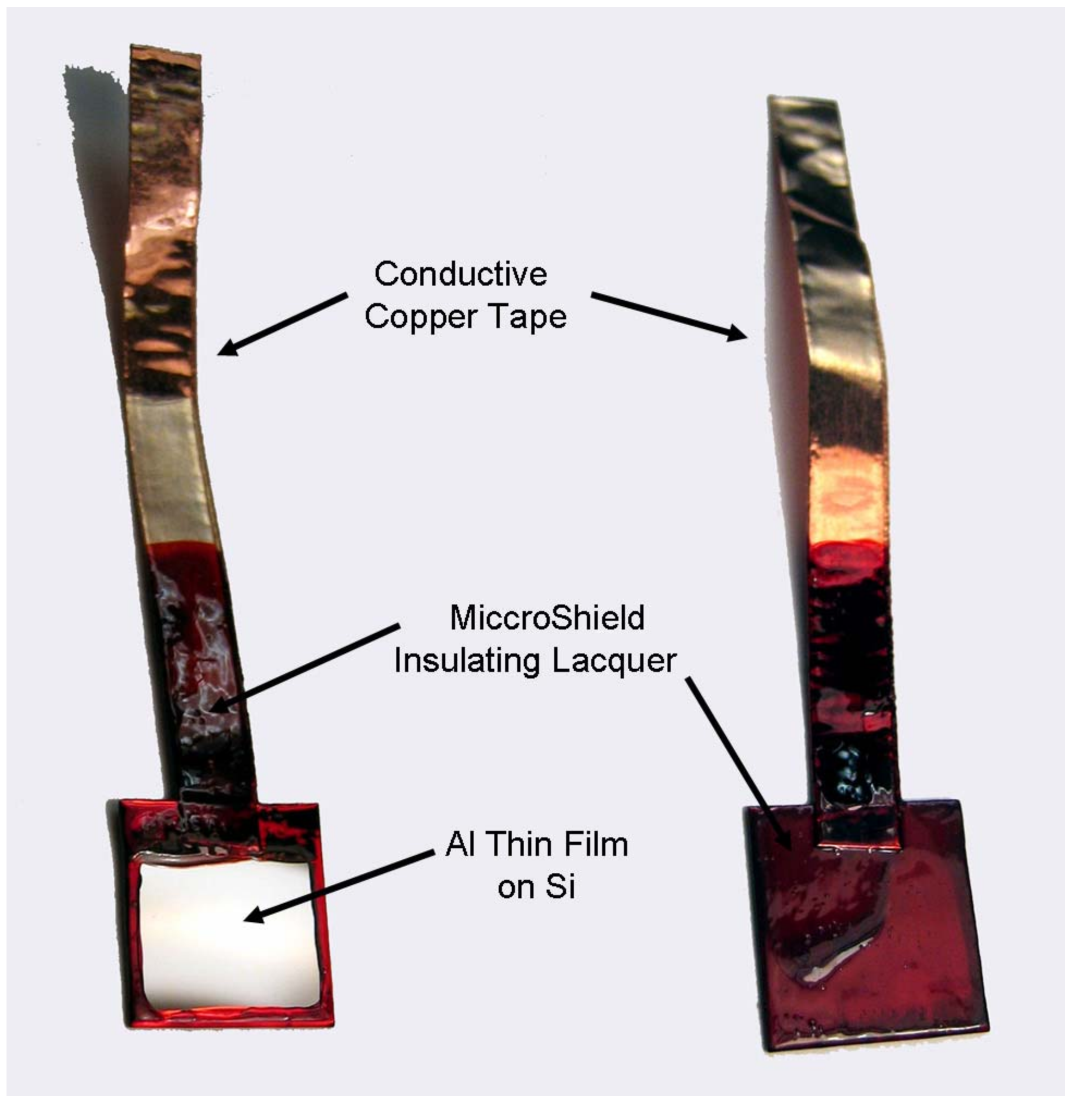

Figure 3.1: Photograph illustrating a prepared sample with an electrical connection and insulated with lacquer.

3.3 Anodization

The anodization process was carried out in an electrolyte solution consisting of 0.3 M oxalic acid ($C_2H_2O_4$). Throughout the anodization process the electrolyte was kept at a constant temperature of 5°C using a Thermo Neslab RTE 7 recirculating chiller and a double walled glass beaker. A piece of platinum foil was used as the cathode material. The platinum foil and the Al sample were each held in a fabricated Teflon chuck designed to maintain a constant separation distance between the two electrodes and facilitate easier electrical connection. A dc power source was used with an applied voltage of 15 – 40 V. A schematic diagram of the anodization setup appears below in Figure 3.2.

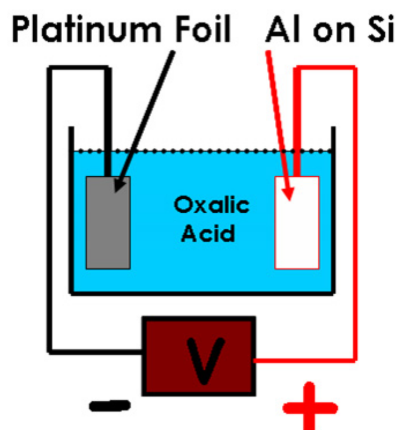

Figure 3.2: Schematic diagram showing the anodization setup used in these experiments.

The anodization was carried out at a constant voltage until a current density of approximately 250 mA / cm^2 was reached. On average this would take about 17 minutes at a temperature of 5°C, with the current remaining at a value of zero until

several minutes into the anodization upon which it begins to rise at a faster and faster rate, rapidly approaching the desired value of 250 mA. A detailed explanation of the current-voltage characteristics of the anodization process will be given in section 4.2.

The two-step anodization process as described previously in section 2.3.1 differs slightly from the single step procedure described above. In this case, the first anodization step was conducted for approximately 8-9 minutes and this initial anodized layer was then removed by immersing the sample for a few minutes in a mixture of 6 wt % phosphoric acid (H_3PO_4) and 1.8 wt % chromic acid (H_2CrO_4) at 60°C. After removal of the anodized aluminum, the second anodization was carried through to completion as described above for the single step anodization. Typically, this results in a porous layer approximately 100 nm thick; however, there is considerable danger of beginning the second anodization step with an Al layer thinner than ~80 nm which seems to be around the minimum necessary to achieve a porous structure.

Following the anodization step, the sample was rinsed off in deionized water and immersed into a 5 wt. % solution of phosphoric acid (H_3PO_4) for 15 minutes to remove any remaining barrier layer present at the bottom of the pores. It is critical to remove this barrier layer and expose the underlying Ni and Au layers because small changes in resistance due to the barrier layer will impact the uniformity of the electrodeposition. However, this step does result in a slight widening of the pores. After this step the sample is soaked in deionized water to remove any remaining acid salts and to clean the sample prior to electrodeposition.

3.4 Electrodeposition

Following etching and exposure of the metal underlayer as a conduction path for electrodeposition, the pores were ready for filling with magnetic material. The electrodeposition process was conducted using a Dynatronix DuP10 pulse DC power supply capable of supplying up to 10 V and 0.3 A, with selectable options for varying the time and duration of the DC pulses. There have been many reports in the literature that using a pulsed power supply can greatly increase the efficiency of the deposition process and the quality of the deposit.[138, 139] For these experiments a constant current density was used with a forward current on time of 0.5 ms and a forward current off time of 0.5 ms. As in the anodization process, a platinum foil was used as the counter-electrode, but for electrodeposition it serves as the anode. Different current density settings were used based on the metal being deposited in the pores.

The Ni sections of the nanowires were deposited using an electrolyte bath consisting of 0.065 M boric acid (H_3BO_3) and 0.045 M nickel sulfate hexahydrate ($NiSO_4{\cdot}7H_2O$).[93] To ensure a slower rate of deposition a current density of 0.1 mA was used with a time of about one minute needed to deposit about 100 nm. With a single element electrolyte bath the current density and voltage serve only to influence the speed and quality of the deposition. On the other hand, when electroplating alloys, the current density and voltage can also influence the composition of the alloy by selectively affecting the deposition rates of one element versus another. The CoPt nanowires were deposited using a previously published bath composition consisting of 0.01 M cobalt sulfate ($CoSO_4$), 0.01 M diamminedinitritoplatinum ($Pt(NO_2)_2(NH3)_2$), 0.085 M sodium acetate ($NaCH_3COO$), 0.052 M triethanolamine ($N(CH_2\text{-}CH_2\text{-}OH)_3$)

and 0.094 M sodium carbonate (Na_2CO_3), with a pH adjusted to 6.3 with sulfuric acid.[108] The ideal current density found to yield the desired atomic ratio of ~50% Co and ~ 50% Pt was determined through experiments to be 23 mA / cm^2. Further information regarding this experimental analysis appears in section 4.3.1.

3.5 Annealing

After electrodeposition of the desired nanowires the samples need to be cleaned before undergoing the annealing procedure. To remove any impurities or leftover solution from the electrolyte baths the samples were first rinsed in deionized water. In order to dehydrate the samples and prevent any oxidation from occurring during the high temperature annealing the samples were subjected to several dehydration steps in increasing concentrations of ethanol (C_2H_5OH) and water solutions. The samples were soaked for ten minutes each in solutions consisting of 10%, 20%, 30%, 50%, 70%, 90%, and in three sequential solutions of 100% ethanol. Following this dehydration procedure the samples were dried using a critical point drier, from Electron Microscopy Sciences, model EMS 850, to remove any remaining traces of water. The cleaned samples were then ready for the annealing treatment.

For annealing, an Applied Test Systems 2" tube furnace with dual zone programmable heater control was used. Prior to use, the controllers were calibrated using thermocouple measurements at various temperature settings. The furnace was outfitted with mass flow controllers, a mechanical pump, and a pressure regulator in order to control the annealing atmosphere. Before operating the furnace, the samples were loaded into the quartz tube in an alumina boat and the tube chamber was pumped

down using the mechanical pump attached to the chamber. After pumping for 10-15 minutes, the chamber was filled with hydrogen and then pumped down again. This process was repeated once more before a final hydrogen fill was conducted. The hydrogen was filled to a pressure slightly above atmospheric pressure to maintain a positive pressure and prevent any of the outside atmosphere from finding its way into the system. A hydrogen atmosphere was selected for all of these experiments to prevent any oxidation of the samples during their exposure to high temperatures.

The heating cycle of the furnace controllers was programmed the following way: 30 minutes heating time to the desired temperature, 30 minute hold time at the desired temperature, and then turning off the heating element for cooling. During the heating cycle, hydrogen gas flowed over the sample at 100 sccm to keep a constant gas flow in the chamber atmosphere. Due to the design of the furnace and its good insulation, the cooling to room temperature was a very slow process. Throughout the cooling process the samples were kept under a hydrogen atmosphere with flowing hydrogen gas to prevent oxidation. A graph of a typical heating and cooling cycle for the furnace is shown below in Figure 3.3 for a 700°C set point.

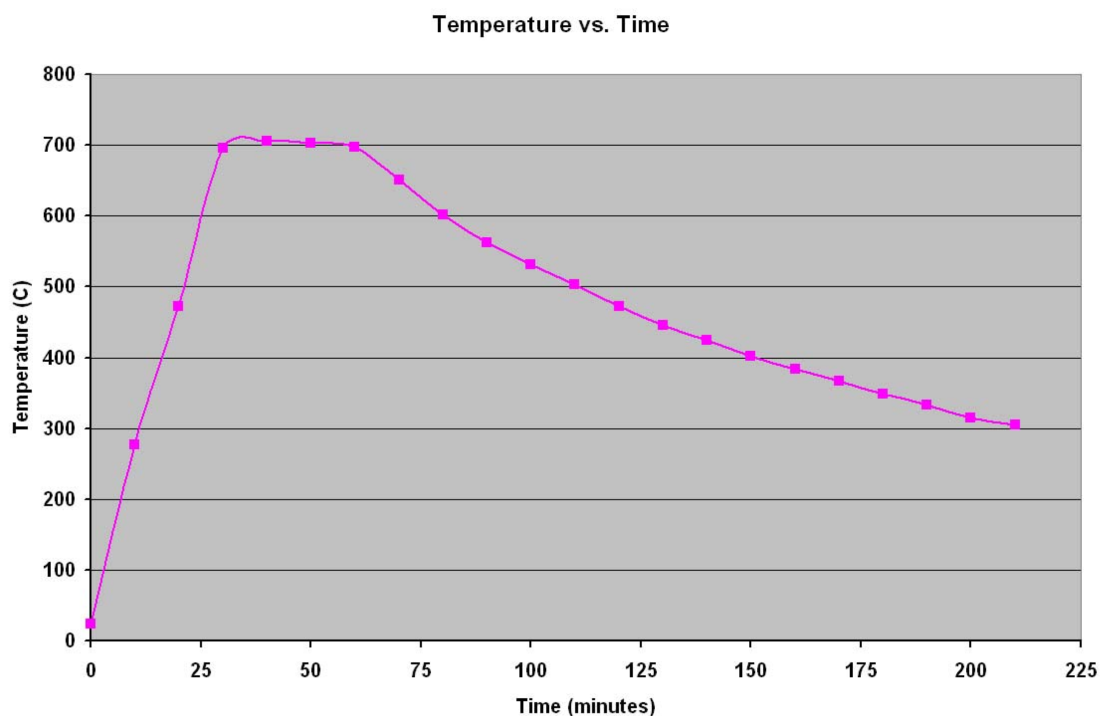

Figure 3.3: A graph showing the heating and cooling cycle for the annealing process, indicated in a temperature versus time plot.

Once the furnace had cooled to room temperature, the chamber was pumped down to vacuum using the mechanical pump and then vented so the samples could be unloaded. After annealing, the samples were ready for characterization by a variety of measurement techniques.

3.6 Sample characterization and analysis

For microstructural analysis of the nanowire samples, scanning electron microscopy (SEM) was performed in a Philips XL30 Field Emission SEM. In order to get a clearer picture of the nanowires, in some instances the AAO template was removed via chemical etching in a sodium hydroxide (NaOH) solution. Cross-sectional

images were obtained by cleaving the samples with a diamond scribe, easily done due to the brittle nature of the AAO and the Si substrates.

The Philips Field Emission SEM was equipped with an Oxford Instruments INCA Energy Dispersive X-ray Spectroscopy (EDS) system. The EDS system was used for compositional analysis of the electrodeposited materials. Using the EDS provided the ability to determine the average composition over a given area. However, the EDS was not sensitive enough to accurately determine the composition of very small regions of nanowires. This is because the penetration depth of the EDS is typically on the order of a few microns while the height of the nanowires in these experiments was only about 100 nm. Considering the volume difference between 100 nm tall nanowires and a few microns of the underlying solid Si substrate there is clearly a comparatively small amount of material that we are interested in measuring.

To measure the surface roughness of the sputtered Al thin films a Veeco Multimode atomic force microscope (AFM) was used. An ultra-sharp AFM tip with a tip radius of a few nanometers was used to obtain a higher surface resolution and therefore more accurate roughness measurements. The AFM analysis software was utilized to determine the RMS surface roughness and comparisons were made at several different scan sizes to determine an average surface roughness. AFM scans were also conducted on anodized aluminum samples to obtain data on the surface roughness and to corroborate the pore size and qualitative surface images obtained with the SEM.

Magnetic measurements of the samples were carried out using an Alternating Gradient Magnetometer (AGM). Due to the very small amounts of magnetic material involved in the measurements, the AGM provided better measurement sensitivity than

the standard vibrating sample magnetometer (VSM). The downside to the AGM used in this analysis was that it is only capable of applying a maximum field of 14 kOe, which turned out to be too low to saturate the high coercivity CoPt materials that were electrodeposited. It would have been ideal to have a maximum applied field of at least 20 kOe, if not higher, in order to observe true saturation of the nanowires. Samples were cut to a size of about 2 mm x 4mm for measurement in the AGM. Measurements were taken in two directions, in-plane with the substrate or perpendicular to the nanowires, and perpendicular to the substrate or parallel to the direction of the nanowires. To see the influence of the annealing treatment, samples were measured before and after annealing. Additionally, the bare aluminum oxide template containing no nanowires was also measured and found to have almost no coercivity.

CHAPTER 4: RESULTS AND DISCUSSION

4.1 Thin film deposition

4.1.1 Metal underlayers

The first step in preparing aluminum thin films for anodization was to deposit the appropriate metal underlayers. Initially, when experiments were first undertaken, the anodization process was conducted without any metal underlayers and utilized just an aluminum film on the silicon substrate. The anodization process was carried out successfully without any metal underlayers and there was good film adhesion between the aluminum film and the substrate. At this beginning stage of the research the samples were also not insulated around the edges and the backside in order to promote more uniform anodization as mentioned in section 3.1. The electrical connection was simply made to the aluminum film and was kept above the level of the electrolyte to prevent shorting.

When we first started research into this field there had been few published reports of nanowires deposited on Si substrates using AAO templates. Consequently, there was little guidance from the literature on the many aspects and details involved in the process. After many failed attempts to electrodeposit materials into the pores, it was discovered that a conductive metal underlayer was necessary because the doped Si did not provide an adequate conduction path. Based on prior research results by Myung et al. on AAO based nanowire arrays on Si substrates for sensor applications we were able to determine a suitable series of metal underlayers.[140, 141] The underlayers consisted of a Ti layer with a thickness of 20 nm, followed by a Au layer with a thickness of 30 nm,

and finally a Ni layer with a thickness of 10 nm. The Ti layer acts as an adhesion layer between the Au layer and the silicon while the Au layer serves as the non-reactive and conductive electrode for the anodization and electrodeposition steps. The Ni layer is present as a buffer layer between the noble Au layer and the Al layer. Without the Ni layer, as the Al layer is consumed during anodization, the Au layer will begin to be exposed to the electrolyte and there will be an evolution of gas bubbles from the electrolysis of the acid electrolyte.[79] In one way, this is good as it indicates that the insulating alumina barrier layer has been penetrated, on the other hand, the rapid evolution of gas bubbles can lead to rupturing and detachment of the AAO film. During anodization, the Ni layer is partially anodized to form a thin conductive oxide layer that serves to connect the AAO film to the Au electrode layer. From the experiments, it appears that the anodized Ni layer has sufficient conductivity for electrodeposition but to ensure uniformity at the pore bottom the samples were still subjected to a post-anodization pore widening treatment in 5 wt % phosphoric acid to remove most, if not all, of the remnants of the Ni layer.

All three of these metal underlayers were deposited sequentially via dc sputtering under continuous vacuum so as to prevent any oxidation of the films when exposed to atmospheric conditions. The films obtained were reasonably uniform over the entire 100 mm Si wafer surface and provided an excellent base surface for deposition of the Al film. Unfortunately, it was necessary for the Al layer to be deposited in a separate sputtering system, as the deposition requirements could not be adequately met with our own sputtering system.

4.1.2 Aluminum film deposition and surface roughness

Prior to attempting to form pore arrays on aluminum thin films, the process was started using bulk aluminum foils. Preparation of AAO on bulk aluminum foils was a good trial and error procedure for learning how to handle the experimental details in the anodization process. It was also educational because, in producing AAO on bulk aluminum foils, we became aware of several steps that must be taken before good quality pore arrays can be achieved on the surface of the foil. The most important step is to create a smooth mirror-like surface through a long and time-consuming mechanical polishing procedure followed in some instances by an electropolishing step. Just as this is important in bulk aluminum it is similarly important for thin film aluminum. Luckily, the sputtering process produces films that are usually about as smooth, if not smoother, than what we achieved through mechanical polishing. This gives us the opportunity to improve this aspect of the experimental procedure and obtain an even smoother surface which helps to produce a more regular array of pores on the surface as was discussed in section 2.3.2.3.

To deposit the thick aluminum layers used for these experiments it was necessary to use a high vacuum deposition environment to prevent oxidation in the deposited film.[142] Our sputtering system lacked the pumping capacity to reach a high vacuum condition. Ideally, it would have been ideal to have had access to an ultra-high vacuum (UHV) sputtering system capable of achieving base pressures of 5×10^{-10} Torr.[143] Unfortunately no such system was available. The aluminum films were deposited at base pressures of at least $\sim 3 \times 10^{-7}$ Torr, which were reached after pumping down the sputtering system for extended periods of time.

With sputtering there are many adjustable parameters that can influence the surface morphology of the deposited film. Some of the most influential parameters are the base pressure, substrate temperature, and deposition power. In attempts to fabricate as smooth a film as possible, experiments were performed varying these parameters in order to determine an optimum deposition condition. Table 4.1 below shows some of the different dc sputtering conditions that were used and the resulting surface roughness, as measured by an atomic force microscope (AFM).

Table 4.1: The corresponding RMS surface roughness values as measured by an AFM for the different sputtering parameters when the substrate temperature and sputtering power were varied.

Substrate Temp. (°C)	Sputtering Power (W)	Al Roughness (nm)	AAO Roughness (nm)
330	150	12.0	13.0
200	150	9.5	10.0
25	150	7.5	8.5
25	125	6.0	6.5
25	***100***	***3.0***	***4.0***
25	75	4.5	5.0

The films compared in the table above were all deposited at the same thickness of 150 nm for an accurate comparison, as thicker films tend to have rougher surfaces than thinner ones. The first parameter that was investigated was the influence of the substrate temperature. The temperature of the substrate was varied based on a prior report that depositing metal films, such as Al, Ti, and Cu, at substrate temperatures (T_s) from 30 – 50% of their melting temperature (T_m), enhances surface diffusion and results in smoother films.[138] As the melting point of aluminum is 660°C, this determined the first two condition listed in Table 4.1 above, corresponding to a T_s / T_m of 0.5 and 0.3.

Unfortunately, the results obtained from these conditions are not as good as the roughness obtained by depositing without heating. This could be due to the high base pressure of the sputtering, in which case, oxidation of the film may be enhanced at these elevated temperatures and coarsening may occur. In looking at the data from the table it would seem that temperature plays a large role in the surface roughness, had our sputtering system been appropriately equipped, it would have been beneficial to see the effects of sputtering at liquid nitrogen temperatures on the film quality and surface roughness. It has been reported that low temperature deposition helps to improve crystallinity and surface characteristics.[145]

After determining that lower temperature yielded a smoother Al surface than elevated temperature deposition, the influence of the sputtering power was analyzed, keeping other parameters constant. Room temperature Al thin film depositions were performed at sputtering powers of 150 W, 125 W, 100 W, and 75 W, for constant film thicknesses. The results in Table 4.1 show a decrease in the roughness of the Al film as the sputtering power is reduced from 150 W to 100 W. Upon further reduction to 75 W, the surface roughness increases. This may be due to the kinetics of the deposition process as the deposition rate was considerably slower at 6 nm / min at 75 W versus 8 nm / min at 100 W.

From the various parameters that were studied, the optimum condition was determined to consist of room temperature or unheated deposition at a sputtering power of 100 W, which yielded an RMS surface roughness of 3.0 nm for the Al film and 4.0 nm for the anodized Al film. For comparison, Figure 4.1 shows SEM images of the different Al films for the conditions listed in Table 4.1 above.

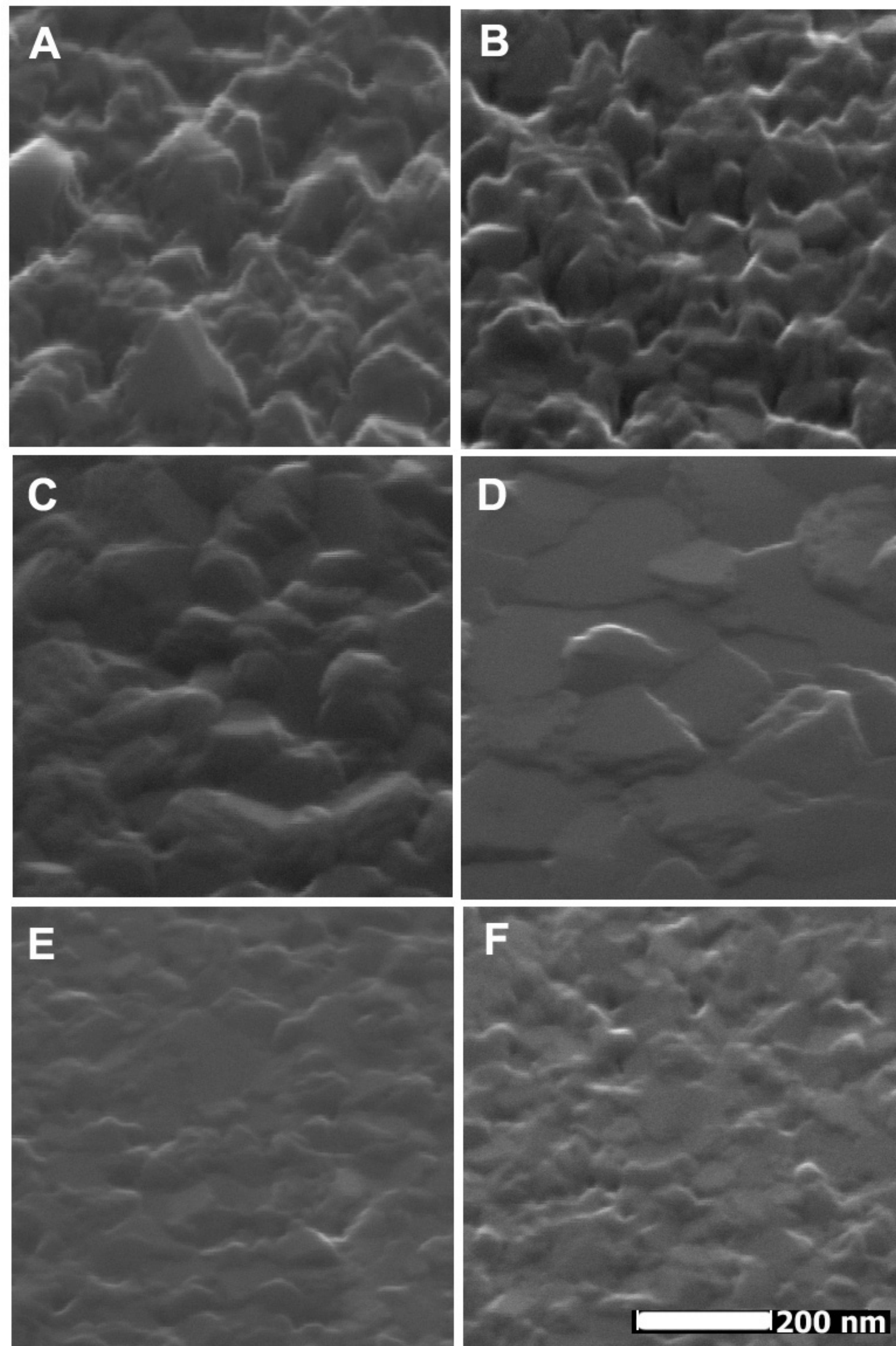

Figure 4.1: Scanning electron microscope images of the as-deposited Al films deposited at 330°C 150 W (A), 200°C 150 W (B), 25°C 150 W (C), 25°C 125 W (D), 25°C 100 W (E), and 25°C 75 W (F).

Figures 4.1 (A) – (C) shows the decrease in roughness as the deposition temperature is reduced from 330°C to 25°C. The dependence of the quality of the Al film on the sputtering power is shown in Figures 4.1 (C) – (F). As the SEM images show, a smoother surface is obtained when the sputtering power is decreased from 150 W to 100 W. Further decreases in the sputtering power, shown in Figure 4.1 (F), result in a rougher Al surface. The SEM images displayed in Figure 4.1 give a qualitative impression of the data shown in Table 4.1. However, it is hard to get a good impression of the surface topography from the SEM image alone and while it may be relatively straightforward to qualitatively judge the surface roughness, a quantitative surface roughness measurement by AFM is much more accurate. Figure 4.2 shows an AFM scan of the surface of the film resulting from the optimum sputtering condition of 25°C and 100 W.

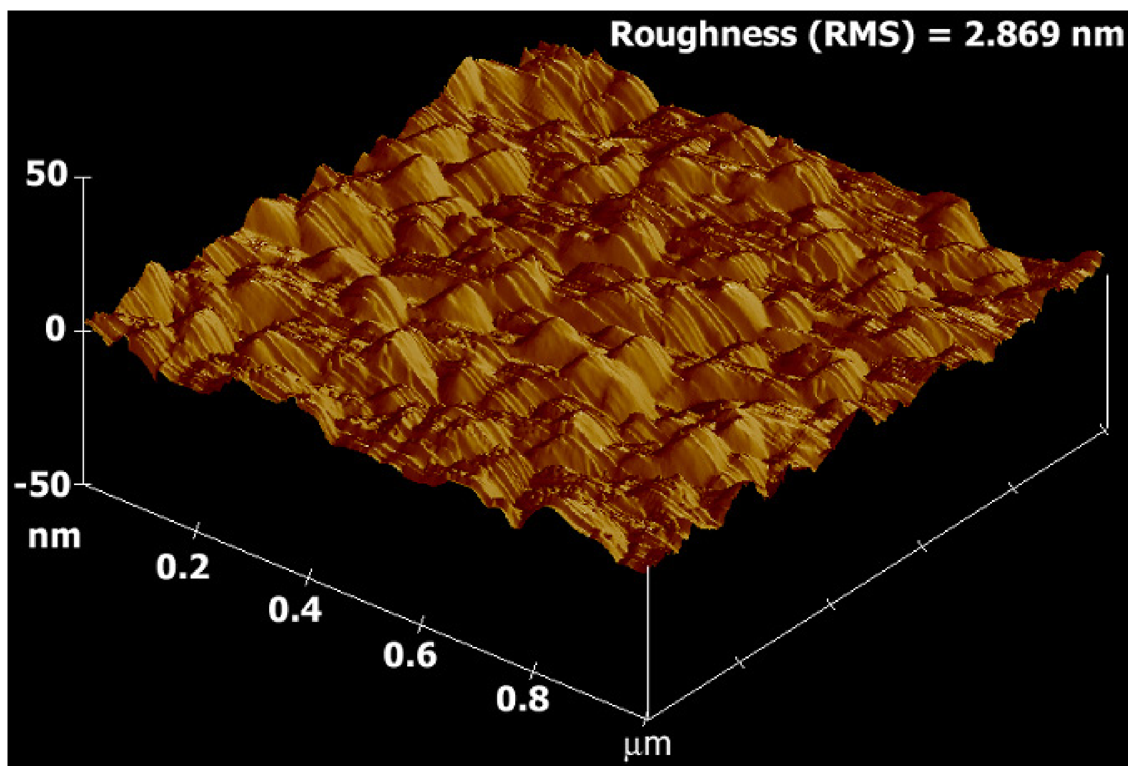

Figure 4.2: AFM image of the surface of the optimum sputtering condition of 25°C and 100 W, showing the RMS surface roughness.

Comparing the AFM scan along with SEM image of the same condition in Figure 4.1 (F) it is possible to get a comprehensive perspective of the surface characteristics.

While the surface roughness of the aluminum films is acceptable at this level, it would be better to obtain a smoother film. It has been suggested that surface roughness might be improved by depositing Al alloys, such as Al-Nb or Al-Zr, rather than pure Al, as these additions may help to control grain growth at elevated temperatures.[146] To investigate this possibility, Al-Zr, Al-Ti, Al-Ta, and Al-Cu alloy films were deposited and analyzed. Unfortunately, none yielded an improvement in surface roughness and some adversely affected the anodization process. Figure 4.3 shows the influence of 3

atomic % Ti and 3 atomic % Zr alloying elements on the as-deposited Al films as well as the change in anodization behavior with increasing amounts of Ta from 0 – 6 at. %.

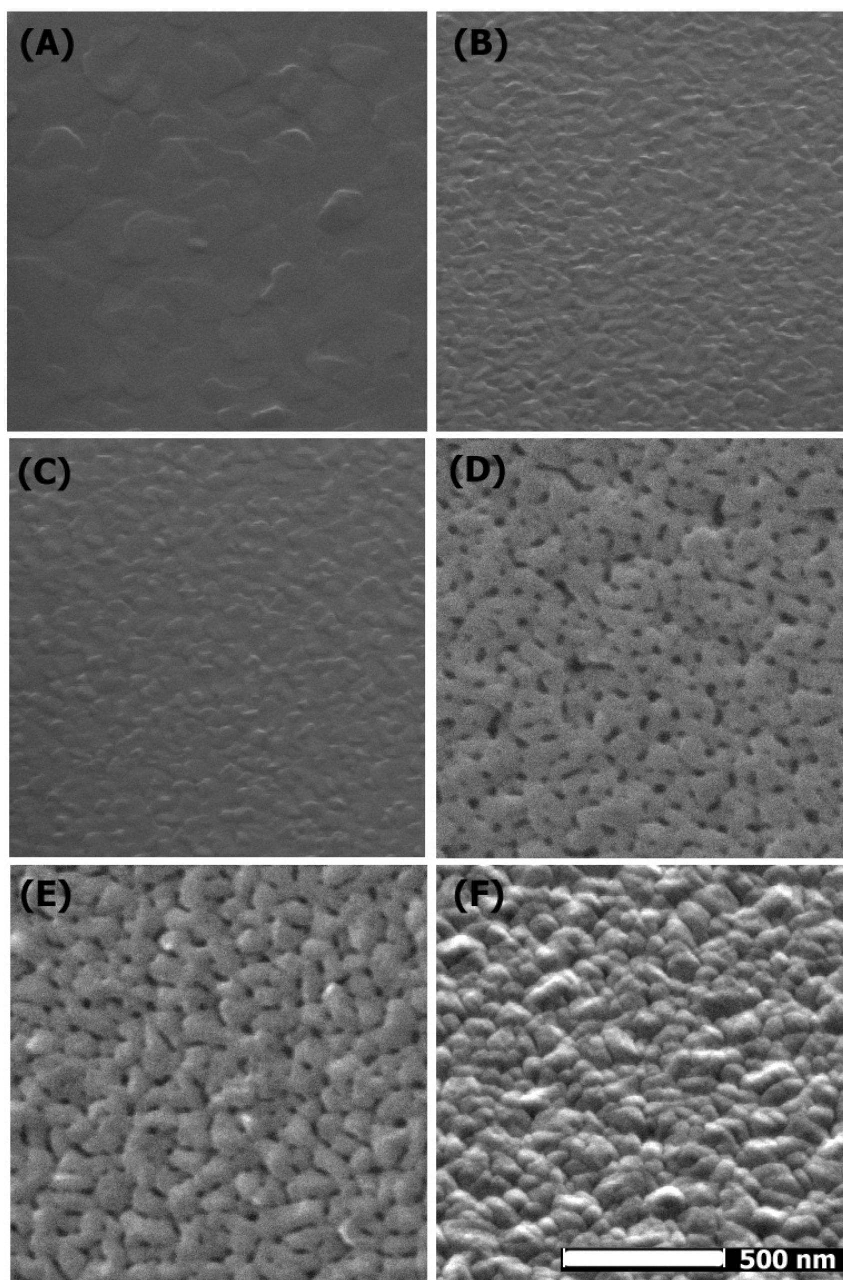

Figure 4.3: SEM images showing the influence of alloying elements on the Al films for 200 nm thick films. (A) as-deposited Al film, (B) $Al_{97}Ti_3$ film, (C) $Al_{97}Zr_3$ film, (D) anodized Al film, (E) anodized $Al_{97}Ta_3$ film, (F) anodized $Al_{94}Ta_6$ film.

The images in Figure 4.3 (A) – (C) show the increase in surface roughness with the addition of Ti and Zr alloying elements. The anodization process is obviously affected by the addition of larger amounts of Ta, shown in Figure 4.3 (D) – (F).

Another way of improving the surface roughness is through chemical mechanical polishing (CMP) of the as-deposited thin films. There are many parameters involved in the CMP process such as the slurry chemistry, the polishing pad, applied pressure, and speed. In order to improve upon an already mirror-like surface finish in the thin film, specialized fixtures and machinery are needed to hold the sample level and maintain an even polish to within the nanometer dimensions that are needed. With CMP there is usually significant material removal, which means that the process requires a much thicker starting film. Lacking appropriate equipment for CMP and the cost of outsourcing the work limited its usefulness for this research work. However, it should be mentioned that recent CMP performed on 4 μm thick Al films by D.S. Industries yielded an RMS surface roughness of 2 nm; although these results appear to be difficult to reproduce. SEM images of the surface of the Al film after the CMP process and after anodization are shown in Figures 4.4 (A) and (B).

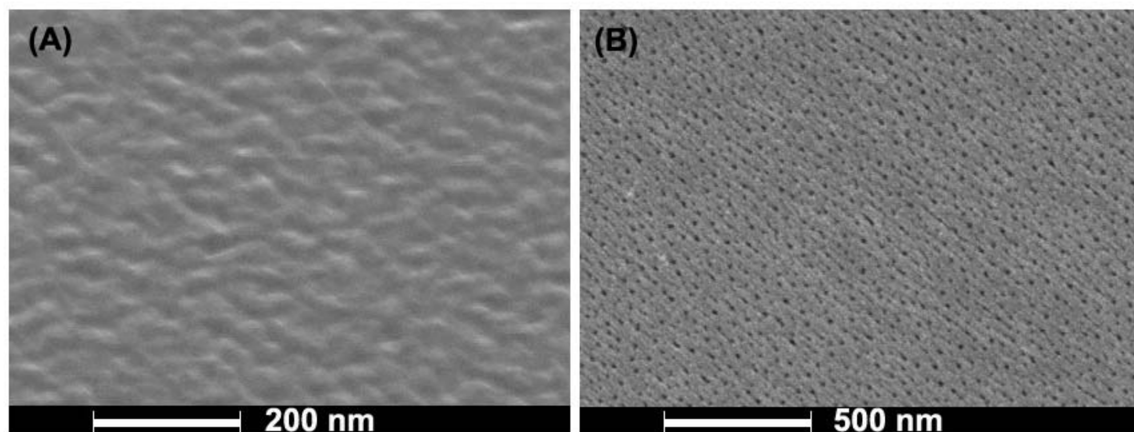

Figure 4.4: SEM images showing the surface of the Al film after chemical mechanical polishing (A) and the top surface of the same film after anodization at 25 V in 0.3 M oxalic acid at 5ºC (B).

Compared to the thinner 150 nm Al film prepared under the deposition conditions described previously and shown in Figure 4.1 (F), the Al film after chemical mechanical polishing appears to be somewhat smoother with more regular surface features. The anodized CMP film showed moderate improvements in the regularity of the pore structures and will be utilized in future experiments.

4.2 Anodization of aluminum films

The nanoporous templates fabricated for this research were prepared both with a two-step anodization procedure, as described previously in sections 2.3.2.3 and 3.3, and with a single step anodization process. SEM images from an Al film anodized in a single-step anodization procedure using 0.3 M oxalic acid at 5°C and an applied voltage of 25 V are shown below in Figure 4.5.

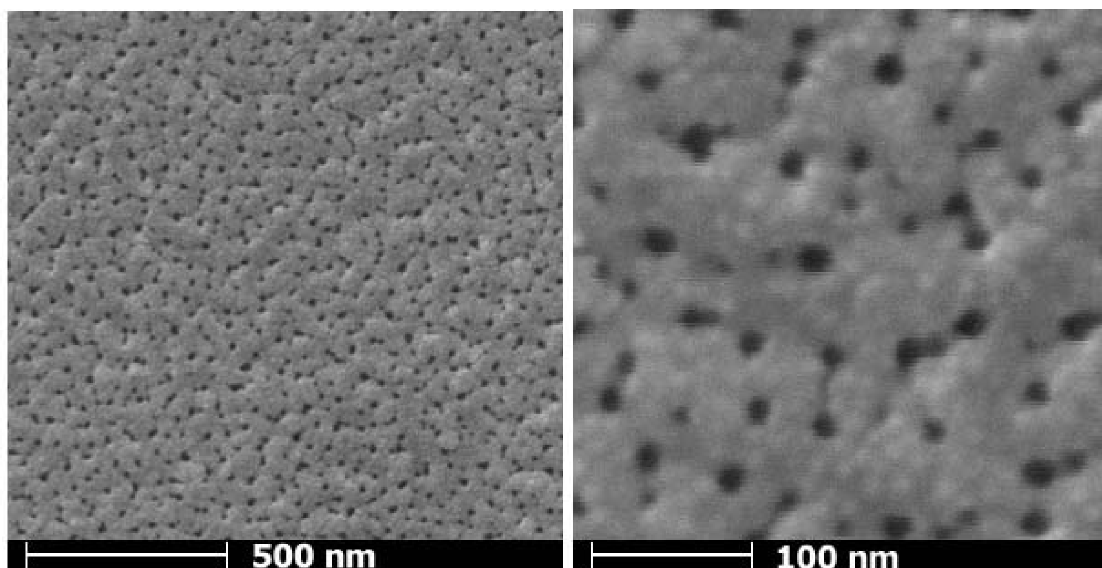

Figure 4.5: SEM images showing the top surface of an Al film anodized in 0.3 M oxalic acid at 5°C and an applied voltage of 25 V (A), and a higher magnification image of the top surface (B).

As the images in Figure 4.5 show, the ordering of the pores is not that regular, yet small pores of ~ 20 nm diameter are obtained with a straight and vertical structure that are more ordered below the surface than they appear on the top, which is proven by the nature of the nanowires that are formed, as will be shown later in section 4.3.1.

The variation in current over the anodization process is indicative of the main events that occur during anodization. A plot showing the sample current versus time during a constant voltage anodization at 25 V is shown in Figure 4.6.

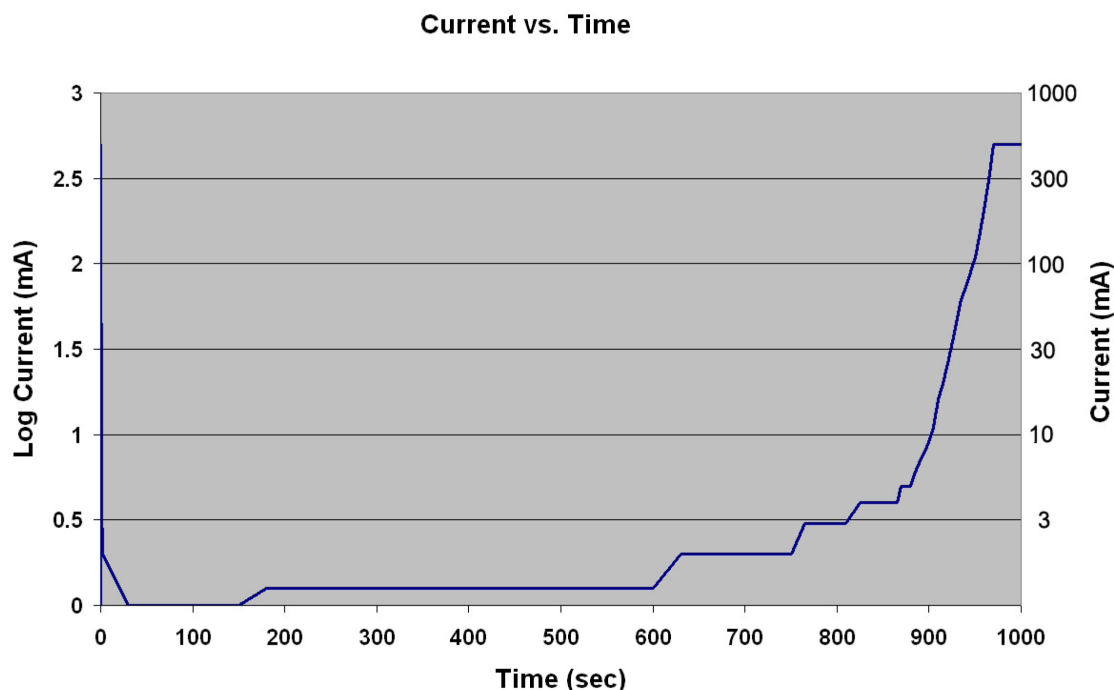

Figure 4.6: Plot showing the increase in current over the course of the anodization process carried out at 25 V in 0.3 M oxalic acid at 5°C.

Initially there is an extremely rapid asymptotic decrease in the current as the voltage is applied, which corresponds to an initial barrier oxide layer formation. Following this, the current starts and remains at near zero levels for a long time, indicating steady state pore growth. As time continues, the current begins to slowly and steadily rise resulting from further consumption of the Al layer as the anodization front approaches the metal underlayers. Towards the end of the anodization process the current increases exponentially, indicating that the Al layer has been fully consumed and the Au underlayer is being exposed as the Ni layer is anodized. Normally, anodization is stopped when a current density of 250 mA / cm^2 is reached, but in obtaining data for this graph the anodization was continued until the maximum current limit of the power supply of 500 mA was reached. Anodizing to this point generally results in destruction

of the porous layer as the rapid evolution of gas bubbles results in localized and then widespread rupturing and delamination of the AAO layer.

In attempts to improve the pore ordering, a two-step anodization process was undertaken. The experimental process for the two-step anodization is summarized in the schematic diagrams shown below in Figure 4.7.

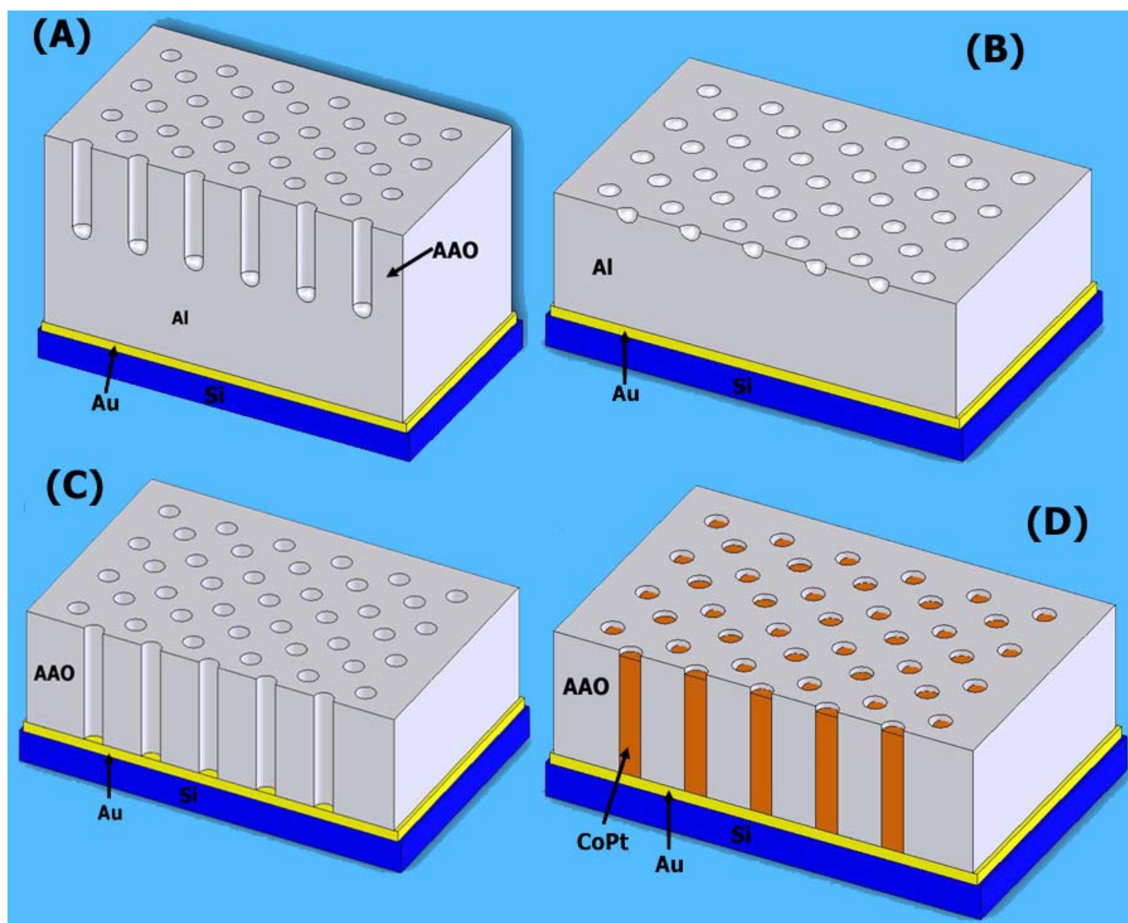

Figure 4.7: Schematic diagrams showing the procedure for a two-step anodization. (A) partial anodization of the Al layer, (B) removal of the anodized layer leaving the depressions from the pore bases as nucleation sites for the next anodization step, (C) second anodization to create through pores to the metal underlayer, and (D) electrodeposition to create nanowires.

This two-step anodization process does improve the order somewhat, but there is really not a thick enough layer of Al for the self-ordering process to really take effect, as supported by Table 2.5.[51] Some SEM images of samples after a two-step anodization process are shown in Figure 4.8.

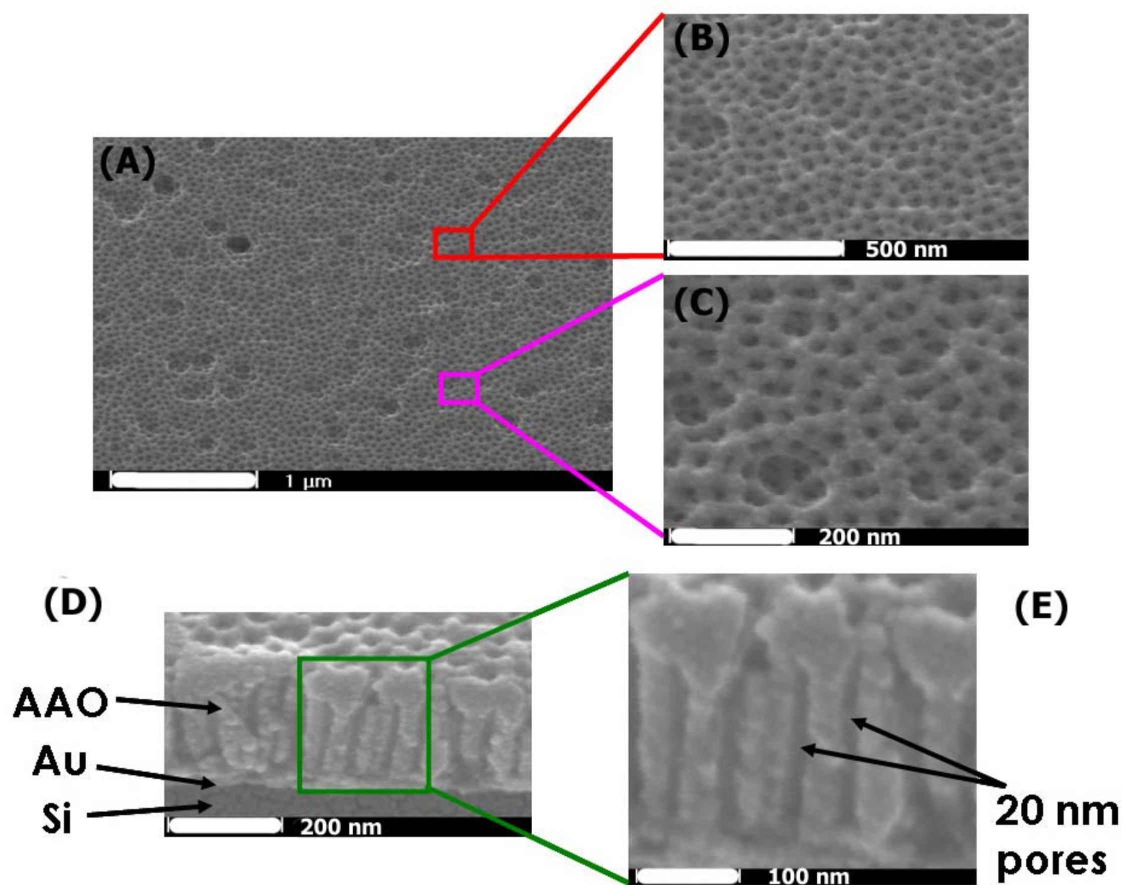

Figure 4.8: SEM images of a sample after a two-step anodization process. The top surface is shown, displaying improved pore regularity at low magnification (A), at successively higher magnification (B) and (C), and a cross-sectional image showing the pore structure at lower magnification (D), and a higher magnification cross-sectional image (E).

In looking at the SEM images in Figure 4.8, the top surface shows much more clearly defined pores, resulting from the pores forming in the depressions left behind by the first anodization layer. The pores may not be much more ordered than a single-step anodization process; however, they may appear that way due to their clearly defined and broader boundaries. Starting with a film thickness of around 500 nm it is very difficult to reliably perform a two-step anodization process because if the first anodization step is too long, there will not be enough Al left to properly anodize in the second anodization step. It is hard to obtain nanometer level precision when performing the anodization step. Also, when stripping the first anodization layer, the etching step is carried out in a mixture of phosphoric and chromic acid at 60°C. This step also needs to be accurately controlled as the hot acid solution has a tendency of seeping underneath the insulating lacquer, exposing the metallic underlayers and the electrical connection to the anodization solution during the second anodization step, short circuiting the anodization process. Over-etching and reaction with the remaining Al layer are also concerns.

4.3 Nanowire deposition into the AAO pores

4.3.1 CoPt Nanowires

4.3.1.1 Fabrication of CoPt nanowires

The CoPt nanowires were fabricated using an electrodeposition process as mentioned previously in section 3.4. Depending on the amount of Al deposited and the resulting height of the AAO, the length of the nanowires could be varied. However, great care must be taken to prevent the nanowires from growing past the top of the pore

structure of the template and overflowing onto the surface of the template. If this does occur, at first a mushroom shaped cap forms on top of the nanowire base and if electrodeposition is continued, ultimately a thin film will form on the surface of the template. Once the nanowire grows past the template it will no longer exhibit the unique characteristics of a nanowire and will approach those of the bulk material. The length of the nanowires depends on the electrodeposition time, however, achieving nanoscale control of the height is very challenging and the height uniformity varies within a given sample. The most successful results were achieved using a more dilute electrolyte solution in order to slow down the growth rate during electrodeposition and obtain finer control.

To determine the correct electrodeposition conditions for the CoPt nanowires it was necessary to perform preliminary experiments to determine how the composition of the nanowires varied with the current density. The composition of the nanowires is very important because when the composition is outside the range of the $L1_0$ phase, shown in the Co-Pt phase diagram in Figure 2.31, high coercivities are not achieved. Figure 4.9 shows the variation in composition as the electrodeposition current density increases.

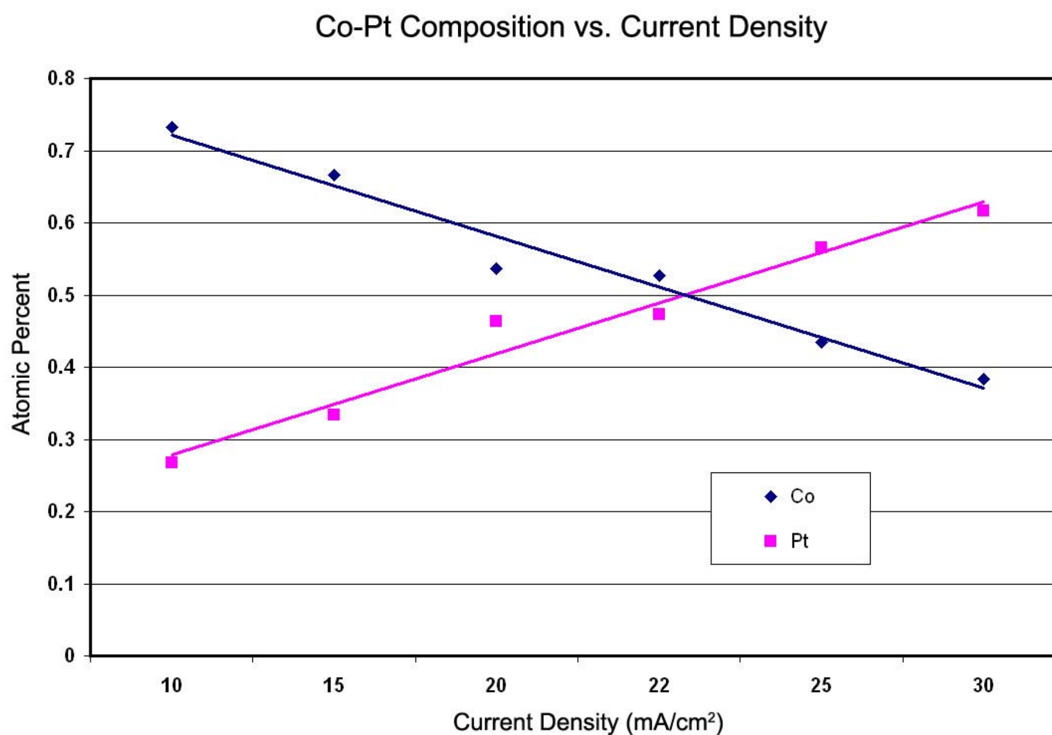

Figure 4.9: A graph showing the variation in Co and Pt composition in atomic percent as determined by EDS analysis when the electrodeposition current density is increased.

At low electrodeposition current densities the rate of Co deposition is much higher than that of platinum, perhaps due to differences in the ion sizes and their mobilities. As the current density increases, there is a steady rise in the rate of Pt deposition and a decline in the rate of Co deposition. The deposition rates of the two elements become equivalent at a current density of 23 mA / cm^2 before diverging again at higher current densities. Based on these experimental results, an electrodeposition current density of 23 mA / cm^2 was used for all subsequent CoPt depositions. It should be noted that since the composition was measured using EDS analysis, it represents the average composition over a given area rather than the composition of individual nanowires.

One of the things desired for patterned recording media is short, uniform nanowires that are isolated from one another. The AAO template serves to separate the nanowires, but its typically large height is undesirable as the nanowires must be grown up to the surface or overgrown onto the top of the AAO template and then polished down to reach the desired height in order to be in close proximity to the surface and accessible for magnetic applications. Both of these approaches create problems. The polishing procedure introduces another complex process to the fabrication and may result in sample contamination from the polishing slurries. Long nanowires are not advantageous because it is desirable for easier magnetization that the height or length of the nanowires needs to be relatively short, typically less than five times the diameter of the nanowire for a given intensity of the write head field. For these reasons, short CoPt nanowires approximately 100 nm long reaching the top of the AAO template were fabricated.

To fabricate these nanowires, it was first necessary to produce a thinner AAO structure. This was accomplished via a two-step anodization process starting with an initial Al layer thickness of ~500 nm. The first anodization step lasted for 5 minutes and then following the stripping of the first anodization layer the remaining Al layer was completely anodized. The template that was formed exhibits ~20 nm diameter pores with an average spacing between holes of ~50 nm. The CoPt nanowires were then electrodeposited into the pores at a current density of 23 mA / cm^2 with the deposition time being carefully controlled in order to prevent overgrowth. Figure 4.10 shows an SEM image of the fabricated structure consisting of the AAO template and the

CoPt nanowires. The image was obtained by cleaving the sample to produce a visible edge while still maintaining the integrity of the AAO template.

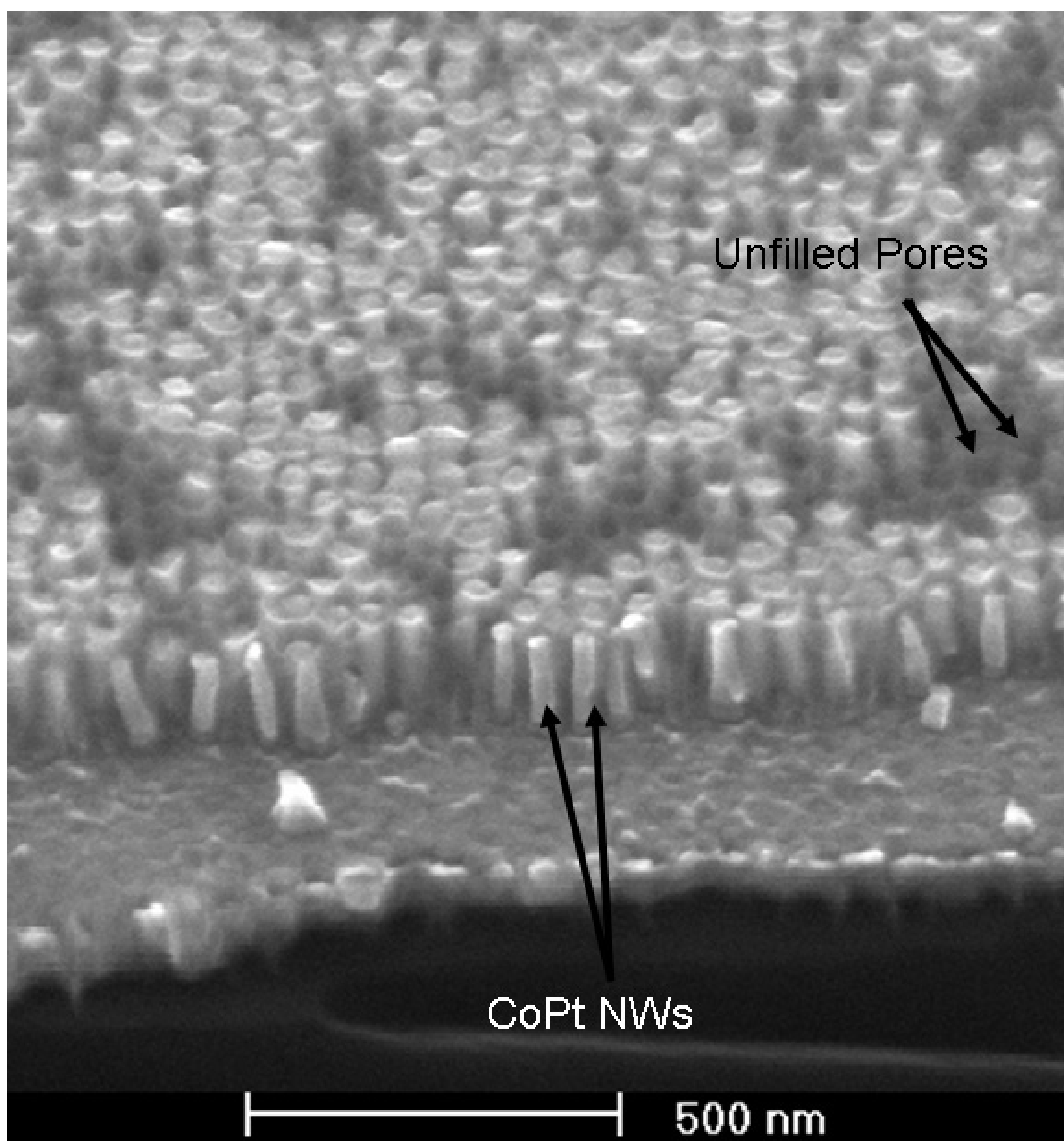

Figure 4.10: SEM image showing the AAO template and embedded CoPt nanowires, the edge was exposed by fracturing the sample, showing the height of the nanowires and the template.

Figure 4.10 shows that the pores of the sample, and therefore the nanowires, have an approximate average height of ~100-150 nm and an average diameter of ~20 nm, giving them the desirable 5:1 aspect ratio (length : diameter) as mentioned above. The top of the CoPt nanowires, show a circular geometry that in some cases is beginning to broaden out slightly larger than the nanowire diameter which is consistent with scalloped shape of the tops of the pores resulting from the two-step anodization process. The height of the nanowires is dependent on the time and other parameters of the electrochemical deposition. Here, the electrochemical deposition for the CoPt nanowires shown in Figure 4.10 took only about one minute. The CoPt nanowires fill the pores with a relatively uniform height, reaching the top of the pores without growing out of the pores or forming a film of CoPt on the surface of the AAO layer. Using different Al film thicknesses and varying the electrodeposition time it is possible to fabricate longer nanowires and shorter nanowires. Figure 4.11 shows CoPt nanowires of several different lengths that have been fabricated.

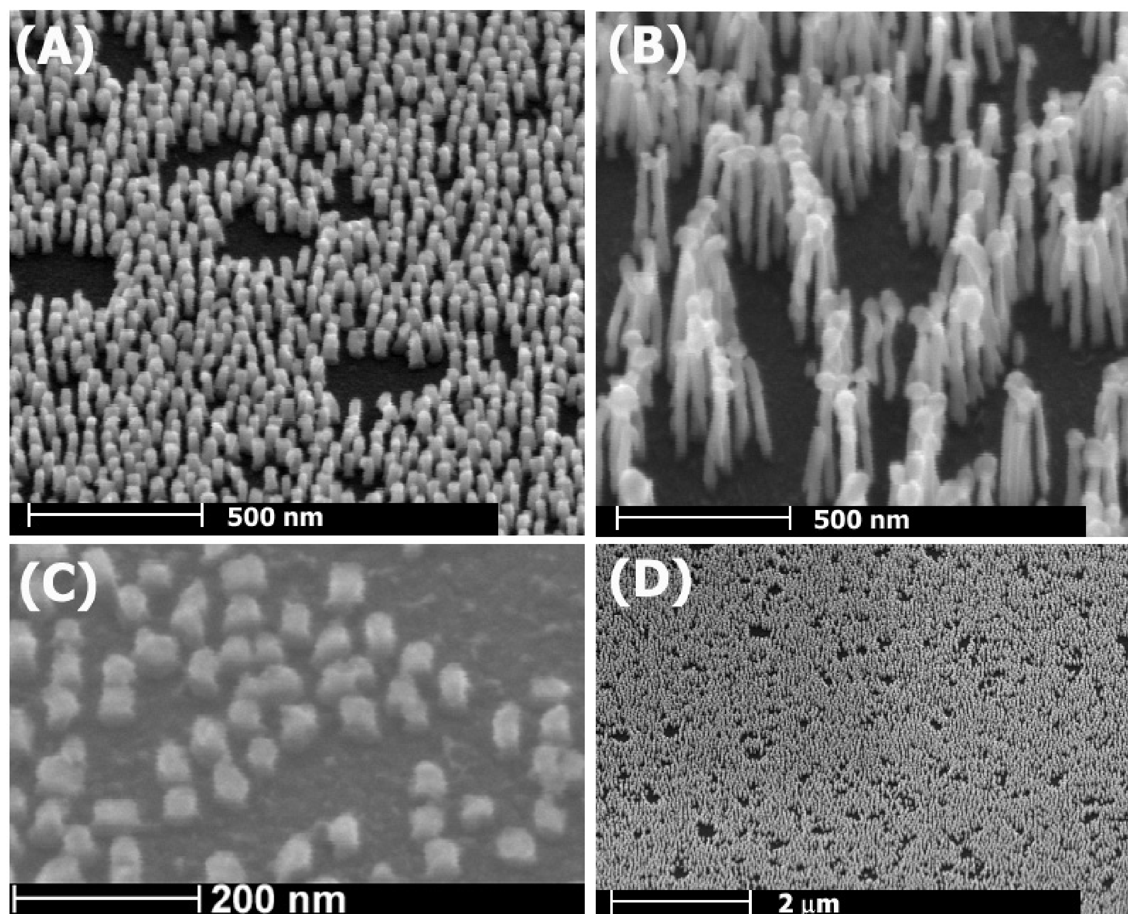

Figure 4.11: SEM images showing CoPt nanowires of different lengths that have been fabricated, ~30 nm (A), ~100 nm (B), ~500 nm (C), and a low magnification image showing the coverage of CoPt nanowires on the substrate (D).

In Figure 4.11 (B) the ~500 nm nanowires are slightly longer than the pores and as the nanowire grows out of the shelter of the pore structure it begins to broaden out and form a mushroom cap on top of the nanowire structure. Figure 4.11 (D) shows the extent and efficiency of nanowire coverage on the surface of the substrate. For the most part, the surface is uniformly covered with nanowires of approximately the same height, albeit with some local variations. There are, however, some areas showing no nanowire

nucleation. These may result from local variations in the barrier layer thickness, leaving an insulating covering layer over the underlying Au layer.

Another interesting view of the CoPt nanowires inside of the AAO template can be obtained using focused ion beam (FIB) techniques. Using an FIB, the edge of the AAO template can be removed by ion milling at an angle so as to expose the CoPt nanowires inside of the AAO template. Figure 4.12 shows the resulting image obtained when the correct processing parameters are chosen.

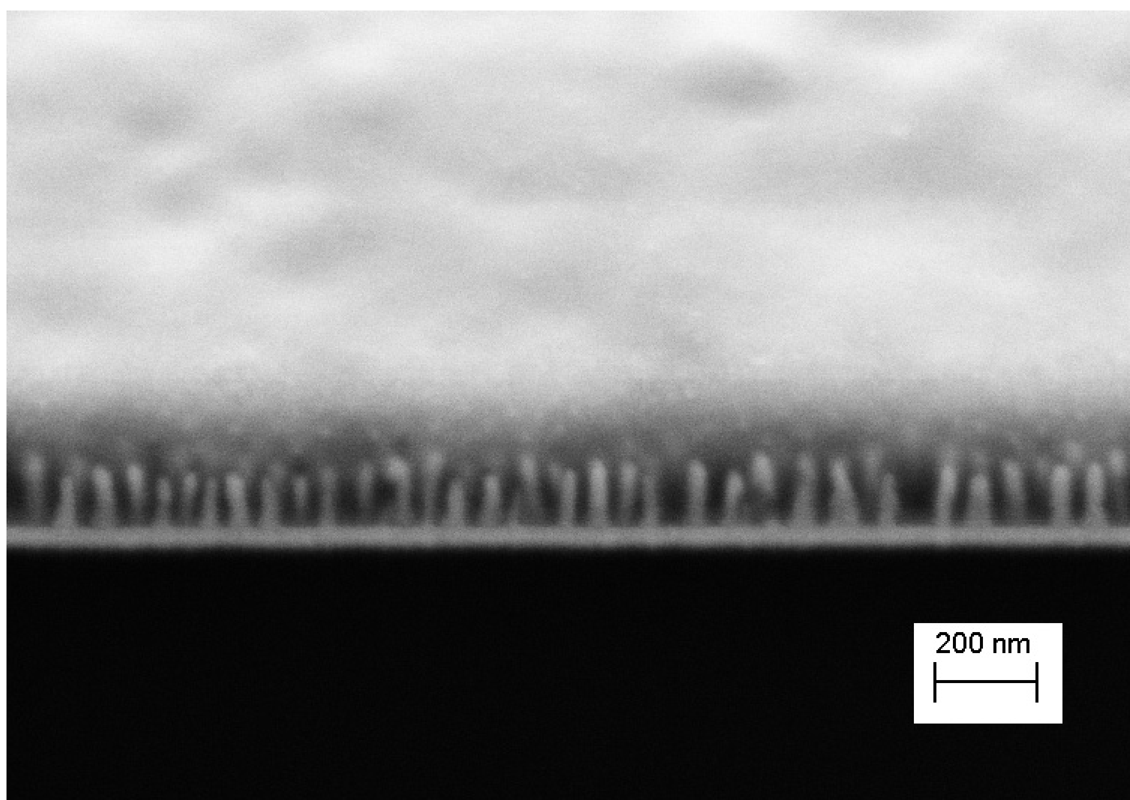

Figure 4.12: An SEM image of CoPt nanowires exposed by ion milling from a focused ion beam to remove the surrounding AAO template.

The CoPt nanowires can be seen extending perpendicularly upwards from the substrate in the region where the AAO template has been removed by FIB. The parts of the AAO template that have not been removed are seen as the white layer covering the nanowires. This shows how the nanowires that were grown remain inside the porous layer and did not grow out onto the surface of the AAO template.

To convert the nanowires to the $L1_0$ phase a high temperature annealing treatment is necessary, as was previously discussed in section 2.4.2. One of the advantages of the AAO template is that even with this high temperature heat treatment at 700ºC the nanowire diameter is maintained without coarsening since the CoPt nanowire array is laterally constrained by the surrounding AAO matrix.

4.3.1.2 Microstructure and composition of CoPt nanowires

The composition of the ~20 nm diameter CoPt nanowires deposited in the AAO template was determined by EDS analysis to be on average approximately 50:50 in atomic %, with possible nanowire compositions likely ranging between $Co_{60}Pt_{40}$ to $Co_{40}Pt_{60}$. This variation is within the typical composition range of the $L1_0$ CoPt phase, according to the phase diagram appearing in Figure 2.31. The as-deposited CoPt nanowires exhibit low coercivity and are clearly not in the $L1_0$ phase, most likely having a disordered FCC structure. The physical characteristics of the nanowires can be observed from the SEM images shown above in Figures 4.10, 4.11, and 4.12.

The EDS analysis was quite sensitive to the composition of the nanowires. To obtain a more accurate measurement, EDS measurements were taken at multiple magnifications ranging from 100,000X to 10,000X, and the numerical results for atomic

percent composition were then averaged. In comparison to the abundance of other elements, namely Si from the underlying Si wafer and Al and O from the AAO template, there were relatively small amounts of the Co and Pt elements. The penetration depth for EDS measurements is on the micron scale so it is not merely the surface area that the elements cover, but their total volume. When this is taken into account there is obviously much more Si detected than anything else, as the nanowires and AAO template are at most only 500 nm thick. Figure 4.13 shows an EDS scan obtained for a sample of CoPt nanowires after the annealing treatment.

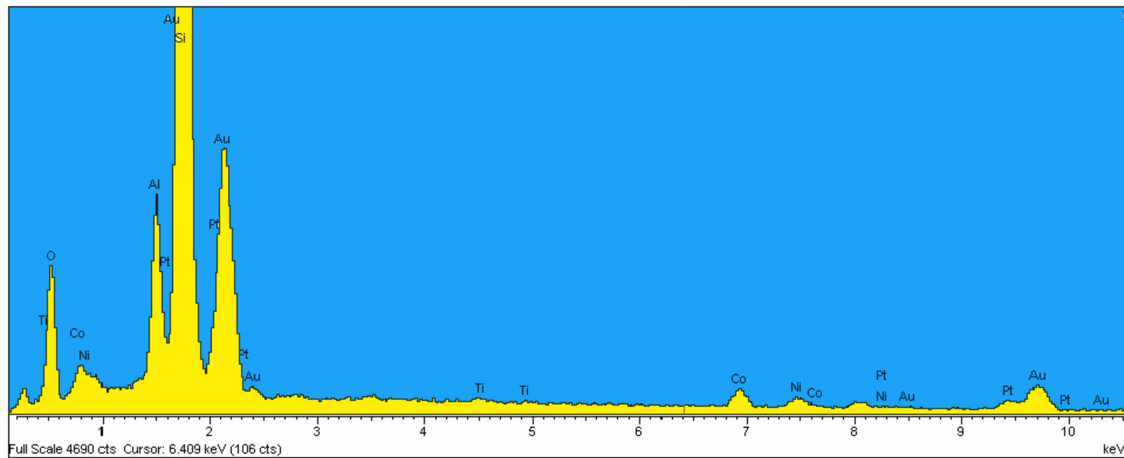

Figure 4.13: An EDS scan showing the number of counts obtained for each element in a sample of CoPt nanowires subjected to a post-deposition annealing treatment at 700°C.

From the figure, the tallest single peaks are from the Si, Al, and O. The Al and O show the presence of the AAO template, even after the annealing treatment. Other elements that show up are Ti, Au, and Ni, comprising the metal underlayers between the Si and the Al. The Ni still exists in small amounts, as it remains intact under the AAO template regions between the pores and as part of a partially anodized Ni_xO_{1-x} layer.

The Ti layer is completely covered by the Au layer and is never exposed to any electrochemical environment and is therefore unaltered throughout the experimental process. The Co and Pt peaks are interspersed with many of the other elemental peaks. The composition of the CoPt nanowires from this sample was measured to be $Co_{48}Pt_{52}$.

After depositing the nanowires an annealing treatment was necessary to convert the as-deposited material to the ordered $L1_0$ phase. The heat treatment was performed under a hydrogen atmosphere to prevent any oxidation during exposure to the high temperatures required. An annealing temperature of 700°C was used based on prior reports.[108, 110, 111] A plot of the heat treatment schedule is shown in Figure 3.3 and more details of the experimental setup for the furnace are given in section 3.5. Unfortunately, the setup and characteristics of the furnace required very long cool down times before safe temperatures could be reached to prevent any oxidation on exposure to the atmosphere when the sample was unloaded. This can be seen from Figure 3.3 where the furnace cooled from 700°C to 300°C in 150 minutes, with further cooling continuing at even slower rates. Typically, the samples were allowed to cool overnight to room temperature after annealing before they were removed from the furnace. These long cooling times negated the effects of varying the annealing time on the magnetic properties, with essentially no influence shown.

4.3.1.3 Magnetic data for CoPt nanowires

The magnetic properties of the CoPt nanowires were measured with an alternating gradient magnetometer (AGM) as this provided better sensitivity than a standard Vibrating Sample Magnetometer (VSM). Measurements were performed on

samples similar to that shown in Figure 4.10 with short ~100 nm long nanowires with a diameter of ~20 nm inside of a thin ~100 nm tall AAO template. Figure 4.14 shows the M-H loops measured in the in-plane and perpendicular directions for the as-deposited and annealed ~20 nm CoPt nanowires. The M-H loops shown are normalized to the maximum applied field of 14 kOe in order to present a more accurate comparison.

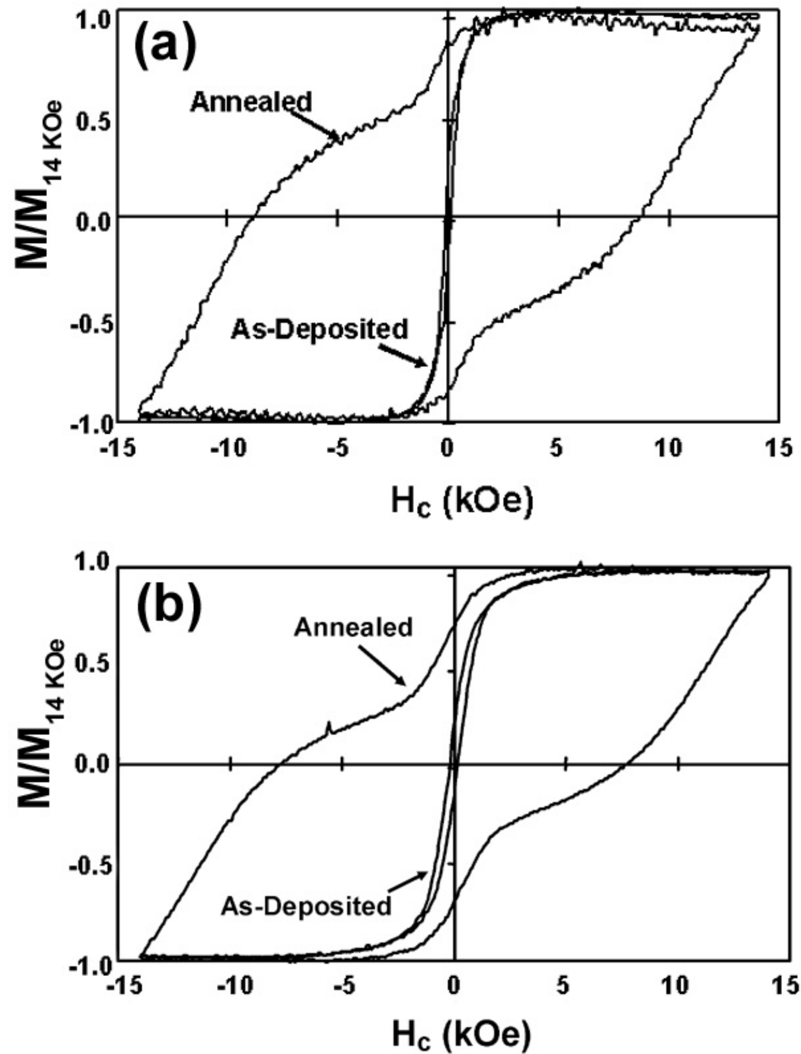

Figure 4.14: M-H loops showing the magnetic properties of the annealed and as-deposited CoPt nanowires, measured in the in-plane direction parallel to the substrate (A), and in the perpendicular direction along the nanowire axis (B).[147]

As shown in Figure 4.14 (A), the as-deposited sample exhibits an in-plane coercivity of only 110 Oe and a saturation moment of ~510 emu / cm^3, as estimated based on the volume of the magnetic CoPt nanowire material in the AAO template. In order to improve the magnetic properties of the CoPt nanowires, the sample was annealed under a hydrogen atmosphere at 700ºC for 30 minutes to form the ordered $L1_0$ phase. Following annealing, an in-plane coercivity of 8.5 kOe was obtained for the CoPt nanowires. Due to annealing, the magnetic moment of these nanowires increases to ~720 emu / cm^3. While the M-H loop is not saturated, it appears to be close to saturation. The observed magnetic moment is comparable to the known saturation value of 800 emu / cm^3 for the $L1_0$ CoPt phase, although it is still ~10 % lower than the reported value, presumably due to inaccuracies in estimating the volume of CoPt material and also the intensity of the applied magnetic field.[148]

Figure 4.14 (B) shows the M-H loops measured in the perpendicular direction, along the growth direction of the nanowires, for both the as-deposited and annealed CoPt nanowires. Similar coercivity values were obtained for both perpendicular and in-plane directions. The as-deposited CoPt nanowires show a perpendicular coercivity of 170 Oe, which increased to 7.7 kOe after annealing. The larger perpendicular coercivity for the as-deposited CoPt sample is due to the effects of shape anisotropy resulting from the aspect ratio of the nanowires. Though it is still present in the annealed samples, the influence of shape anisotropy is not seen in the M-H loop because the large magnetocrystalline anisotropy resulting from the ordered $L1_0$ phase is much more dominant.[108] The fact that the M-H loops measured in-plane and perpendicular show nearly-isotropic magnetic behavior could be due to the fact that the

nanowires may not be oriented in the proper anisotropy direction. The shape of the hysteresis loops in Figure 4.14 and the fact that the measured magnetic moment of these samples is lower than that reported for the pure $L1_0$ phase probably indicates the presence of two phases. As reported in previous papers, the phases are most likely the face-centered cubic and face-centered tetragonal $L1_0$ phases of CoPt alloys.[108, 109] There are in fact two possibilities for a near uniform CoPt composition, either one phase is the ordered $L1_0$ phase with the other being the low-H_c face centered cubic (fcc) CoPt phase, or both are the $L1_0$ phase but with different stoichiometry and therefore different magnetic anisotropy and coercivity. In the event of localized composition variations it is possible that other phases such as the $L1_2$ $CoPt_3$ or the hexagonal close packed (hcp) Co_3Pt phase might be present, which could also account for the difference in properties from those reported for the pure $L1_0$ phase.[149]

The presence of multiple phases and the possibility of localized composition variations may also result from difficulties in controlling the composition of the nanowires. Mallet et al. reported problems in controlling the composition of 35 nm diameter CoPt nanowires due to hydrogen evolution during the electrodeposition process, however, no difficulties were reported when depositing larger 80 nm diameter nanowires.[108] It seems that this becomes increasingly problematic as the AAO pore size decreases. Similar problems may occur in the case of these ~20 nm diameter pores, and may even be enhanced by the smaller diameter pores, thereby explaining some of problems in obtaining a uniform composition. During the electrodeposition process the AAO samples routinely come into contact with many different chemical species in the complex bath solutions. Because of this, sample contamination was a big concern. To

minimize this possibility, the samples were thoroughly rinsed in deionized water before and after electrodeposition to clean the sample and remove any traces of foreign elements from the anodization electrolyte and the electrodeposition bath. Despite this, there was still a chance of impurities being incorporated into the deposited nanowires. EDS analysis never confirmed the presence of any contaminating elements, save for occasional traces of copper which must have originated from exposure of the conducting copper electrical lead due to poor coverage with the insulating lacquer. There was one previously published paper citing the influence of Cu doping in FCC Co_3Pt nanowires in which the authors observed a slight increase in the coercivity from 600 Oe to 850 Oe with the addition 19 atomic % Cu.[150] The amount of Cu detected during EDS analysis of the samples for this research was very small, less than 1 atomic %, typically on the scale of the amount of error in the EDS measurements, and the majority of times Cu was not detected at all. The magnetic data acquired for various samples showed no enhancement or reduction in coercivity for samples with detectable amounts of Cu.

In efforts to fabricate magnetic nanowires with perpendicular anisotropy, attempts were made at using different underlayer materials to promote specific crystallographic orientations within the CoPt nanowires. Pattanaik et al. reported that using an Ru underlayer facilitated the growth of an oriented hexagonal Co-rich $Co_{80}Pt_{20}$ thin film deposited via electrodeposition.[151] The 150 nm thin film exhibited perpendicular coercivities of 4.5 kOe with in-plane coercivities of only ~250 Oe.[149] When trying to adapt this approach to AAO templates there was a problem with the Ru compatibility to the anodization process. During anodization the Ru layer reacted with

the anodization solution resulting in the detachment of the Al/AAO layer. Attempts were made at using a Ni buffer layer between the Ru layer and the Al layer but this did little to alleviate the problem and towards the end of anodization the same delamination of the Al layer was observed. If the anodization process was stopped short of fully consuming the Al layer then there was no electrical connection between the electrodeposition solution and the Ru underlayer and no nanowires could be formed. It is also likely that the presence of a Ni intermediary layer would negate the benefits of the Ru layer.

4.3.2 Ni/CoPt composite nanowires

4.3.2.1 Fabrication of Ni/CoPt composite nanowires

The coercivity of the fabricated CoPt nanowires discussed in the previous section is quite large and may pose significant problems for potential magnetic data recording at currently available magnetic write head fields. One approach of solving this problem is to create a composite nanowire structure combining soft and hard magnetic materials. This type of composite recording media was proposed in 2005 by Victora and Shen.[152] Using exchange coupling between the two layers, the soft magnetic layer assists the switching of the hard layer by altering the direction of the applied field, allowing switching of the hard layer with a lower applied field.[153] From the theoretical studies, the best results were found when the ratio of saturation magnetization of the soft layer to the hard layer is 0.1 – 0.3 and the coercivity of the hard layer is much greater than the coercivity of the soft layer.[152] The relative volumes of the layers is also a factor but in the studies mentioned it was fixed at the volume of

the soft layer being twice that of the hard layer.[152, 153] As of yet, there have been no experimental reports of soft/hard nanowire composite materials that approximate this type of composite media structure. As part of this research work, successful fabrication of arrays of soft/hard composite nanowires has been accomplished and the magnetic properties have been measured.

To give a clearer picture of the structure, a schematic diagram showing the Ni/CoPt composite nanowires within the porous AAO matrix is shown below in Figure 4.15.

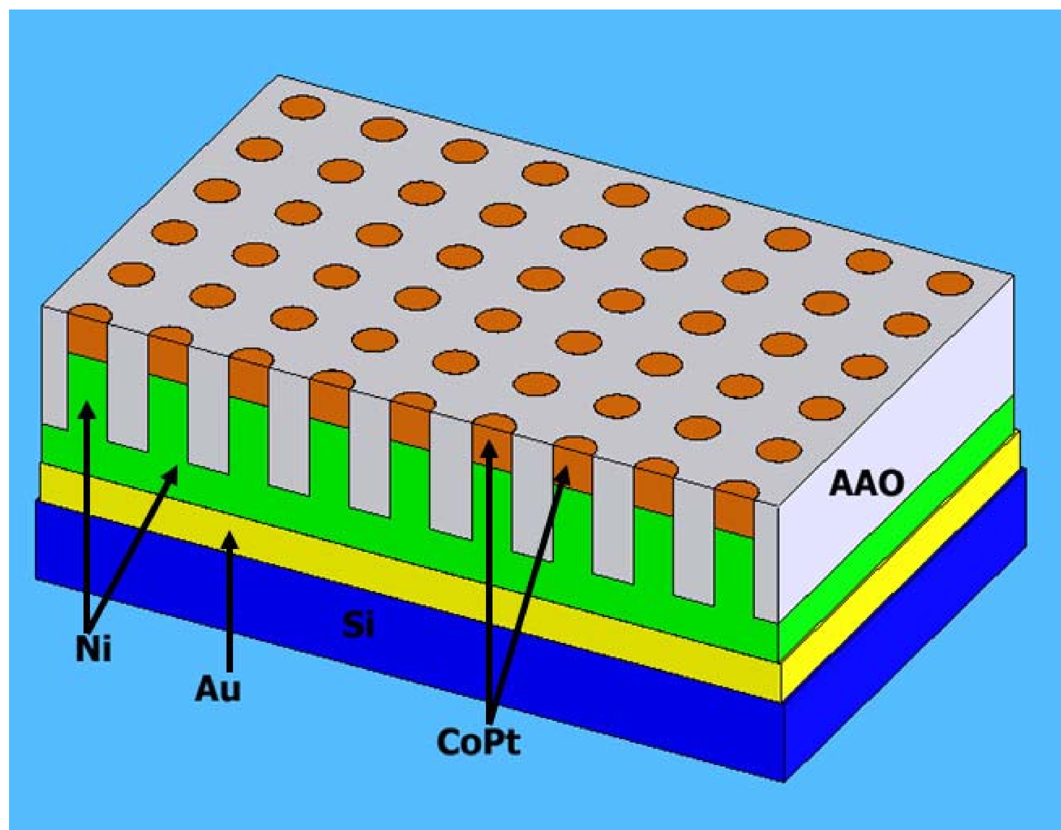

Figure 4.15: A schematic diagram showing the structure of the fabricated Ni/CoPt composite nanowires in the AAO template.

As the figure shows, the presence of the Ni film underneath the segments of Ni nanowires also serves as a soft magnetic underlayer (SUL). The presence of the soft magnetic underlayer enhances the available write head field by channeling the magnetic flux from the write pole to the return pole, essentially placing the magnetic medium between two poles.[137] There is also evidence that the presence of an SUL helps to increase the signal-to-noise ratio in AAO-based patterned media.[154] An SEM image of the as-deposited Ni/CoPt nanowires is shown in Figure 4.16 from a viewing angle of 45°.

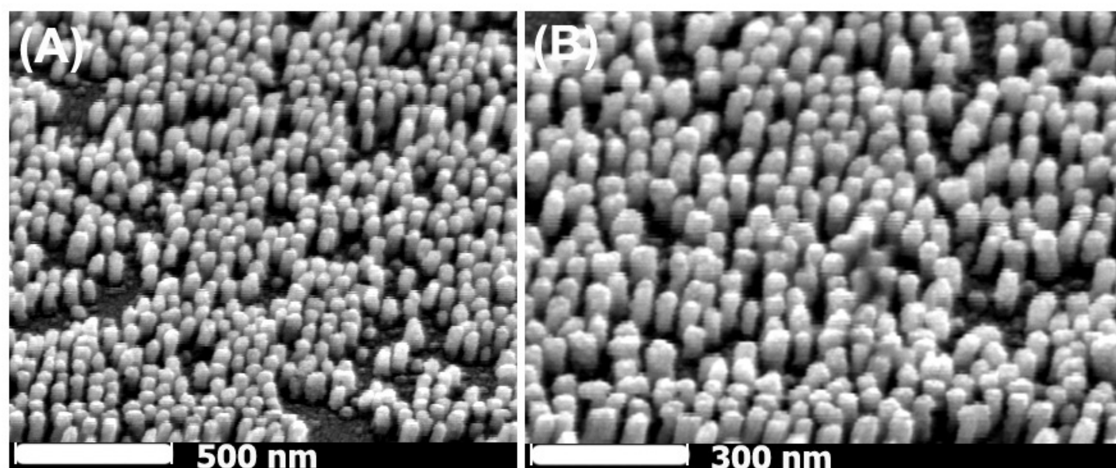

Figure 4.16: SEM images showing the composite Ni/CoPt nanowires from a 45° angle after removal of the AAO template via chemical etching to expose the nanowires, at lower magnification (A) and higher magnification (B).

The nanowires were exposed by removing the AAO template via chemical etching in a sodium hydroxide solution. The diameter of the nanowires is ~25 nm and the average spacing between the nanowires is ~50 nm, when measured from center to center of adjacent nanowires. As with the CoPt nanowires discussed in the previous section, the

height of the nanowires is dependent on the time and other electrodeposition parameters. Here, the electrochemical deposition for the Ni/CoPt nanowires shown in Figure 4.16 took, in total, only about one minute to reach a length of ~100 nm with individual deposition times of 20 seconds to form ~80 nm of Ni and 120 seconds to form ~20 nm of CoPt. The Ni/CoPt nanowires have a desirably small aspect ratio (length : diameter) of approximately 4:1.

4.3.2.2 Microstructure and composition of Ni/CoPt nanowires

The composite Ni/CoPt nanowires were fabricated using two electrodeposition steps. First the Ni segments of the nanowires were deposited and the sample was thoroughly rinsed and then soaked in deionized water to remove any traces of Ni electrolyte solution. Following this, the CoPt segment was deposited and then the sample was rinsed and soaked again in deionized water prior to the supercritical drying technique outlined in section 3.5. The relative length of the nanowire segments was determined by SEM analysis after each electrodeposition step to within a margin of error of ±10 nm when taking into account variations in the uniformity of the nanowire heights. The composition of the CoPt segments was measured using EDS analysis in the same manner that was described in the previous section on the CoPt nanowires and ranged from $Co_{60}Pt_{40}$ to $Co_{40}Pt_{60}$, which is within the typical composition range of the $L1_0$ CoPt phase. An annealing treatment was necessary to convert the as-deposited CoPt to the ordered $L1_0$ phase and was also performed the same way as previously described.

4.3.2.3 Magnetic data for Ni/CoPt nanowires

To see the influence of the two-layer composite structure on the magnetic properties, separate samples with Ni and CoPt nanowires of the same height as the Ni/CoPt samples were prepared and annealed using identical conditions. The as-deposited CoPt and Ni/CoPt nanowires exhibit low coercivity due to the lack of $L1_0$ phase CoPt. The ordered $L1_0$ phase was formed during annealing and subsequent increases in the coercivities were obtained. M-H hysteresis loops measured along the nanowire axis, perpendicular to the substrate, are presented in Figure 4.17.

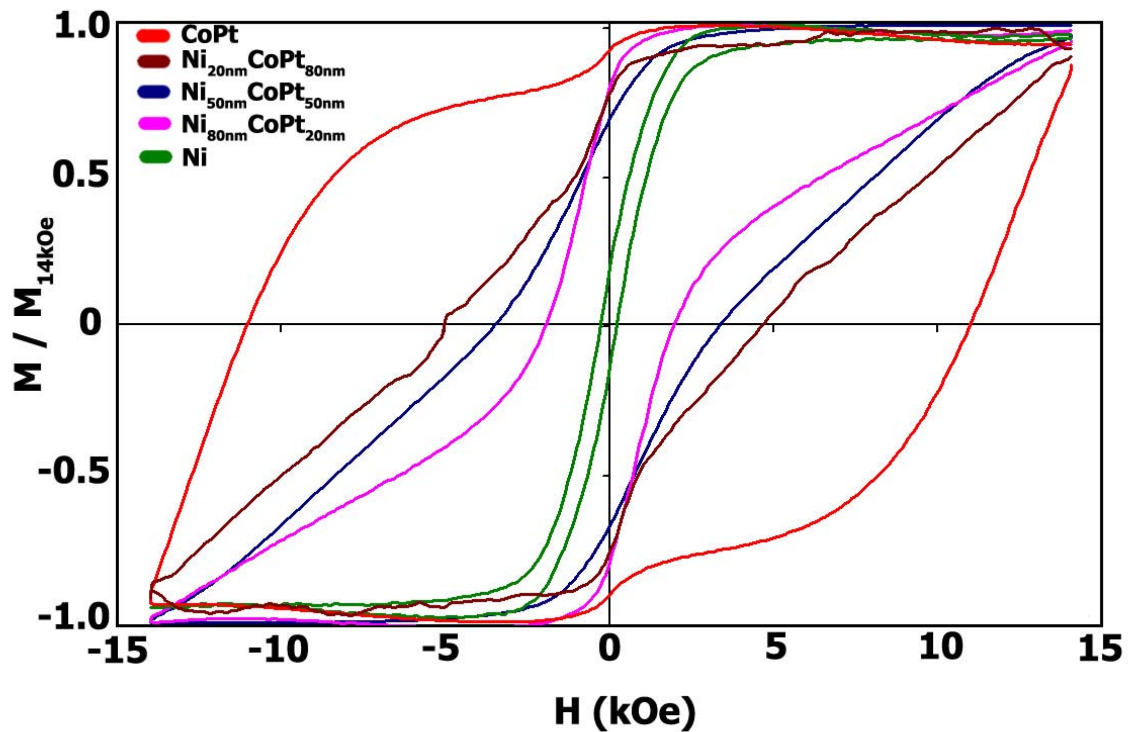

Figure 4.17: M-H hysteresis loops measured in the perpendicular direction along the nanowire axis for the annealed CoPt, Ni_{20nm} / $CoPt_{80nm}$, Ni_{50nm} / $CoPt_{50nm}$, Ni_{80nm} / $CoPt_{20nm}$, and Ni nanowires, all with equivalent lengths of ~100 nm.[155]

The figure shows the comparative data for the Ni nanowires only (100 nm tall), CoPt nanowires only (100 nm tall), and three different 100 nm tall Ni/CoPt composite nanowires, consisting of ~80 nm Ni and ~20 nm CoPt (Ni_{80nm} / $CoPt_{20nm}$), ~50 nm Ni and ~50 nm CoPt (Ni_{50nm} / $CoPt_{50nm}$), and ~20 nm Ni and ~80 nm CoPt (Ni_{20nm} / $CoPt_{80nm}$). The M-H loops for all the samples were measured after the annealing treatment. The Ni nanowires exhibit relatively soft magnetic coercivity of 240 Oe, while the CoPt nanowires show a very high coercivity of at least 10.97 kOe. The real coercivity of the CoPt nanowires is likely to be much higher as the nanowires were not saturated with the maximum applied field of 14 kOe that our AGM is capable of applying. This is also true for the coercivity of the Ni_{20nm} / $CoPt_{80nm}$ nanowires. The two-layer Ni/CoPt nanowires all exhibit intermediate coercivities between those of the CoPt and Ni nanowires of 5.13 kOe for the Ni_{20nm} / $CoPt_{80nm}$, 3.59 kOe for the Ni_{50nm} / $CoPt_{50nm}$, and 1.96 kOe for the Ni_{80nm} / $CoPt_{20nm}$.

Compared to the data shown for the CoPt nanowires presented in the previous section, the composite nanowires do show different magnetic behavior in the in-plane and perpendicular directions. Figure 4.18 shows the M-H loops for the three different compositions of composite nanowires measured in the in-plane and perpendicular directions.

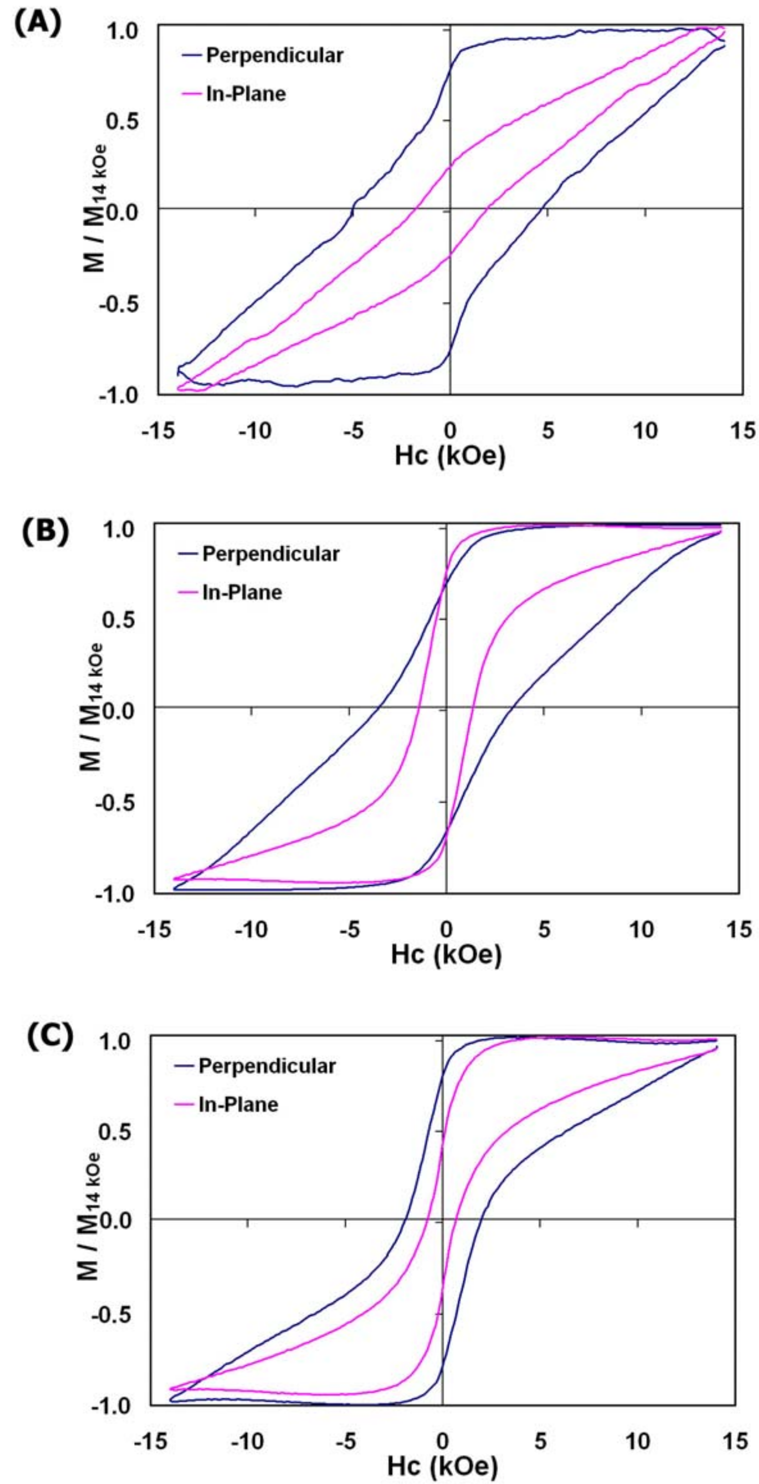

Figure 4.18: M-H loops showing the magnetic properties of the annealed composite Ni/CoPt nanowires measured in the in-plane and perpendicular directions for the Ni_{20nm} / $CoPt_{80nm}$ (A), Ni_{50nm} / $CoPt_{50nm}$ (B), and Ni_{80nm} / $CoPt_{20nm}$ (C) samples.[155]

The coercivity for the Ni_{80nm} / $CoPt_{20nm}$ nanowires in the perpendicular direction is significantly higher than in the in-plane direction, 1.96 kOe versus 730 Oe. This probably indicates the influence of shape anisotropy and perhaps some perpendicular anisotropy due to the texture and orientation of the nanowires. By increasing the ratio of CoPt to Ni, the coercivity can be increased as the M-H loops show for the varying compositions. The measured coercivities for the Ni_{50nm} / $CoPt_{50nm}$ sample were 3.59 kOe in the perpendicular direction and 1.38 kOe in-plane and the Ni_{20nm} / $CoPt_{80nm}$ sample were 5.10 kOe perpendicular and 1.92 kOe in-plane. A summary of the coercivities for the different nanowire compositions is presented in Table 4.2.

Table 4.2: Data table summarizing the coercivities measured in the perpendicular and in-plane directions for the different nanowire compositions.

Composition	**Coercivity (kOe)**	
	Perpendicular	**In-Plane**
CoPt	10.97	9.79
Ni_{20nm} / $CoPt_{80nm}$	5.10	1.92
Ni_{50nm} / $CoPt_{50nm}$	3.59	1.38
Ni_{80nm} / $CoPt_{20nm}$	1.95	0.73
Ni	0.24	0.16

The shape of the M-H loops for the composite nanowires gradually shifts as the composition changes. Figure 4.17 shows the broadening out of the M-H loops and the increase in coercivity as the amount of CoPt relative to the amount of Ni increases. The influence of the soft Ni layer can be seen in how the M-H loop is still constrained in the midsection and has a tall and thinner shape compared with that of the pure CoPt, which

shows a tall and wide M-H, loop shape. As the amount of Ni decreases, its influence on the magnetic properties can be seen especially in the in-plane measurement of the Ni_{20nm} / $CoPt_{80nm}$ sample where the M-H loop looks considerably different from the other in-plane M-H loops with larger relative amounts of Ni.

The data indicates a trend that the presence of the soft magnetic bottom layer reduces the field required to reverse the CoPt nanowire segments on top. Because the M-H loop for the Ni/CoPt nanowires contains the magnetization switching of both the CoPt and the Ni, it is not easy to separate the individual component M-H loops. Attempts to separate the M-H loop into its Ni and CoPt components reveal that the coercivity of the CoPt recording layer decreases while the coercivity of the Ni underlayer increases. This indicates magnetic coupling between the two layers and demonstrates the overall reduction in the coercivity achieved with the Ni/CoPt composite nanowire structure.

In reports published by Dobin and Richter, theoretical calculations and micromagnetic modeling were performed on thin film composite media systems.[156, 157] The authors devised a generalized equation for calculating the switching field, H_{SW}, needed to switch the composite structure:

$$H_{SW} = \frac{H_{HARD} - \gamma \cdot H_{SOFT}}{\left(1+\sqrt{\gamma}\right)^2} \quad , \quad \gamma \equiv \frac{M_{SOFT} \cdot A_{SOFT}}{M_{HARD} \cdot A_{HARD}} \ .$$ [156]

Here, M_{soft} and M_{hard} are the saturation magnetizations of the soft and hard layers, A_{soft} and A_{hard} are the anisotropy fields of the soft and hard layers, and γ represents the ratio of the domain wall energies of the soft and hard layers.[156] This formula was derived for thin films with the same thicknesses of hard and soft materials and does not cover

nanowire type structures. Recently, mathematical modeling and theoretical calculations were performed by Loxley and Stamps on a proposed hard/soft magnetic two-layer nanowire structure to estimate the magnetic reversal properties.[158] The mathematical calculations in that work are based on smaller diameter, d ≤ ~10 nm, half hard magnet and half soft magnet nanowires of infinite length. The small diameters allow them to be considered as one-dimensional single magnetic domain structures and the infinite length negates any edge effects. An important result from this analysis was that if the anisotropy constant of the hard magnetic material is much greater than that of the soft magnetic material, $K_{HARD} >> K_{SOFT}$, then the magnetic field required for reversal is:

$$H_{SW} \cong \frac{K_{HARD}}{2\mu_O M_S} ,$$

corresponding to a switching field 25% of that required for reversal of an uncoupled hard layer.[158] This approximation is relevant in our Ni/CoPt structure, as the anisotropy constants, K, of Ni and CoPt are ~5.0×10^4 erg / cm^3 and ~4.5×10^7 erg / cm^3, respectively.[159, 160] Although, this equation relates only to one-dimensional analysis and does not consider any variation in the relative amounts of hard and soft material. The presence of larger multiple magnetic domains in the nanowires fabricated in this research work will certainly affect the magnetic switching behavior. However, the perpendicular coercivity of the Ni_{50nm} / $CoPt_{50nm}$ nanowires was measured at 3.60 kOe which is about 33% of the coercivity of the pure CoPt nanowires. This amount of reduction in coercivity agrees fairly well with the predicted reduction to 25% as proposed by Loxley and Stamps.[158] Considering that the coercivity of the fabricated CoPt nanowires was measured at 10.97 kOe and is likely to be higher since the M-H

loop is not saturated, the reduction in coercivity should therefore be larger, and the agreement seems quite good. As of yet, there has been no theoretical treatment of either larger diameter nanowires dealt with as three-dimensional structures or nanowires with varying amounts of hard and soft material. Regardless, the experimental data for the other Ni/CoPt composite nanowire samples demonstrates the general trend in the reduction of the coercivity. With four times more Ni than CoPt the measured coercivity of 1.95 kOe for the Ni_{80nm} / $CoPt_{20nm}$ nanowires is 18% of the value for the CoPt nanowires. For the Ni_{20nm} / $CoPt_{80nm}$ nanowires and with four times more CoPt than Ni, the measured coercivity is 46% of the coercivity of the CoPt nanowires. The latter result shows the benefit of a relatively thin layer of soft magnetic material in reducing the effective coercivity. Such reductions in the measured coercivity are among the potential benefits of hard/soft exchange coupling in a hard/soft two-layer nanowire structure.

In fact, exchange coupling may not be the only factor responsible for the observed reduction in coercivity. The Ni nanowire segments may serve as magnetic field-concentrating poles, effectively increasing the applied field on the CoPt portion of the composite nanowires. Another possible explanation for the reductions in coercivity is interdiffusion during annealing between the Ni and CoPt segments that could result in the formation of a ternary $L1_0$ alloy of Co-Pt-Ni. Although, this explanation seems unlikely because significant interdiffusion would be reflected by a third magnetization behavior in the M-H loops shown previously. However, no such effect is observed in the data, but it is likely that minor diffusion between the hard and soft layers does occur

around the interface region due to the high temperatures reached in the annealing process.

4.4 Nanoimprint lithography using an AAO based master

Using the regularity of AAO templates it is possible to create an imprinting master stamp as a means to replicate the pore array. Some background material on imprinting technology was presented previously in section 2.3.3. Imprinting with an ideally ordered master stamp can be used to pre-pattern the aluminum surface yielding a very regular pore array. The master stamps are typically made using a costly and time-consuming serial electron beam lithography process, making them very valuable. The nature of the imprinting process makes them vulnerable to mechanical damage and degradation while repeated use only increases the likelihood of this happening. Because of this, it is desirable to minimize the use of the master stamp by replicating it and creating what is known as a daughter stamp.[161] Typically, this is done by using the master stamp to imprint a polymer or photoresist layer and then using the imprinted material as a means to replicate the shape of the master stamp.[162, 163, 164] For this research work, a technique has been developed using the anodization characteristics of Al and electrodeposition to replicate a master stamp pattern and produce a daughter stamp.

While the full application of this process to replicate a master imprinting stamp pattern obviously requires a master imprinting stamp, it is still possible to demonstrate the technique without one. For clarity, Figure 4.19 shows a schematic diagram of the

process steps used to replicate a master stamp, which is described in further detail below.

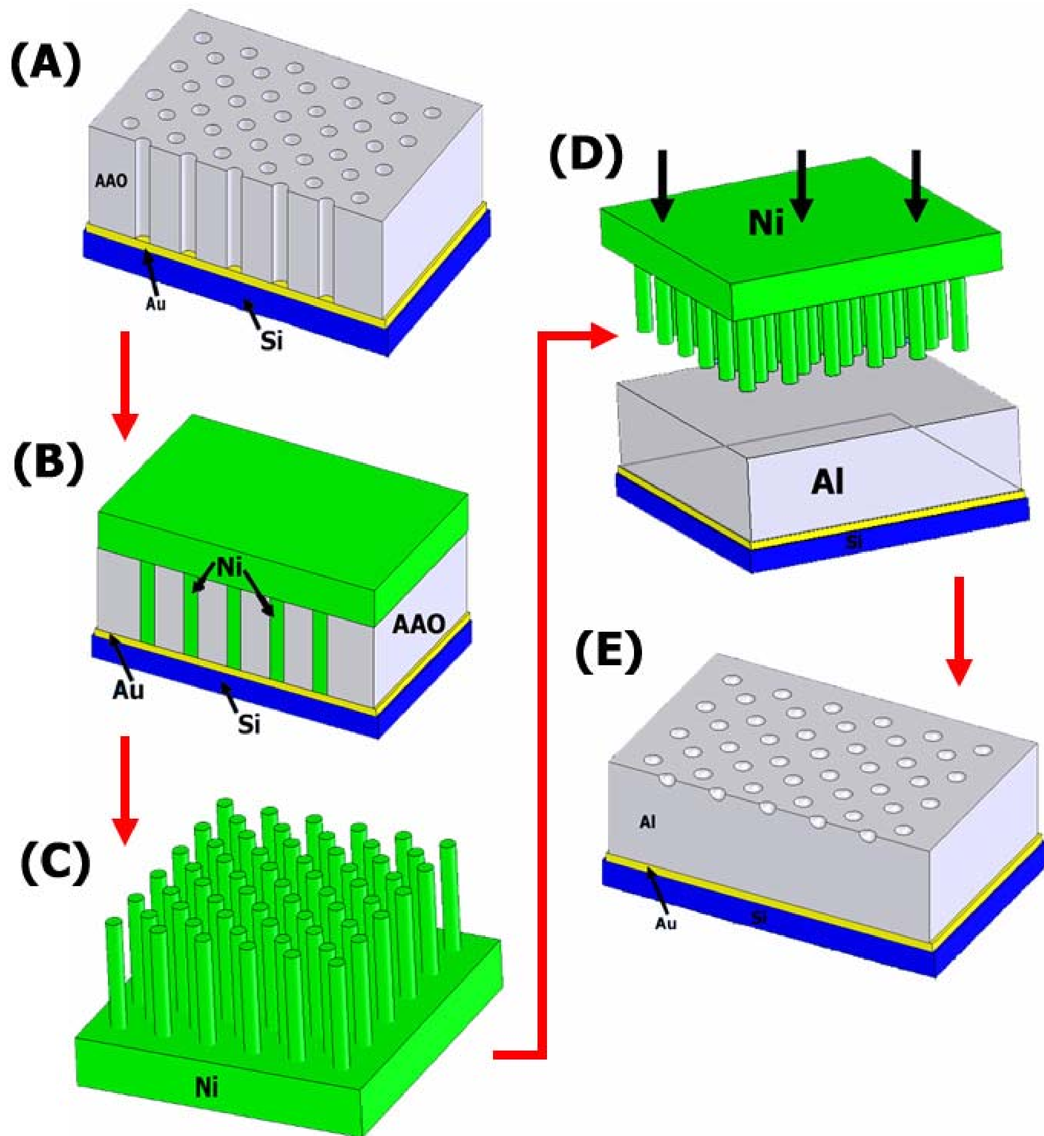

Figure 4.19: Schematic diagram showing the process steps in the replication of an imprinting master stamp: (A) an ideally ordered pore structure prepared from anodizing an Al film imprinted by the master stamp, (B) electrodeposition of nanowires into the pores and onto the surface of the AAO template, (C) chemical dissolution of the Si substrate and AAO template leaving only the nanowires, (D) imprinting of an Al film using the prepared nanowire array, and (E) an imprinted film with ordered surface depressions, ready to repeat the process.

In the full process, the master stamp would first be used to imprint the surface of an aluminum film on a silicon substrate, pre-patterning the surface and yielding an ideally ordered pore array after anodization. In the absence of the master stamp, the Al film is anodized without imprinting, resulting in a more randomly ordered pore array on the surface, with better regularity at the pore base. After this, an electrodeposition step is performed and nanowires are deposited into the pores and allowed to grow out over the top of the AAO template to form a metal film. For the demonstration of the principle, Ni nanowires were used, although it is possible to use other metals and alloys to possibly obtain a more rigid imprinting stamp. The electrodeposition was carried out over a long time, in some cases being left overnight, to build up a very thick Ni film. To provide added structural support and serve as a handle, a piece of quartz was affixed to the top side of the thick Ni film using epoxy. Although the thick Ni film was strong enough to be manipulated on its own, the quartz backing plate allowed for easier manipulation. The sample was then immersed in a solution of 40 weight % potassium hydroxide (KOH) at 60°C, an optimal condition for dissolving Si.[165] Dissolution of the entire Si substrate generally took about six hours, and the basic KOH solution also dissolved the AAO template at the same time without reacting with the Ni nanowires and film. The freestanding Ni nanowire array that resulted was still covered by the thin Au underlayer, which was etched away using a commercially available Au etching solution to expose the Ni nanowires. The fabricated structure exhibits nanowires of identical height due to the flat and smooth Si substrate that was used as the base

material. Figure 4.20 shows some top view and cross-sectional SEM images of the freestanding Ni nanowire arrays that were fabricated.

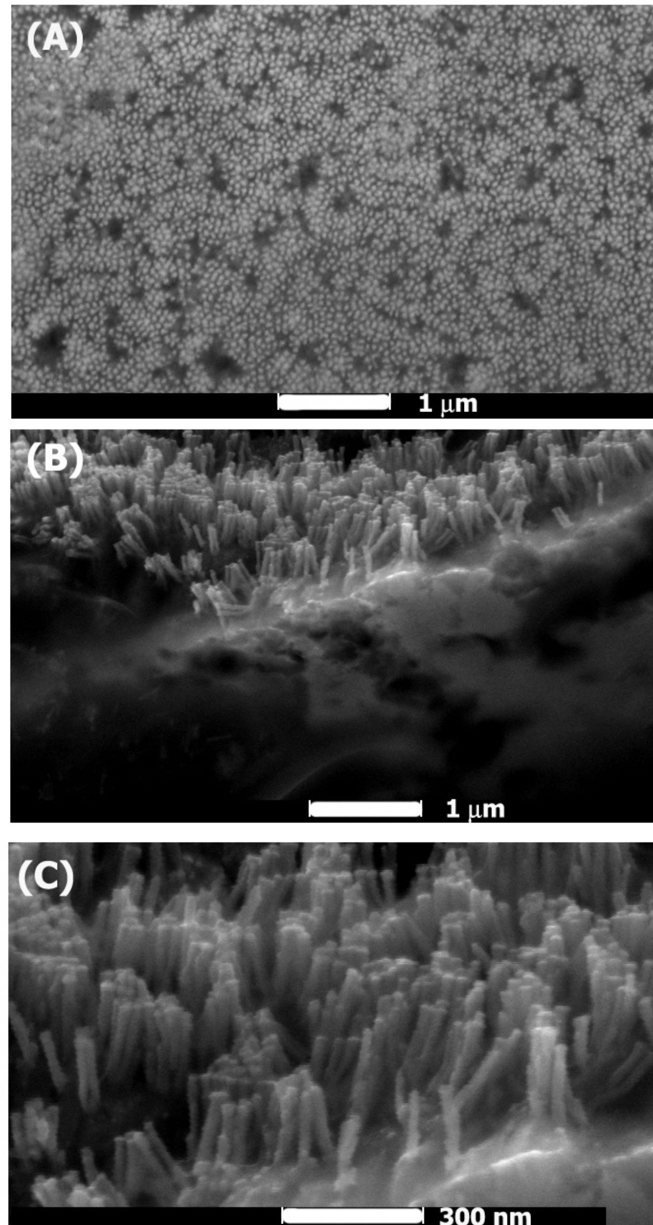

Figure 4.20: SEM images of the freestanding Ni nanowire arrays produced using the procedure described in the text, (A) top view of the nanowire bases that were attached to the Si substrate, (B) cross-sectional lower magnification image of a sectioned Ni film and nanowire array with the film crumpled during sectioning, and (C) higher magnification cross-sectional image, again crumpled during sectioning.

The top view SEM image shown in Figure 4.19 (A) looks quite similar to top view images of nanowires prepared in the AAO pores as shown in Figure 4.10 (D). This is to be expected as they are embedded in similar pore structures and are electrodeposited in the same way. The Ni nanowires here exhibit a vertical structure the same as the CoPt nanowires shown in Figure 4.10. In mechanically sectioning the thick Ni film and nanowires to produce a suitable edge for cross-sectional SEM images it was not possible to maintain the structural integrity of the sample. As a result, some bending and crumpling of the thick film occurred resulting in the distorted surface topography shown in Figure 4.20 (B) and (C).

Because no imprinting master stamp was used to produce an ordered pore array the resulting Ni stamp with randomly arranged Ni nanowires has limited utility. However, this simplified technique for replicating a master stamp would certainly be an economical and practical method for creating daughter stamps without degrading the master stamp. Hopefully the opportunity to use this technique will arise in future research efforts and it will prove useful and beneficial.

CHAPTER 5: SUMMARY, CONCLUSIONS, AND FUTURE WORK

In summary, it was shown how magnetic nanowires and composite nanowires can be deposited within the pores of anodized aluminum oxide templates. Perpendicular coercivities up to 10.97 kOe were obtained for 25 nm diameter, 100 nm tall CoPt nanowires. The high coercivity of the CoPt nanowires can effectively be reduced to a desirable level by creating a composite structure blending an underlying soft magnetic material such as Ni with a top layer of a hard magnetic material like CoPt. The fabricated Ni/CoPt nanowires exhibited intermediate coercivities between those of their Ni and CoPt constituents. Three different compositions of 25 nm diameter and ~100 nm tall composite nanowires were produced, Ni_{20nm} / $CoPt_{80nm}$, Ni_{50nm} / $CoPt_{50nm}$, and Ni_{80nm} / $CoPt_{20nm}$. The measured perpendicular coercivities for these were 5.10 kOe, 3.59 kOe, and 1.95 kOe, respectively. The data shows how the relative amounts of Ni and CoPt influence the measured coercivity and magnetic switching behavior of the nanowires. Additionally, a technique using the characteristics of anodized aluminum oxide and an electrodeposition step to replicate a master imprinting stamp for nanoimprinting was demonstrated.

The goal of this work was to produce a structure using the anodized aluminum membranes that could potentially be used in magnetic data storage applications as a patterned media device. While we were able to fabricate a porous structure with magnetic nanowires with some desirable properties, there are still many challenges to overcome before a structure such as this could be used in a data storage device.

One of the most critical challenges, and perhaps the biggest hurdle, is creating an extremely ordered pore structure over a large area on the order of several square centimeters. For a recording density of 1 Tbit / in^2 the pores would need to be ~12.5 nm with an interpore spacing of 25 nm. At these distances, even a small variation in the positioning of the pores such as 1-2 nm would be an error of almost 5-10%. The ability to accurately locate an individual pore is necessary in any data storage device and with even a small positioning difference like this leading to a significant error, numerous errors in writing and accessing information might result. In the event that the position of one pore might influence that of its neighbors, any error could be catastrophic since with such a large number of pores this type of cumulative error would quickly move the pores way out of alignment, rendering the device useless. At the moment, much research has centered on nanoimprinting as a means to solve this problem. Using electron beam lithography it may soon be possible to make a functional imprinting master stamp with feature sizes around 10 nm. However, when working with a serial process like electron beam lithography the primary concern is the time required to define all of the features. When considering the vast number of features on something even the size of a square inch, it might take months of electron beam lithography to pattern that area. As of now though, this seems to be the best alternative as there are few, if any, available methods of fabricating features of this small size with such uniformity and precision over a large area. The necessary nanoimprinting technology is already available and perhaps with future research work into the electron beam lithography process, fabricating a near perfectly ordered large-area imprinting master may soon become a reality. If this does occur, large scale ordered anodized aluminum

templates would become an economical and viable matrix material for a patterned media device.

Another challenge in moving towards an AAO based data storage device is the surface roughness of the anodized aluminum membrane. With the magnetic recording head needing to move across the surface at such small separation distances, on the order of a few nanometers, an extremely smooth surface with an RMS roughness of ~5 Å is necessary. With proper polishing equipment and the correct chemical mechanical polishing techniques and parameters this should be achievable, although with such a composite structure as this there would be concerns of preferential material removal leading to non-uniformities over the larger surface areas needed for a device.

The third main issue is the uniformity of the magnetic properties of the nanowires. The possibility exists that there may be some variation in the magnetic properties of the nanowires. Obviously such fluctuations would need to be minimized in a data storage device because if the coercivity of one nanowire were much higher than the average, the magnetic field applied by the magnetic recording head might not be strong enough to write or erase the data. Statistically speaking, there should be a very small standard deviation for the values of the coercivity. As of now, there is not really a good method of measuring the coercivity of a nanoscale feature with the size of a single nanowire. While magnetic force microscopy (MFM) may be able to provide some magnetic data, it is still challenging to attain the characteristics of such small features without influencing the neighboring regions. Even with refinements, MFM would still prove to be a very time-consuming way to analyze large sections of a device. Lacking such a necessary measurement method, the magnetic properties could be

inferred by comparing the structure of many nanowires through transmission electron microscopy, assuming that similarities in structure would translate to similarities in magnetic properties. Even if such a comparison were accurate, it would be incredibly time consuming to analyze a statistically relevant number of nanowires with a TEM.

It is also necessary to determine the optimum coercivity for the most efficient device operation. Further work in this area should center around selecting the right materials to either alloy together or by combining different materials to form a composite structure as shown here with the Ni/CoPt nanowires. Proper materials selection along with fine tuning of the electrodeposition and post-processing conditions should lead to a material with ideal properties.

Despite these main roadblocks that exist, the primary foundation of research already completed indicates that there is tremendous potential for anodized aluminum oxide templates in the field of magnetic recording technology. The central question that arises is whether or not a competing patterned media method or even an alternative storage technology will come to fruition before these problems can be solved. With other storage option such as holographic data storage being studied there is some competition. However, many of the requirements that the hard disk industry is looking to fulfill could be met by using anodized aluminum oxide templates. With advantages such as potentially high throughput, ease of production, low cost materials, and the flexibility in terms of substrate size, pore size, and pore spacing; it is clear to see why there has already been such a prodigious amount of funded research in this field.

Hopefully, the research accomplished as part of this project will open some new avenues for advancement in this field. The ability to synthesize hard and soft magnetic

composite materials could be very advantageous in many applications and could prove to be a central point in facilitating easier magnetic switching in the high coercivity materials needed to overcome the superparamagnetic limit that has currently derailed longitudinal recording technology.

As the world's population continues to expand and everyday life moves further into the digital world, we will continue to amass more and more data, in the form of pictures, music, e-mails, or documents. In conjunction with this are people's desires for small size and easy portability, evidenced by the explosion in, PDAs, cell phones, and MP3 players. Unless new storage methods can be implemented, we will soon reach a maximum in the amount of information that these little devices can store. It would certainly be very beneficial if new technology such as patterned recording media can be developed to prevent this from happening. In the event that this does happen, it will be a great accomplishment to have worked and contributed to such an important technological advancement.

REFERENCES

1. History of Aluminum. http://www.historyofaluminum.com.

2. William F. Smith, *Structure and Properties of Engineering Alloys*, McGraw-Hill, New York, 1993.

3. Mineral Information Institute. http://www.mii.org/Minerals/photoal.html.

4. R. M. Howe and R. F. Ferguson, *J. Am. Cer. Soc.*, **6**, 3 (1922).

5. C. M. Hall, *Process of Reducing Aluminum from its Fluoride Salts by Electrolysis*, US Patent No. 400,664 (1889).

6. J. D. Edwards, F. C. Frary and Z. Jeffries, *Aluminum and its Production*, McGraw-Hill, New York (1930).

7. J. C. Kotz and P. Treichel, *Chemistry and Chemical Reactivity*, Harcourt Brace, Fort Worth (1996).

8. K. Grjotheim and H. Kvande, *Understanding the Hall-Heroult process for production of aluminium*, Aluminium-Verlag, Dusseldorf (1986).

9. United States Geological Survey. http://minerals.usgs.gov/minerals/pubs/commodity/aluminum/.

10. K. R. Van Horn, *Aluminum Vol I. Properties, Physical Metallurgy and Phase Diagrams*, American Society for Metals, Metals Park (1967).

11. M. E. Straumanis and T. Ejima, *Z Physik Chem.*, **23**, 440 (1960).

12. H. J. Axon and W. H. Rothery, *Proc. Roy. Soc.*, **A193**, 1 (1948).

13. J. E. Hatch, *Aluminum Properties and Physical Metallurgy*, American Society for Metals, Metals Park (1984).

14. W. H. Gitzen, *Alumina as a Ceramic Material*, The American Ceramic Society, Columbus (1970).

15. E. Dörre and H. Hübner, *Alumina*, Springer-Verlag, Berlin (1984).

16. R. S. Alwitt, *The Electrochemistry Encyclopedia: Anodizing*, http://electrochem.cwru.edu/ed/encycl/art-a02-anodizing.htm, (2002).

17. M. S. Hunter and P. E. Fowle, *J. Electrochem. Soc.*, **101**, 481 (1954).

18. G. E. Thompson and G. C. Wood, *Treatise on Materials Science and Technology*, Academic, New York, 1983.

19. I. A. Ammar, S. Darwish, and P. Khalil, *Z. Werkstofftechn.* **12**, 421 (1981).

20. R.C. Furneaux, G.E. Thompson, and G.C. Wood, *Corrosion Science*, **18**, 853 (1978).

21. W. A. Badawy, M. M. Ibrahim, M. M. Abon-Romia, and M. S. El-Basionny, *Corrosion*, **42**, 324 (1986).

22. H. Asoh, K. Nishio, M. Nakao, T. Tamamura, and H. Masuda, *J. Electrochem. Soc.*, **148**, B152 (2001).

23. J. D. Edwards and F. Keller, *Trans. Electrochem. Soc.*, **79**, 135 (1941).

24. J. D. Edwards and F. Keller, *Trans. Am. Inst. Mining Met. Engrs.*, **156**, 288 (1944).

25. F. Keller, M. S. Hunter, and D. L. Robinson, *J. Electrochem. Soc.*, **100**, 411 (1953).

26. M. S. Hunter and P. Fowle, *J. Electrochem. Soc.*, **101**, 514 (1954).

27. R. B. Mason, *J. Electrochem. Soc.*, **102**, 671 (1955).

28. G. C. Wood, J. P. O'Sullivan, and B. Vaszko, *J. Electrochem. Soc.*, **115**, 618 (1968).

29. G. C. Wood and J. P. O'Sullivan, *J. Electrochem. Soc.*, **116**, 1351 (1969).

30. J. P. O'Sullivan and G. C. Wood, *Proc. R. Soc. London*, **A317**, 511 (1970).

31. A. Despić and V. P. Parkhutik, *Modern Aspects of Electrochemistry*, **20**, 401 (1989).

32. T. P. Hoar and N. F. Mott, *J. Phys. Chem. Solids*, **9**, 97 (1959).

33. J. Choi, R. B. Wehrspohn, and U. Gösele, *Electrochem. Acta*, **50**, 2591 (2005).

34. G. E. Thompson, R. C. Furneaux, G. C. Wood, J. A. Richardson, and J. S. Goode, *Nature*, **272**, 433 (1978).

35. V. P. Parkhutik and V. I. Shershulsky, *J. Phys. D: Appl. Phys.*, **25**, 1258 (1992).

36. K. Shimizu, G. E. Thompson, G. C. Wood, K. Kobayashi, *Phil. Mag. Lett.*, **61**, 133 (1990).

37. A. P. Li, F. Müller, A. Birner, K. Nielsch, and U. Gösele, *J. Appl. Phys.*, **84**, 6023 (1998).

38. K. Ebihara, H. Takahashi, and M. Nagayama, *J. Met. Finish. Soc. Jpn.*, **34**, 548 (1983).

39. C. R. Martin, *Science*, **266**, 1961 (1994).

40. H. Masuda, H. Tanaka, and N. Baba, *Chem. Lett.*, **19**, 621 (1990).

41. C. R. Martin, *Chem. Mater.*, **8**, 1739 (1996).

42. K. Ebihara, H. Takahashi, and M. Nagayama, *J. Met. Finish. Soc. Jpn.*, **33**, 4 (1982).

43. H. Masuda, F. Hasegwa, and S. Ono, *J. Electrochem. Soc.*, **144**, L127 (1997).

44. H. Masuda and K. Fukuda, *Science*, **268**, 1466 (1995).

45. S. Ono, M. Saito, and H. Asoh, *Electrochim. Acta*, **51**, 827 (2005).

46. Z. Chen and H. Zhang, *J. Electrochem. Soc.*, **152**, D227 (2005).

47. O. Jessensky, F. Müller, U. Gösele, *Appl. Phys. Lett.*, **72**, 1173 (1998).

48. K. Nielsch, J. Choi, K. Schwirn, R. B. Wehrspohn, and U. Gösele, *Nano Letters*, **2**, 677 (2002).

49. S. Ono, M. Saito, and H. Asoh, *Electrochem. Sol. St. Lett.*, **7**, B21 (2004).

50. S. Ono, M. Saito, M. Ishiguro, and H. Asoh, *J. Electrochem. Soc.*, **151**, B473 (2004).

51. Y. Lei, W. Cai, and G. Wilde, *Prog. Mater. Sci.*, **52**, 465 (2007).

52. V. V. Konovalov, R. M. Metzger, G. Zangari, *Proc. Electrochem. Soc.*, **99**, 203 (2000).

53. F. Li, L. Zhang, and R. M. Metzger, *Chem. Mater.*, **10**, 2470 (1998).

54. H. Masuda, K. Nishio, and N. Baba, *Jpn. J. Appl. Phys.*, **31**, L1775 (1992).

55. H. Masuda, K. Nishio, and N. Baba, *Thin Solid Films*, **223**, 1 (1993).

56. H. Masuda, T. Mizuno, N. Baba, and T. Ohmori, *J. Electroanal. Chem.*, **368**, 333 (1994).

57. O. Jessensky, F. Müller, and U. Gösele, *J. Electrochem. Soc.*, **145**, 3735 (1998).

58. S. Bandyopadhyay, A. E. Miller, H. C. Chang, G. Banerjee, V. Yuzhakov, D. F. Yue, R. E. Ricker, S. Jones, J. A. Eastman, E. Baugher, and M. Chandrasekhar, *Nanotechnology*, **7**, 360 (1996).

59. H. Masuda and M. Satoh, *Jpn. J. Appl. Phys.*, **35**, L126 (1996).

60. H. Masuda, H. Yamada, M. Satoh, H. Asoh, M. Nakao, and T. Tamamura, *Appl. Phys. Lett.*, **71**, 2770 (1997).

61. K. Yasui, K. Nishio, H. Nunokawa, and H. Masuda, *J. Vac. Sci. Technol.*, **23**, L9 (2005).

62. J. Choi, R. B. Wehrspohn, and U. Gösele, *Adv. Mater.*, **15**, 1531 (2003).

63. H. Masuda, H. Asoh, M. Watanabe, K. Nishio, M. Nakao, and T. Tamamura, *Adv. Mater.*, **13**, 189 (2001).

64. A. P. Li, F. Müller, and U. Gösele, *Electrochem. Sol. State Lett.*, **3**, 131 (2000).

65. Y. Matsui, K. Nishio, and H. Masuda, *Japn. J. Appl. Phys.*, **44**, 7726 (2005).

66. Y. Matsui, K. Nishio, and H. Masuda, *Small*, **2**, 522 (2006).

67. S. Shingubara, Y. Murakami, K. Morimoto, and T. Takahagi, *Surf. Sci.*, **532**, 317 (2003).

68. H. Masuda, M. Yotsuya, M. Asano, K. Nishio, M. Nakao, A. Yokoo, and T. Tamamura, *Appl. Phys. Lett.*, **78**, 826 (2001).

69. H. Masuda, A. Abe, M. Nakao, A. Yokoo, T. Tamamura, and K. Nishio, *Adv. Mater.*, **15**, 161 (2003).

70. J. Choi, K. Nielsch, M. Reiche, R. B. Wehrspohn, and U. Gösele, *J. Vac. Sci. Technol. B*, **21**, 763 (2003).

71. D. Crouse, Y. H. Lo, A. E. Miller, and M. Crouse, *Appl. Phys. Lett.*, **76**, 49 (2000).

72. Y. Kimura, H. Shiraki, K. Ishibashi, H. Ishii, K. Itaya, and M. Niwano, *J. Electrochem. Soc.*, **153**, C296 (2006).

73. M. Schlesinger and M. Paunovic, *Modern Electroplating*, Wiley, New York (2000).

74. M. Schlesinger, *The Electrochemistry Encyclopedia: Electroplating*, http://electrochem.cwru.edu/ed/encycl/art-e01-electroplat.htm, (2002).

75. G. Sauer, G. Brehm, S. Schneider, K. Nielsch, R. B. Wehrspohn, J. Choi, H. Hofmeister, and U. Gösele, *J. Appl. Phys.*, **91**, 3243 (2002).

76. K. Nielsch, F. Müller, A. P. Li, and U. Gösele, *Adv. Mater.*, **12**, 582 (2000).

77. J. Choi, G. Sauer, K. Nielsch, R. B. Wehrspohn, and U. Gösele, *Chem. Mater.*, **15**, 776 (2003).

78. H. Pan, B. Liu, J. Yi, C. Poh, S. Lim, J. Ding, Y. Feng, C. H. A. Huan, and J. Lin, *J. Phys. Chem. B*, **109**, 3094 (2005).

79. O. Rabin, P. R. Herz, Y. M. Lin, A. I. Akinwande, S. B. Cronin, and M. S. Dresselhaus, *Adv. Funct. Mater.*, **13**, 631 (2003).

80. M. Tian, S. Xu, J. Wang, N. Kumar, E. Wertz, Q. Li, P. M. Campbell, M. H. W. Chan, and T. E. Mallouk, *Nano Lett.*, **5**, 697 (2005).

81. C. L. Xu, H. Li, T. Xue, and H. L. Li, *Scripta Mater.*, **54**, 1605 (2006).

82. K. Yasui, T. Morikawa, K. Nishio, and H. Masuda, *Jap. J. Appl. Phys.*, **44**, L469 (2005).

83. H. Zeng, M. Zheng, R. Skomaski, D. J. Sellmyer, Y. Liu, L. Menon, and S. Bandyopadhyay, *J. Appl. Phys.*, **87**, 4718 (2000).

84. S. Kato, H. Kitazawa, and G. Kido, *J. Mag. Mag. Mat.*, **272**, 1666 (2004).

85. D. Almawlawi, N. Coombs, and M. Moskovits, *J. Appl. Phys.*, **70**, 4421 (1991).

86. Y. Peng, H. L. Zhang, S. L. Pan, and H. L. Li, *J. Appl. Phys.*, **87**, 7405 (2000).

87. K. Kim, M. Kim, and S. M. Cho, *Mat. Chem. Phys.*, **96**, 278 (2006).

88. M. J. Zheng, L. D. Zhang, G. H. Li, X. Y. Zhang, and X. F. Wang, *Appl. Phys. Lett.*, **79**, 839 (2001).

89. Y. Yang, H. Chen, Y. Mei, J. Chen, X. Wu, and X. Bao, *Solid St. Comm.*, **123**, 279 (2002).

90. D. Xu, Y. Xu, D. Chen, G. Guo, L. Gui, and Y. Tang, *Chem. Phys. Lett.*, **325**, 340 (2000).

91. D. Xu, Y. Xu, D. Chen, G. Guo, L. Gui, and Y. Tang, *Adv. Mater.*, **12**, 520 (2000).

92. M. S. Sander, A. L. Prieto, R. Gronsky, T. Sands, and A. M. Stacy, *Adv. Mater.*, **14**, 665 (2002).

93. K. Nielsch, R. B. Wehrspohn, J. Barthel, J. Kirschner, U. Gösele, S. F. Fischer, and H. Kronmüller, *Appl. Phys. Lett.*, **79**, 1360 (2001).

94. K. Nielsch, R. B. Wehrspohn, J. Barthel, J. Kirschner, S. F. Fischer, H. Kronmüller, T. Schweinböck, D. Weiss, and U. Gösele, *J. Mag. Mag. Mat.*, **249**, 234 (2002).

95. W. Chen, S. Tang, M. Lu, and Y. Du, *J. Phys: Condens. Mat.*, **15**, 4623 (2003).

96. H. Zhu, S. Yang, G. Ni, D. Yu, and Y. Du, *Scripta Mater.*, **44**, 2291 (2001).

97. G. B. Ji, S. L. Tang, B. X. Gu, and Y. W. Du, *J. Phys. Chem. B*, **108**, 8862 (2004).

98. R. L. Wang, S. L. Tang, B. Nie, X. L. Fei, Y. G. Shi, and Y. W. Du, *Solid St. Comm.*, **142**, 639 (2007).

99. F. Li and L. Ren, *Phys. Stat. Sol.*, **193**, 196 (2002).

100. S. Jeong, Y. Hsu, M McHenry, and D. Laughlin, *J. Appl. Phys.*, **87**, 6143 (2000).

101. A. S. Darling, *Platinum Metal Rev.*, **7**, 96 (1963).

102. F. Bolzoni, F. Leccabue, R. Panizzieri, and L. Pareti, *IEEE Trans. Mag.*, **20**, 1625 (1984).

103. N. Sharma, S. M. Casey, G. A. Jones, and P. J. Grundy, *J. Mag. Mag. Mat.*, **193**, 93 (1999).

104. N. Yasui, A. Imada, and T. Den, *Appl. Phys. Lett.*, **83**, 3347 (2003).

105. J. Mallet, K. Y. Zhang, C. L. Chien, T. S. Eagleton, and P. C. Searson, *Appl. Phys. Lett.*, **84**, 3900 (2004).

106. H. Li, C. L. Xu, G. Y. Zhao, and H. L. Li, *J. Phys. Chem. B*, **109**, 3759 (2005).

107. W. Chen, Z. Li, G. B. Ji, S. L. Tang, M. Lu, and Y. W. Du, *Solid St. Comm.*, **133**, 235 (2005).

108. J. Mallet, K. Y. Zhang, S. M. Tempfli, M. M. Tempfli, and L. Piraux, *J. Phys. D: Appl. Phys.*, **38**, 909 (2005).

109. M. H. Lu, T. Song, T. J. Zhou, J. P. Wang, S. N. Piramanayagam, W. W. Ma, and H. J. Gong, *J. Appl. Phys.*, **95**, 6735 (2004).

110. L. Cagnon, Y. Dahmane, J. Voiron, S. Pairis, M. Bacia, L. Ortega, N. Benbrahim, and A. Kadri, *J. Mag. Mag. Mat.*, **310**, 2428 (2007).

111. Y. Dahmane, L. Cagnon, J. Voiron, S. Pairis, M. Bacia, L. Ortega, N. Benbrahim, and A. Kadri, *J. Phys. D: Appl. Phys.*, **39**, 4523 (2006).

112. M. Alper, *Nanostructured Magnetic Materials and their Applications*, Springer-Verlag, Berlin (2002).

113. Y. G. Guo, L. J. Wan, C. F. Zhu, D. L. Yang, D. M. Chen, and C. L. Bai, *Chem. Mater.*, **15**, 664 (2003).

114. P. P. Nguyen, D. H. Pearson, R. J. Tonucci, and K. J. Babcock, *J. Electrochem. Soc.*, **145**, 247 (1998).

115. S. Dubois, C. Marchal, J. M. Beuken, L. Piraux, J. L. Duvail, A. Fert, J. M. George, and J. L. Maurice, *Appl. Phys. Lett.*, **70**, 396 (1997).

116. X. T. Tang, G. C. Wang, and M. Shima, *Phys. Rev. B*, **75**, 134404 (2007).

117. J. U. Cho, J. H. Min, S. P. Ko, J. Y. Soh, Y. K. Kim, J. H. Wu, and S. H. Choi, *J. Appl. Phys.*, **99**, 08C909 (2006).

118. Y. K. Su, D. H. Qin, H. L. Zhang, H. Li, and H. L. Li, *Chem. Phys. Lett.*, **388**, 406 (2004).

119. K. R. Van Horn, *Aluminum Vol. III Fabrication and Finishing*, American Society for Metals, Metals Park (1967).

120. A. Mozalev, S. Magaino, and H. Imai, *Electrochim. Acta*, **46**, 2825 (2001).

121. S. Basu, S. Chatterjee, M. Saha, S. Bandyopadhyay, K. K. Mistry, and K. Sengupta, *Sens. Act. B Chem.*, **79**, 182 (2001).

122. S. Lazarouk, S. Katsouba, A. Demianovich, V. Stanovski, S. Voitech, V. Vysotski, and V. Ponomar, *Solid State Electron.*, **44**, 815 (2000).

123. S. Lazarouk, S. Katsouba, A. Leshok, A. Demianovich, V. Stanovski, S. Voitech, V. Vysotski, and V. Ponomar, *Microelectron. Eng.*, **50**, 321 (2000).

124. H. Coufal, L. Dhar, and C. D. Mee, *MRS Bulletin*, **31**, 374 (2006).

125. K. E. Johnson, *J. Appl. Phys.*, **87**, 5365 (2000).

126. H. J. Richter, A. Y. Dobin, R. T. Lynch, D. Weller, R. M. Brockie, O. Heinonen, K. Z. Gao, J. Xue, R. J. M. v. d. Veerdonk, P. Asselin, and M. F. Erden, *Appl. Phys. Lett.*, **88**, 222512 (2006).

127. I. R. McFadyen, E. E. Fullerton, and M. J. Carey, *MRS Bulletin*, **31**, 379 (2006).

128. S. H. Charap, P. L. Lu, and Y. He, *IEEE Trans. Mag.*, **33**, 978 (1997).

129. C. A. Ross, *Annu. Rev. Mater. Res.*, **31**, 203 (2001).

130. D. Weller and A. Moser, *IEEE Trans. Mag.*, **35**, 4423 (1999).

131. H. J. Richter and S. D Harkness IV, *MRS Bulletin*, **31**, 384 (2006).

132. I. Kaitsu, R. Inamura, J. Toda, and T. Morita, *Fujitsu Sci. Tech. J.*, **42**, 122 (2006).

133. R. Wood, *IEEE Trans. Mag.*, **36**, 36 (2000).

134. H. N. Bertram and M. Williams, *IEEE Trans. Mag.*, **36**, 4 (2000).

135. R. H. Victora, *IEEE Trans. Mag.*, **38**, 1886 (2002).

136. S. Khizroev and D. Litvinov, *J. Appl. Phys.*, **95**, 4521 (2004).

137. B. D. Terris and T. Thomson, *J. Phys. D: Appl. Phys.*, **38**, R199 (2005).

138. P. C. Baldwin, *Met. Fin.*, **93**, 84 (1995).

139. F. Mueller, *Plat. Surf. Fin.*, **87**, 54 (2000).

140. N. V. Myung, J. Lim, J. P. Fleurial, M. Yun, W. West, and D. Choi, *Nanotech.*, **15**, 833 (2004).

141. N. V. Myung, D. Y. Park, R. M. Penner, and N. J. Tao, *Electrodeposition of Nanoengineered Materials*, Electrochemical Society, New Jersey (2006).

142. A. T. Voutsas, Y. Hibino, R. Pethe, and E. Demaray, *J. Vac. Sci. Tech. A*, **16**, 2668 (1998).

143. J. Qiu, K. Li, G. Han, Z. Guo, and Y. Wu, *Mat. Res. Soc. Symp. Proc.*, **672**, O8.36.1 (2001).

144. J. A. Thornton, *J. Vac. Sci. Tech. A*, **4**, 3059 (1986).

145. H. Shimizu, E. Suzuki, and Y. Hoshi, *Electrochim. Acta*, **44**, 3933 (1999).

146. S. Takayama, *Mat. Trans.*, **41**, 850 (2000).

147. A. I. Gapin, X. R. Ye, J. F. AuBuchon, L. H. Chen, Y. J. Tang, and S. Jin, *J. Appl. Phys.*, **99**, 08G902 (2006).

148. T. Klemmer, D. Hoydick, H. Okumura, B. Zhang, and W. A. Soffa, *Scripta Mat.*, **33**, 1793 (1995).

149. M. Maret, M. C. Cadeville, R. Poinsot, A. Herr, E. Beaurepaire, and C. Monier, *J. Mag. Mag. Mat.*, **166**, 45 (1997).

150. J. H. Min, B. H. An, J. U. Cho, H. M. Ji, S. J. Noh, Y. K. Kim, H. L. Liu, J. H. Wu, Y. D. Ko, and J. S. Chung, *J. Appl. Phys.*, **101**, 09K513 (2007).

151. G. Pattanaik, J. Weston, and G. Zangari, *J. Appl. Phys.*, **99**, 08E901 (2006).

152. R. H. Victora and X. Shen, *IEEE Trans. Mag.*, **41**, 537 (2005).

153. D. Seuss, T. Schrefl, M. Kirschner, G. Hrkac, F. Dorfbauer, O. Ertl, and J. Fidler, *IEEE Trans. Mag.*, **41**, 3166 (2005).

154. H. Oshima, H. Kikuchi, H. Nakao, T. Kamimura, T. Morikawa, K. Matsumoto, J. Yuan, S. Ishio, K. Nishio, H. Masuda, and K. Itoh, *IEEE Trans. Mag.*, **43**, 2148 (2007).

155. A. I. Gapin, X. R. Ye, L. H. Chen, D. H. Hong, and S. Jin, *IEEE Trans. Mag.*, **43**, 2151 (2007).

156. A. Y. Dobin and H. J. Richter, *Appl. Phys. Lett.*, **89**, 062512-1 (2006).

157. H. J. Richter and A. Y. Dobin, *J. Appl. Phys.*, **99**, 08Q905 (2006).

158. P. N. Loxley and R. L. Stamps, *Phys. Rev. B.*, **73**, 024420-1 (2006).

159. E. Secemski and J. C. Anderson, *J. Phys. D: Appl. Phys.*, **4**, 574 (1970).

160. H. Shima, K. Oikawa, A. Fujita, K. Fukamichi, and K. Ishida, *Appl. Phys. Lett.*, **86**, 112515 (2005).

161. L. J. Heyderman, H. Schift, C. David, B. Ketterer, M. Auf der Maur, and J. Gobrecht, *Microelect. Eng.*, **57**, 375 (2001).

162. S. Y. Chou, P. R. Krauss, W. Zhang, L. Guo, and L. Zhuang, *J. Vac. Sci. Technol. B*, **15**, 2897 (1997).

163. W. Wu, B. Cui, X. Y. Sun, W. Zhang, L. Zhuang, L. Kong, and S. Y. Chou, *J. Vac. Sci. Technol. B*, **16**, 3825 (1998).

164. M. Geissler and Y. Xia, *Adv. Mater.*, **16**, 1249 (2004).

165. W. Wang, X. Liu, X. Wang, Y. Liu, and M. Fan, *Proc. Int. Conf. Solid St. Int. Circ. Tech.*, **5**, 127 (1998).